Quantification of sugar uptake in cells via Raman Spectroscopy

Masterarbeit aus dem Fachbereich der Physikalischen Chemie

von

Simon Martin Wanninger, B.Sc.
geboren am 06.09.1990
in München

Ludwig-Maximilians-Universität
Fakultät für Chemie und Pharmazie
Department Physikalische Chemie, Prof. Don C. Lamb

Quantification of sugar uptake in cells via Raman Spectroscopy

Masterarbeit aus dem Fachbereich der Physikalischen Chemie

von

Simon Martin Wanninger, B.Sc.
geboren am 06.09.1990
in München

Beginn der Masterarbeit: 15.01.2018
Masterarbeit beim Prüfungsausschuss eingereicht am: 16.07.2018

Ludwig-Maximilians-Universität
Fakultät für Chemie und Pharmazie
Department Physikalische Chemie, Prof. Don C. Lamb

Erklärung

Ich versichere, dass ich die vorgelegte Masterarbeit am Department Chemie, Physikalische Chemie der Ludwig-Maximilians-Universität München unter der Anregung und Anleitung von Prof. Don C. Lamb, PhD und Evelyn Ploetz, PhD selbständig durchgeführt habe und keine anderen als die angegebenen Hilfsmittel und Quellen benutzt habe.

München, 15.07.2018

Unterschrift: _____

(Simon Wanninger)

Erstgutachter:	Prof. Don C. Lamb, PhD
Zweitgutachter:	Prof. Dr. Achim Hartschuh

"Innovating means daring to dream, taking the risky route, losing your way without ever giving up and – ultimately – solving a very real problem."

- Pierre-Emmanuel Calmel, Devialet, inventor of ADH® and Heart Bass Implosion HBI®

Abstract

Sugars are an ubiquitous energy source for almost all living organisms. There is a close relationship between the metabolic demand of these sugars and the physiopathological condition of a cell, hence sugar uptake is of high interest in biomedical research. In recent time, different imaging approaches haven been developed to get insight into the biological mechanisms of metabolism, transport and storage of sugars. Advanced fluorescence microscopy is commonly employed to obtain information about protein dynamics and enzyme activities such as membrane transporters at the single-molecule level. Confocal Raman microscopy has proven to be a powerful tool to chemically analyze cells *in vivo* while allowing video-rate imaging in a noninvasive manner. To benefit best from both imaging techniques at the same time, the groundwork for a new imaging technology is laid in this thesis which will combine the advantages of fluorescence and Raman microscopy on a single setup. A dual-color confocal microscope including an additional multiphoton excitation path and a new detection unit was constructed. Characterization of the home-built system was performed via fluorescence correlation spectroscopy and confocal scanning microscopy. To monitor sugar uptake by Raman scattering, a database was acquired containing Raman spectra of solvents, conventional and Raman-labeled sugars This served to develop a software for the quantification of sugars by performing principle component analysis and estimate their detection limit via simulations. Successful culturing of living cells with Raman-labeled sugars and examination via confocal Raman microscopy was achieved.

Acknowledgements

Well, I could probably make this as long as my thesis but time is critical, so here it goes:

First of all, I thank Prof. Don C. Lamb for giving me the opportunity to do my master's thesis in his group. Thank you for always giving feedback when I encountered a problem, for taking me to Heidelberg even though I was not even a master's student yet (quote: "Let's hope it was worth the investment."), for giving me the great honor of researching a new coffee machine for the group and, of course, for making really delicious burgers at the 15th anniversary of FABlab (coming from a vegetarian, this means a lot).

I thank Prof. Hartschuh, not only for agreeing to grade my thesis as a second corrector, but for letting me use his setups for trying to get a sensible Raman spectrum of HeLa cells and for incidentally showing me an interesting experiment involving a single-photon emitter. At this point, I would also like to thank Richard Ciesielski, PhD, for conducting the experiments with me, for putting off with these nasty cells and their annoyingly weak willingness to give off a Raman signal. Also, thank you for the excursion on how to purely theoretically estimate the expected amount of Raman scattered photons and for showing me that interestingly achieved doughnut mode.

I thank you, ~~Prof.~~ Evelyn Ploetz, PhD, for so many things. All this would have never been possible without you taking me in as a student assistant, guiding my efforts and constantly bubbling with new ideas. Thank you for getting me interested in non-linear optics and Raman microscopy, for teaching me how to talk to salesmen (lie...a lot) and for always being available if I had any questions. Thank you for always keeping my motivation up, especially after i got spoiled by the first obtained Raman spectra and for generally reminding me to go home.

I thank Prof. A. Kornath for letting me use his staggeringly bright 1.8 W laser to get these lovely Raman spectra and I thank Florian Zischka for performing the measurements with me, even helping me to keep things organized, and just for the nice company.

I thank Prof. Dr. C. Haisch for letting me use the confocal Raman microscope and David Bauer for conducting the measurements. With these experiments I finally got my real hyper-spectral data cube on which I could test my analysis, which is a large part of my thesis, so thank you for making the time available for me.

I thank Adrian Fuchs, for being the best lab partner I could hope for and all those interesting conversations. Thank you for reassuring me that once a FCS curve is finally obtained, it will stay. Your calm and rational approaches to view the never ending, occurring problems helped me a lot. Also, your dry humor really lightened up my mood.

I thank Waldemar Schrimpf, for teaching me a lot about everything related to microscopy and FCS, especially the technical topics.

I thank Fabian Wehnekamp, for taking me in as a research intern and getting me interested in programming in the first place.

I thank all people in my office for, among other things, being so nice and quiet. Ivo, thank you for showing me how to fix cells, keeping me company on those (loud) weekend sessions and for the recommendation to move to the Biosys office for writing, which was a true life saver. Chen, thank you for supplying me with cells when I needed them and amusing office chair postures. Maria, thank you for always giving me honest input, the occasional chocolate and espresso, and for helping me in the recovery of my injured hand.

I thank Philipp for showing me how to couple laser beams into fibers, how to work zero-mode wave guides and generally for always being helpful and open for discussions. I thank Bettina for cell supply and aspiration of my cells which were rotting in the incubator after I started writing (sorry).

I thank Anders for all the help fixing scanning bugs, for teaching me much about basically everything and for never saying no to a coffee break (just like you, Alex). I thank Kira for proof reading my thesis and together with Anders and Alex always making sure that I had enough to eat. Of course, the same goes for you, Vanessa, but apart from that, I thank you for showing my how to coat slides, use the NanoDrop and for regularly resetting my brain (most likely involuntarily).

I thank Bässem, for showing me how to perfectly recycle individual parts to get a stable linear translation stage and for all the coffee tastings. I thank Frank for supplying me with fluorescent beads, drip extracted coffee and for taking the first step of selling your soul to FABlab. Finally, I would like to thank everyone I forgot.

A special thanks goes to Devialet for delivering me the best sound in the world during my thesis via two phantom speakers, i.e. the combined power of 9000 W resulting in the acoustic pressure of the very much appreciated 216 dB.

Contents

Contents **VI**

1. Introduction **1**

2. Theory **4**

2.1. Fluorescence 4

2.1.1. Overview of Absorption and Emission Processes 4

2.1.2. The Franck-Condon principle and Stokes shift 5

2.1.3. Quantum yield and fluorescence lifetime 7

2.2. Two-Photon Absorption 8

2.3. Raman Spectroscopy 10

2.3.1. Scattering processes 10

2.3.2. Classical description of Raman scattering 12

2.3.3. Experimental dependencies 13

2.4. Confocal Microscopy 15

2.4.1. Resolution 15

2.4.2. Confocal microscope setup 17

2.4.3. Fluorescence Correlation Spectroscopy 18

2.5. Data Analysis 21

2.5.1. Linear Decomposition 21

2.5.2. Principle Component Analysis (PCA) 22

3. Methods **25**

3.1. Description of the home-built setup 25

3.2. Characterization of the home-built microscope setup 29

3.3. Raman Setups 29

3.3.1. Raman spectroscopy in liquid phase 29

3.3.2. Raman spectroscopy in solid phase 31

3.3.3. Confocal Raman imaging of living cells . . . 31
3.4. Data Analysis and Simulation . . . 32
3.4.1. Estimation of the detection limit . . . 33
3.4.2. Live cell data . . . 34
3.5. Cell Culture . . . 35

4. Results and Discussion **37**
4.1. Characterization of the combined one- and two-photon microscope . . . 37
4.1.1. Characterization via FCS . . . 37
4.1.2. Characterization via scanning images . . . 44
4.2. Raman measurements and simulations . . . 49
4.2.1. Raman spectra . . . 49
4.2.2. Estimation of the detection limit . . . 56
4.2.3. Live Cell Measurements . . . 59

5. Conclusion and Outlook **65**

List of Figures **68**

List of Tables **70**

Abbreviations **71**

A. Appendix **79**

1. Introduction

Sugars play a fundamental role in living organisms, as they are the primary source of metabolic energy and carbon skeletons for the biosynthesis of many other cellular compounds. Among all sugars, glucose is obtained in the largest quantity either from the diet or from synthesis in organs such as the liver. All types of sugars are transported inside the organism via the blood stream and must pass the plasma membrane of individual cells before they can be metabolized. Due to its lipid backbone, the cellular membrane is impermeable to sugar molecules which all possess polar and hydrophilic properties. Thus, membrane-associated carrier proteins are required for regulating the influx and efflux of sugars. There are two identified families of transporters distinguished by their main working mechanism, namely SGLT (solute carrier family 5, sodium-glucose symporter) and GLUT (solute carrier family 2, facilitated glucose uniporter). The SGLT proteins actively transport sugars against gradient concentration by exploiting the electrochemical potential generated by the Na^+-K^+ pump which needs energy via ATP hydrolysis.[1,2] The GLUT proteins facilitate the diffusion of sugars by utilizing their naturally occurring concentration gradients at no energy cost.[3–6] Since the GLUT family controls the primary sugar uptake from blood into cells, these transporters are of special interest in the research of cancer, diabetes and the corresponding therapies.[7–16] For example, cancer cells show an increased consumption of glucose which is paralleled by the raised expression level of the GLUT transporter proteins.[17,18] On the other hand, lower expression levels and impaired function of GLUT4 transporters have been linked to diabetes.[14] Various methods have been used to obtain information about the function of sugar transporters and monitor their transport rates. These include probing changes in cell volume induced by sugar, electrophysiology, mass spectrometric analyses and using enzyme-linked markers of the cellular sugar content.[19] One of the most popular techniques is using radioisotopically labeled tracer sugars.[20] However, these approaches usually share common disadvantages such as insufficient characterization of animal transporters, limited temporal and spatial resolution and the demand of large numbers of cells, hence inhibiting the examination of physiologically diverse membrane transporters on a single cell level. Furthermore, the actual functioning of many transporters and their interactions with sugar molecules are still unknown. Studying

sugar-protein interactions, sugar transport and storage in form of glycans by visualization of different sugar moieties remains a major challenge. In recent developments, fluorescent transport activity sensors have been employed to measure the activity of a transporter *in vivo* as a change in fluoresescence intensity.[21–23] Although subcellular resolution can be achieved by these techniques, only the transporters themselves can be examined. Additionally, fluorescent microscopy depends on the expression of fluorescent molecules via external genes, which can directly influence cell physiology and thus may not reflect the natural cellular conditions.[24,25] Due to the large size of fluorophores and intracellular sugar concentrations ranging from µM to mM, sugar uptake is immensely impaired if fluorescent labeling techniques are used. Therefore, a novel imaging technology is needed which is capable of noninvasively probing sugars during transport, metabolism and storage. One of the most promising tools to address these challenges is Raman spectroscopy, which allows the determination of the chemical structure of a cell including proteins, lipids and DNA in a label free manner.[26–30] The main limitation of Raman spectroscopy is the inherently weak signal obtained from spontaneous Raman scattering. Nonetheless, several technological advancements regarding the instrumentation used for detection and especially the development of ultrashort pulse lasers are able to overcome this problem. Modern femtosecond pulsed lasers can be used to generate multiple nonlinear effects such as second-harmonic generation (SHG), multi-photon absorption, coherent anti-stokes Raman scattering (CARS) and stimulated Raman scattering (SRS). In particular, SRS microscopy has emerged as a powerful technique in life and pharmaceutical sciences as well as a diagnostic tool in medicine.[31–37] Still, since the Raman signal of normal sugars is obscured by all other signals of the cell, sugar molecules must be differentiated in some way for adequate identification and quantification. Suitable Raman-labels are nitride, nitrile and alkyne moieties as they are small and exhibit an intense Raman scattering within the Raman-silent region of a cell.[38–40] Using the advantages of both confocal fluorescence microscopy and Raman microscopy in a single setup for elucidating the field of sugar transporters and sugar metabolism is an intriguing idea. It would allow for numerous excitation and detection options, thereby facilitating the imaging and analysis of molecular species over the full concentration range.

In this thesis, the main goal is to lay the groundwork for a multimodal microscope setup which is dedicated for sugar imaging at the single cell level. The designed setup combines single molecule fluorescence based imaging with nonlinear microscopy and will include the implementation of stimulated Raman imaging in the new future. Within the framework of this thesis, a dual-color confocal microscope with extension for multiphoton imaging using a dual-femtosecond pulsed IR laser and a new detection unit has been successfully developed.

Its modular design is open for further modificaitons and facilitates the integration of coherent Raman imaging. To study the cellular sugar uptake by Raman scattering, a database comprised of spontaneous Raman spectra of solvents, conventional and Raman-labeled sugars has been established. With this data at hand, first software for data acquisition and analysis has been developed to quantify the concentration of different sugars. Moreover, based on the experimentally recorded data, simulations have been conducted to estimate the detection limit of a Raman-labeled sugar under various conditions and elicit the feasibility of quantifying sugars in cells. Finally, living cells have been successfully cultured with Raman-labeled sugars and examined using a scanning confocal Raman microscope. Simulations and hyperspectral data obtained from live cell measurements have been analyzed by chemiometric methods, including principle component analysis (PCA) which has been implemented using MATLAB.

2. Theory

In this work, different spectroscopic techniques and imaging modes are employed. The following chapter treats their theoretical background. First, different types of light matter interaction will be discussed, starting from fluorescence, including one- and multiphoton processes, to scattering processes as Raman scattering. The second part deals with imaging, in particular confocal scanning microscopy and chemiometric data analysis which is employed to quantitatively analyze sugar in living cells.

2.1. Fluorescence

2.1.1. Overview of Absorption and Emission Processes

Fluorescence can be described as the spontaneous emission of electromagnetic radiation shortly after the excitation of a fluorescent molecule, often denoted as fluororphore. Figure 2.1 shows a Jablonski diagram, which is commonly used to illustrate different processes of light absorption and emission. If a fluorophore absorbs a photon of a specific wavelength, an orbital electron is excited from its ground state S_0 to a higher quantum state S_1 or S_2. The same energy transition can occur if the energy of two photons match the energy gap between the ground and excited state. In this case, two photons are absorbed simultaneously via an intermediate virtual state. At each quantum state the electron can occupy several vibrational energy levels. At room temperature molecules are electronically in the S_0 state. After absorption of a photon, a common excitation path is the transition from S_0 to a higher vibrational level of S_1. Since a fluorophore undergoes billions of collisions per second with surrounding molecules, it relaxes rapidly to the vibrational ground state of S_1 within picoseconds. In this so called internal conversion, no photons are emitted and the spin state does not change. The radiationless transition from the singlet state S_1 to the triplet state T_1 via spin conversion is known as intersystem crossing, At a duration in the range of 10^{-8} s–10^{-3} s, intersystem crossing is a relatively slow process compared to internal conversion.[41] The relaxation from S_1 to S_0 is termed fluorescence. It is accompanied by an emission of a photon and occurs on a time scale

of nanoseconds. Phosphorescence describes the emission of light by relaxation from T_1 to S_0, which is a forbidden transition and therefore occurs at a low probability. Consequently, the time scale of phosphorescence can be up to a couple of minutes or hours.

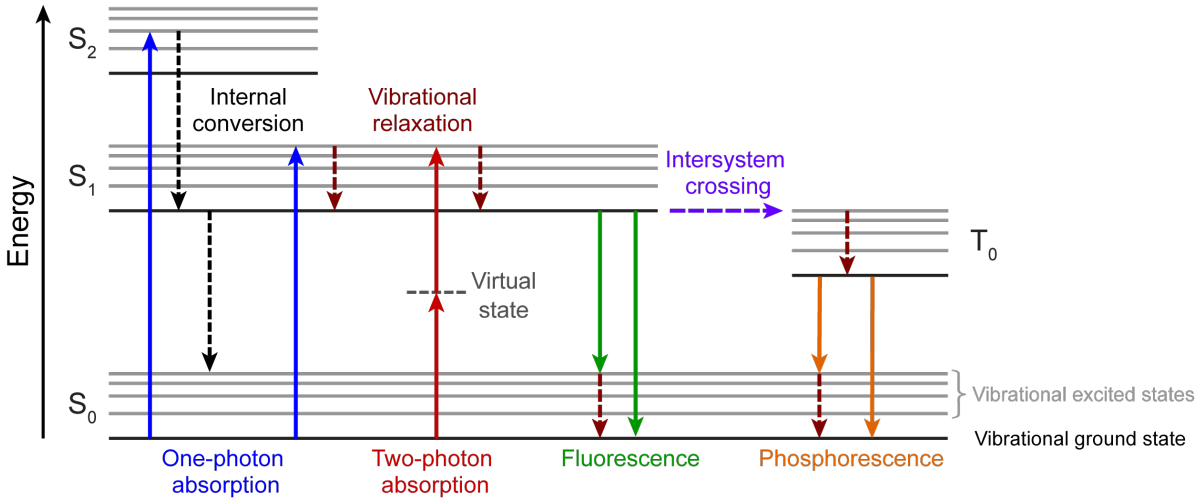

Figure 2.1. | Jablonski diagram: Excitation and relaxation pathways of one-photon (blue) and two-photon absorption (red), vibrational relaxation (dark red), internal conversion (black), fluorescence (green), phosphorescence (orange) and intersystem crossing between the excited singlet and triplet states (purple). Radiationless transitions are represented by dashed lines.

2.1.2. The Franck-Condon principle and Stokes shift

The Franck-Condon principle is a quantum mechanical law, which explains the intensities of vibrational transitions and can also be applied to the absorption and emission of a photon. It states that the probability of a vibrational transition depends on the overlap of the wave functions of the initial and the final energy level after excitation. A core assumption of the Franck-Condon principle is that during an electronic transition, occurring on a timescale of femtoseconds, the relatively slow movement of the nucleus can be neglected, i.e. the wave function does not change. This assumption is known as the Born-Oppenheimer approximation and is mathematically expressed by separating the electronic and vibrational wave functions. The states S_0 and S_1 shown in 2.2a can be described as the product of the vibrational, electronic and spin wave functions:

$$\Psi = \Psi_e \Psi_v \Psi_s \tag{2.1}$$

The probability amplitude P of a transition can be calculated by the scalar product of the initial state $|\Psi\rangle$ and the final state $|\Psi'\rangle$:

$$P = \langle \Psi' | \boldsymbol{\mu} | \Psi \rangle \tag{2.2}$$

where $\boldsymbol{\mu}$ is the molecular dipole operator, given by the sum of the charges and locations of the electrons and nuclei:

$$\boldsymbol{\mu} = \boldsymbol{\mu}_e + \boldsymbol{\mu}_N \tag{2.3}$$

Equation 2.2 can be written as:

$$P = \langle \Psi'_e \Psi'_v \Psi'_s | \boldsymbol{\mu}_e | \Psi_e \Psi_v \Psi_s \rangle + \langle \Psi'_e \Psi'_v \Psi'_s | \boldsymbol{\mu}_N | \Psi_e \Psi_v \Psi_s \rangle \tag{2.4}$$

$$= \underbrace{\langle \Psi'_v | \Psi_v \rangle}_{\substack{\text{vibrational} \\ \text{overlap} \\ \text{integral}}} \cdot \underbrace{\langle \Psi'_e | \boldsymbol{\mu}_e | \Psi_e \rangle}_{\substack{\text{orbital} \\ \text{selection} \\ \text{rule}}} \cdot \underbrace{\langle \Psi'_s | \Psi_s \rangle}_{\substack{\text{spin} \\ \text{selection} \\ \text{rule}}} + \underbrace{\langle \Psi'_e | \Psi_e \rangle}_{0} \cdot \langle \Psi'_v | \boldsymbol{\mu}_N | \Psi_v \rangle \cdot \langle \Psi'_s | \Psi_s \rangle \tag{2.5}$$

Since the two wave functions Ψ_e and Ψ'_e describe two different electronic states, they are orthogonal and the integral $\langle \Psi'_e | \Psi_e \rangle$ is equal to zero. The square of the vibrational overlap integral $\langle \Psi'_v | \Psi_v \rangle$ is proportional to the intensity of a vibrational transition between two different electronic states. The quantities $|\langle \Psi'_v | \Psi_v \rangle|^2$ are called Franck-Condon factors. Figure 2.2a shows the energy diagram of the transitions between $v = 0$ and $v = 2$ which are equally favored. This principle applies to other transitions as well, resulting in an approximate mirror symmetry in the absorption and emission spectra, which is illustrated in 2.2b. In general, sharp peaks are observed for cold and dilute gases whereas solid curves are usually caused by inhomogeneous broadening occurring in liquids and solids.[42] In case of fluorescence, the emission spectrum is independent of the excitation wavelength, which can also be explained by the Franck-Condon principle. Due to the strong overlap of the vibrational wave functions of almost equal energy, the relaxation to the S_1 state occurs on a time scale three orders of magnitude shorter than fluorescence. Hence, emitted photons mainly originate from the lowest excited state regardless of the excitation wavelength. This phenomenon is also referred to as Kasha's rule. Vibrational relaxation causes the emission spectrum of a fluorophore to shift to higher wavelengths and lower energies compared to the absorption spectrum. Additional energy loss is caused by the realignment of the dipole moments of the solvent and the fluorophore occuring after the vibrational relaxation. The total energy difference between the absorption and emission spectra is called Stokes shift and is experimentally observed as a shift between the maxima of absorption and emission spectrum.

Therefore, the Stokes shift also allows to separate excitation and emission in a confocal microscope using dichroic mirrors.

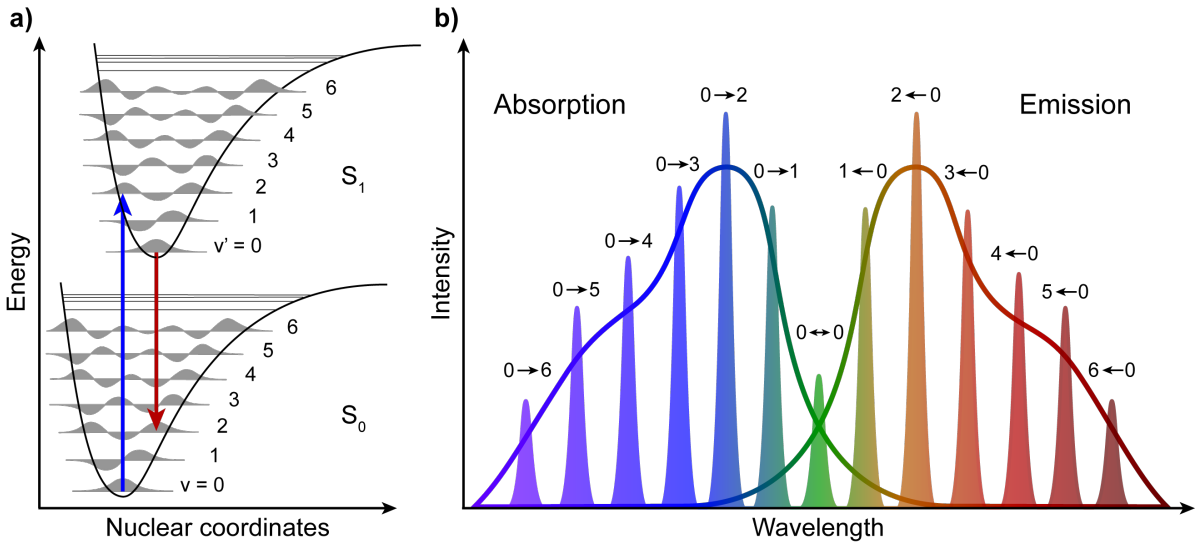

Figure 2.2. | Franck-Condon-Principle: (a) The transitions depicted by arrows are favored due to higher overlap of the vibrational wave functions. (b) Illustration of vibrational transitions in absorption and emission spectra of dilute gases (transparent narrow lines) and liquids (solid lines).[42]

2.1.3. Quantum yield and fluorescence lifetime

The fluorescence quantum yields and fluorescence lifetimes of fluorophores are essential parameters in experiments. The fluorescence quantum yield Q_F can be interpreted as the probability of the relaxation from the S_1 state to the S_0 state via fluorescence and is defined by the ratio of emitted photons to absorbed photons:

$$Q_F = \frac{\Gamma}{\Gamma + k_{nr}} \tag{2.6}$$

where Γ represents the radiative decay rate and k_nr the radiationless decay rate. Q_F can also be an indicator for the brightness of a fluorophore. In experiments, the intensity can be reduced by numerous processes, which are referred to as quenching. These intensity diminishing mechanisms such as collisional quenching, Förster resonance energy transfer (FRET) and complex formation generally depend on the environmental conditions.[43] The time available for the observation of one fluorophore depends on a different property, the fluorescence lifetime.

It is defined as the average time τ a fluorophore stays in the S_1 state, which usually follows an exponential decay:

$$S_1(t) = S_1(0) \bullet e^{-t/\tau} \tag{2.7}$$

where the fluorescence lifetime τ is given by the reciprocal value of the sum of all decay rates depopulating the S_1 state:

$$\tau = \frac{1}{\Gamma + k_{nr}} \tag{2.8}$$

2.2. Two-Photon Absorption

As mentioned in section 2.1.1, two incident photons can be absorbed by a fluorophore simultaneously to excite an electron from the ground state to an excited state. The theory behind this phenomenon was first developed by Göppert-Mayer in 1931.[44] Experimental conformation was achieved in 1961 after the development of pulsed lasers reaching the required local intensity through high spacial and temporal overlap of the incident photons.[45] Two-photon excitation (TPE) has several advantages over one-photon excitation (OPE) such as UV excitation without using a UV source and greater depth penetration for deep tissue imaging. Additionally, the high photon flux required for two-photon absorption exists only in vicinity of the focal region. Hence, optical sectioning is achieved without the use of a pinhole and photo-bleaching is considerably reduced. TPE is a nonlinear optical phenomenon and follows different selection rules compared to one-photon excitation. The probability of a fluorophore absorbing one or multiple photons can be directly related to its electric susceptibility χ, i.e. the degree of polarization induced by the electric field of the laser light. Considering the high intensities obtained from pulsed lasers, χ becomes a function of the electric field $\mathbf{E}$ and the polarization $\mathbf{P}$ can be expressed by a Taylor series expansion of $\chi(\mathbf{E})$:

$$\mathbf{P}(\mathbf{E}) = \epsilon_0 \left(\chi^{(1)}\mathbf{E} + \chi^{(2)}\mathbf{E}^2 + \chi^{(3)}\mathbf{E}^3 + ...\right) \tag{2.9}$$

Here, $\epsilon_0\chi^{(1)}\mathbf{E}$ corresponds to linear polarization, i.e. OPE, and the following susceptibility terms $\chi^{(n)}$ describe the n-th order nonlinearity resulting in $(n+1)$-wave-mixing. In case of TPE, the induced polarization depends on the third order term $\epsilon_0\chi^{(3)}\mathbf{E}^3$. Since two electric field vectors are needed to describe the interaction with a fluorophore, TPE shows a greater dependency on the angle between polarization of the laser beam and the transition dipole moment of the fluorophore leading to a higher degree of photoselection.

In quantum mechanical terms, the transition probability Γ between the initial state $|i\rangle$ and the final state $|f\rangle$ is described by the following equation and shows the quadratic dependency on the incident photon density:

$$\Gamma_{i\to f} \sim \left| \sum_m \frac{\langle f|\,\vec{E}_\gamma \cdot \vec{r}\,|m\rangle\langle m|\,\vec{E}_\gamma \cdot \vec{r}\,|i\rangle}{\epsilon_\gamma - \epsilon_m} \right|^2 \tag{2.10}$$

where the summation is over all intermediate states m, ϵ_m is the energy difference between the state m and the ground state, $\vec{r}$ is the position operator, $\vec{E}_\gamma$ is the electric field vector and ϵ_γ is the corresponding photon energy. Equation 2.10 also shows that the one-photon transition moment $\langle f|\,\vec{E}_\gamma \cdot \vec{r}\,|i\rangle$ requires a change in parity as opposed to the two-photon moment $\langle f|\,\vec{E}_\gamma \cdot \vec{r}\,|m\rangle\langle m|\,\vec{E}_\gamma \cdot \vec{r}\,|i\rangle$ which allows transitions between two states of same parity.[46][47] Due to momentum conservation, the selection rules regarding the angular momentum quantum number l are $\Delta l = \pm 1$ for OPE and $\Delta l = 0, \pm 2$ for TPE. Therefore, the absorption spectra of a fluorophore for TPE can vary significantly from the corresponding OPE absorption spectra. In order to experimentally validate TPE, the relationship between the excitation power and the detected fluorescence signal can be measured. For a continuous wave laser source usually used in one-photon microscopy, the intensity distribution incident on the sample is linearly dependent on the average excitation power. This differs from the intensity distribution in TPE, where the total intensity achieved by a pulsed laser is a periodic function of time and depends on the pulse width as well as the pulse repetition rate. The two-photon excitation probability distribution W_{2p} is given by

$$W_{2p}(t) = \sigma_2 I_0^2(t) \int_V dV S^2(\mathbf{r}) \tag{2.11}$$

where σ_2 is the two-photon absorption cross section, V is the excitation volume, $S(\mathbf{r})$ is the spatial distribution and I_0 is the temporal intensity profile of the laser. Assuming a focal spot of a diffraction-limited objective lens with uniform illumination, the spacial distribution $S(\mathbf{r})$ is described by the corresponding point-spread function:

$$S(\mathbf{r}) = S(v, u) = \left| 2 \int_0^1 J_0(v\rho)\, e^{-\frac{i}{2}u\rho^2} \rho\, d\rho \right|^2 \tag{2.12}$$

Here, J_0 is the zeroth-order Bessel function, v and u are the radial and axial optical coordinates:

$$v = \frac{2\pi r \sin\alpha}{\lambda} \tag{2.13}$$

$$u = \frac{8\pi z \sin^2 \alpha/2}{\lambda} \tag{2.14}$$

Finally, the detected fluorescence signal $F(t)$ depends on the concentration of the fluorophore $C(\mathbf{r}, t)$, the fluorescence quantum efficiency η_2 and the overall collection efficiency of the microscope setup ϕ:

$$F(t) = \frac{1}{2}\eta_2 \phi W_{2p} C(\mathbf{r}, t) \tag{2.15}$$

2.3. Raman Spectroscopy

Light interacts with matter in various ways. The term Raman scattering is associated with the scattering of light by optical phonons in solids or molecular vibrations. Its theory is comprehensively described in literature.[48,49] In the following section, the process of spontaneous Raman scattering are shortly explained in a two-photon picture and its physical background is described dependencies on experimental parameters are derived such as the sample concentration, polarization and intensity of the incident laser light, which are important for this master's thesis.

2.3.1. Scattering processes

When a substance interacts with light, occasionally a small fraction of the light is scattered. Two scenarios can be distinguished. In case no energy is exchanged between the molecule and the electric field during this process, the interaction is termed elastic scattering. The scattered light has the same frequency as the incident one and is called Rayleigh scattering (figure 2.3a). This phenomenon can be viewed as electrons being forced into oscillation by the incident light field, but the "absorbed" energy is "emitted" from a virtual state immediately and radiated again in all directions of space. Spontaneous Raman scattering is an inelastic scattering process of electromagnetic radiation on molecules (figure 2.3b-c). It was first theoretically predicted in 1923[50] and experimentally observed first in 1928 by C.V. Raman.[51] During this process, a portion of energy (equal to a vibration transition within the molecule) is transferred between the incident light field and the molecule. If a portion of energy is retained for excitation of molecular vibrations, the scattered light has lower frequency than the incident light, and is

referred to as Stokes scattering (figure 2.3b). If the molecule is already vibrationally excited, light scattering can also be associated with a release of vibrational energy and an increase in frequency of the scattered light is observed (2.3c). The spectral lines with the frequency reduced by the oscillation frequency (Stokes lines) correspond to the rule of Stokes, those with the higher frequency do not (anti-Stokes lines). For both cases, spontaneous Raman scattering is a linear optical process. Its molecular polarisation **P** depends only linear on the electric field of the incident light. Hence, the detected Raman signal scales linearly with the intensity of the excitation laser. The scattered signal is emitted incoherently in all directions of space. Since one is interested in the oscillation frequencies of the molecules, wavenumbers - shown in a Raman spectrum - are always related to that of the incident excitation light. The difference between the actual wavenumber of the Raman scattered light and that of the excitation light is depicted as Raman shift in cm^{-1}.

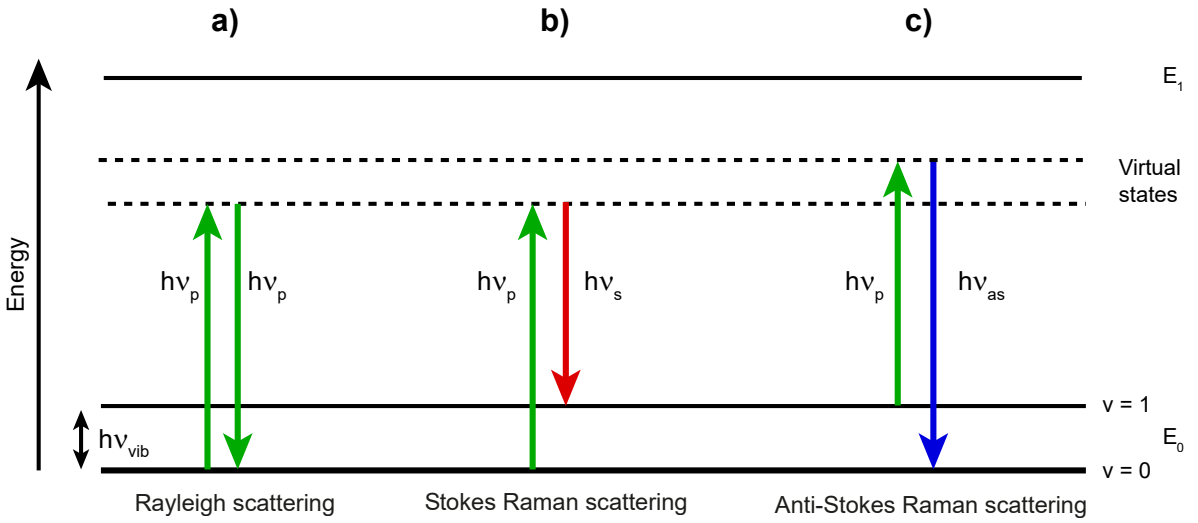

Figure 2.3. | **Scattering processes:** Rayleigh scattering, i.e. elastic scattering, is a passive process. No energy is transferred. b,c) Raman scattering, i.e. inelastic scattering, is an active process. Energy is transferred between molecule and light. Molecular transitions are represented by colored vertical arrows.

2.3.2. Classical description of Raman scattering

The classical theory of the Raman effect is based upon the polarizability of molecules. This parameter reflects how easy the electron cloud of a molecule can be distorted by an electric field. If α is the polarizability and $\mathbf{E}$ is the field strength of an external electric field, the polarization induced dipole moment $\boldsymbol{\mu}$ is described by:

$$\boldsymbol{\mu} = \alpha \mathbf{E} \tag{2.16}$$

Given that $\mathbf{E}$ describes the electric field component of the excitation light with the frequency ν_p and $\mathbf{e}$ the unity vector in direction of the electric field, $\mathbf{E}$ becomes:

$$\mathbf{E} = E_0 \cos\left(2\pi\nu_\mathrm{p} t\right) \cdot \mathbf{e} \tag{2.17}$$

Equation 2.16 can be modified to

$$\boldsymbol{\mu} = \alpha E_0 \cos\left(2\pi\nu_\mathrm{p} t\right) \cdot \mathbf{e} \tag{2.18}$$

The polarizability α is modified by vibration-induced displacements of atoms within the molecule. These can be described via normal coordinates $\mathbf{q}_\mathrm{i}$. For a molecule that vibrates along the normal coordinate $\mathbf{q}$ and unity vector $\mathbf{e}_\mathrm{q}$ with frequency ν, this displacement can be written as:

$$\mathbf{q} = \mathbf{Q} \cos 2\left(\pi\nu t\right) \cdot \mathbf{e}_\mathrm{q} \tag{2.19}$$

Taking the change of molecular shape into account, the polarizability can be approximated within a Taylor approximation along this normal coordinate. It becomes in first approximation:

$$\alpha = \alpha_0 + \frac{\delta\alpha}{\delta q} q + \ldots \tag{2.20}$$

where α_0 denotes the polarizability in the equilibrium state. Going from the microscopic to macroscopic polarization, the macroscopic dipole $\mathbf{P}$, i.e. the polarization of the medium is linked via the polarizability α to the external electric field $\mathbf{E}$:

$$\mathbf{P} = N\boldsymbol{\mu} = N\alpha\mathbf{E} \tag{2.21}$$

with N being the number molecules. The periodic change of the macroscopic polarisation $\mathbf{P}$ along a specific vibration is therefore given as:

$$\mathbf{P} = N \cdot \boldsymbol{\mu} = N \left(\alpha_0 + \frac{\delta\alpha}{\delta q} Q \cos(2\pi\nu t) \right) \cdot E_0 \cos\left(2\pi\nu_\mathrm{p} t\right) \cdot \mathbf{e} \tag{2.22}$$

$$= N \cdot \alpha_0 \cdot E_0 \cos\left(2\pi\nu_\mathrm{p} t\right) + \frac{N}{2} E_0 \frac{\delta\alpha}{\delta q} Q \left[\cos\left(2\pi(\nu_\mathrm{p} - \nu)t\right) + \cos\left(2\pi(\nu_\mathrm{p} + \nu)t\right)\right] \cdot \mathbf{e} \tag{2.23}$$

Due to the oscillating dipole, the polarization $\mathbf{P}$ comprises three superimposed frequencies: ν_p, $\nu_\mathrm{p} - \nu$ and $\nu_\mathrm{p} + \nu$, which are present in the scattered light field. The first term refers to the elastically scattered light, i.e. Rayleigh scattering, the second and third term to inelastic Raman scattering process.

2.3.3. Experimental dependencies

The classical theory correctly predicts the existence of two electric fields that are shifted to lower (Stokes field) and higher (Anti-Stokes field) frequencies with respect to the incident laser frequency. However, it cannot explain the difference in intensity between bands on the Stokes or Anti-Stokes side. This discrepancy can only be explained in the framework of quantum mechanics, which is beyond of this thesis. Shortly, the difference in intensity of both scattering processes is a result a Boltzmann distributed occupancy of vibrational states. As the population of the vibrationally excited state is smaller than within the vibrational ground state, the Stokes scattering exhibits larger signals than Anti-Stokes scattering. Following equation 2.22, it becomes further on obvious that the intensity of Rayleigh scattering scales with the polarizability α_0 while the intensity of Raman scattering scales with $\delta\alpha/\delta q$. The latter has an important consequence, namely, that Raman scattering occurs only if $\delta\alpha/\delta q$ is not equal to 0, i.e. if the polarizability needs to change during the molecular oscillation. In the formulas 2.16-2.22, α is treated as a scalar, i.e. as an isotropic polarizability averaged over all directions. Taking into account that the electric field $\mathbf{E}$ is a vector field, same as the molecular dipole $\boldsymbol{\mu}$, and the polarisation $\mathbf{P}$, the polarizability α is actually a rank two tensor:

$$\alpha = \begin{bmatrix} \alpha_{xx} & \alpha_{xy} & \alpha_{xz} \\ \alpha_{yx} & \alpha_{yy} & \alpha_{yz} \\ \alpha_{zx} & \alpha_{zy} & \alpha_{zz} \end{bmatrix}$$

It depends on the polarization and direction of the electric field of incident light, as well as the orientation of the detection, e.g. the magnitude α_{xy} describes the response of the polarization in x-direction for the electric field applied in y-direction.

The polarizability is anisotropic, so is Raman scattering itself which is irradiated in all directions. For polarized light, the scattered light therefore has two polarization components, i.e. parallel or perpendicular to the incident polarization. If **x** is the direction of incident light, **y** the direction of scattered radiation and **z** the direction of polarization of the incident light, the scattered light will have two orientations of polarization: parallel $I_{\parallel}$ or perpendicular $I_{\perp}$ to the incident polarization (figure 2.4). Thus, the detected signal is strongly dependent on the polarization of the incident laser field, as well as the so-called polarization ratio ρ:

$$\rho = \frac{I_{\parallel}}{I_{\perp}} \tag{2.24}$$

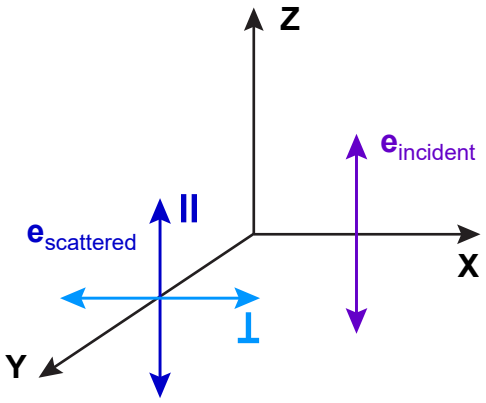

Figure 2.4. | Definition of Raman polarization: Upon the the interaction of a molecule with incident light, the scattered light will have parallel or perpendicular orientations of polarization.

To summarize, the signal strength of detected Raman resonances will strongly depend on the change in polarizability which is dependent on molecular orientation, symmetry of a vibrational mode and the employed laser polarization. Taken the above consideration together, the overall measured Raman intensity can be derived to:[49]

$$I(\nu_p) = Nz\sigma(\nu_p)I_0 \tag{2.25}$$

It depends on the number of molecules per volume N, i.e. the sample concentration c, the sample thickness z, the intensity of the incident laser field I_0 and the Raman cross section σ, which is molecule-specific.

The Raman cross section σ is directly linked to the polarizability α of the molecule via

$$\mathrm{I}(\nu_\mathrm{p}) = \frac{1}{12\pi\epsilon_0 c^3 \cdot \left(2\pi\nu_\mathrm{p}\right)^4 \cdot Q^2 \cdot \left|\frac{\delta\alpha}{\delta q}\right|^2} \cdot \mathrm{I} \tag{2.26}$$

In order to achieve strong signals in spontaneous Raman scattering, the excitation light should have the highest possible frequency. However, it is generally not appropriate to use higher-frequency light than blue light around 488 nm because many substances absorb in the near UV region and a spontaneous Raman spectrum can only be measured if the excitation light is not fully absorbed by the sample. Since many substances absorb in the near UV region, the use of a UV light source would limit its applicability to this substance. For coloured substances, this even applies to visible light. Another important factor, which can be very disturbing in Raman spectroscopy, is the fluorescence emitted by the sample since it can cover the entire range of Raman scattering. For little absorbing samples, fluorescence can be suppressed if the wavelength of the laser light is sufficiently shifted to longer wavelengths. In practice, excitation wavelengths of 532 nm to 1050 nm are employed. The relative intensity ratio of the Rayleigh to Raman scattered light is larger than 10^6. Therefore, Rayleigh scattered light must be highly attenuated before the emitted signal is detected, otherwise the much weaker Raman scattering would be overshadowed by the generated stray light.

2.4. Confocal Microscopy

2.4.1. Resolution

In 1873, Ernst Abbe published his theory on the theoretical resolution limit of a microscope.[52] It states that the lateral limit of microscopic resolution Δx is defined as follows:

$$\Delta x = \frac{\lambda}{2n\sin(\theta)} \tag{2.27}$$

where λ is the wavelength, n is the index of refraction between the lens and the sample, θ is the acceptance angle of the lens and the product $n\sin(\theta)$ represents the numerical aperture (NA), which describes the capability of a lens to focus light. In 1835, George Biddell Airy discovered that light cannot be focused on an infinitely small point due to diffraction and a finite aperture size.[53] Instead, the result will always be a diffraction pattern, which consists of a bright spot (Airy disk) surrounded by a series of concentric rings of decreasing intensity (Airy pattern). Mathematically, the intensities are described by a point spread function (PSF)

and can be calculated by the Kirchhoff's diffraction formula, but are usually approximated by a Gaussian profile. Lord Rayleigh built on Airy's work to further develop Abbe's theory on image generation. He compiled a new criterion for the achievable resolution of a lense based microscope, nowadays termed Rayleigh criterion.[54] It states that two points can be resolved if their first diffraction minima coincide with their maxima. The required distance between the maxima of the two point sources is the resolution limit Δx:

$$\Delta x = \frac{0.61\lambda}{n \sin(\theta)} \tag{2.28}$$

Although the PSF is hourglass-shaped along the optical axis, the equation for the axial resolution limit Δz can be deduced to:

$$\Delta z = \frac{2\lambda n}{(n \sin(\theta))^2} \tag{2.29}$$

Compared to the lateral resolution limit, the axial resolution limit is particularly difficult to achieve in standard wide-field microscopy. Since the whole sample is evenly illuminated and all fluorophores are excited simultaneously, the detected signals include the emitted fluorescence outside of the focal plane. This problem was solved by Marvin Minsky, who filed in the patent for the principle of confocal microscopy in 1957.[55] In confocal microscopy, the unfocused fluorescent light is blocked by a pinhole, which especially increases the axial resolution and the contrast. The term confocal arises from the alignment of the pinhole, which is optically conjugate to the focal plane of the objective lens, i.e. the pinhole and the focal plane are simultaneously in focus. The pinhole diameter is usually expressed in so-called Airy Units (AU). One Airy Unit is defined as the distance between the maximum of the Airy disc and the first minimum of the Airy pattern multiplied by the total magnification of the microscope. The axial resolution for pinhole diameters greater than 1 AU is described by the following equation:

$$\Delta z = \sqrt{\left(\frac{0.88\lambda_0}{n - \sqrt{n^2 - NA^2}}\right)^2 + \left(\frac{\sqrt{2}nPH}{NA}\right)^2} \tag{2.30}$$

where PH is the diameter of the pinhole in micrometers, the first term is called the wave-optical term and the second term is the geometric-optical term.[56] It follows from equation 2.30 that the resolution of the microscope can be enhanced only to some extent by decreasing the pinhole size. For $PH \leq 1$, the geometric-optical term already disappears and for $PH \leq 0.25$ AU, the resolution approaches a finite diffraction-limited value, which is then given by

the following equation:

$$\Delta x = \frac{0.64\lambda_0}{n - \sqrt{n^2 - NA^2}} \tag{2.31}$$

Since pinhole diameters below 1 AU considerably reduce the detection yield and contrast, a compromise between high resolution and detection yield must be made. The optimal pinhole diameter is usually ~ 0.85 AU but can vary depending on the experimental conditions. For wavelengths in the visible range between 488 nm and 640 nm, the theoretical resolution limit in lateral and axial direction hence amounts to approximately 250 nm and 800 nm, respectively.

2.4.2. Confocal microscope setup

As opposed to wide-field microscopy, optical sections are produced by illuminating only a small fraction of the specimen at a time. In combination with the improved axial resolution, this method allows images to be collected noninvasively and therefore renders physical sectioning of the sample unnecessary. A schematic of a simplified confocal setup is shown in figure 2.5. First, the light emitted from a laser (green) is focused onto the first pinhole to form a small point source. After being realigned by a collimator and reflected by a dichroic mirror, the excitation beam is focused onto the sample by the objective lens. The emitted fluorescent light (red) passes through the dichroic mirror and is focused onto to the second pinhole by the tube lens. Instead of the second pinhole, a multimode fiber is commonly used. In this configuration, exclusively fluorescent emission that originates from the confocal volume is collected and subsequently measured by the detector. The high resolution and contrast is accompanied by a reduced signal intensity since only the fluorescence of the confocal volume is detected. Due to the high sensitivity of modern detectors such as photomultiplier tubes (PMT), avalanche photodiodes (APD) or the newly developed hybrid photo detector (HPD) the intensity decrease can be compensated. Since only one point of the specimen is observed at any given instant, several techniques have been developed to obtain a complete image, which are not illustrated in figure 2.5. For a two-dimensional image, the laser beam can be rapidly scanned across the sample in a raster pattern using scanning galvo mirrors or an acousto-optic deflector (AOD). Another method is to move the sample stage using a piezoelectric scanner while the optics remain stationary. The stage scanning technique is especially useful for acquiring 3D images since modern piezo scanners can be moved in all three dimensions with sub-nanometer precision. However, piezo scanning is not suitable for imaging of mobile or dynamic objects objects and hence samples such as living cells must be fixed to the surface.

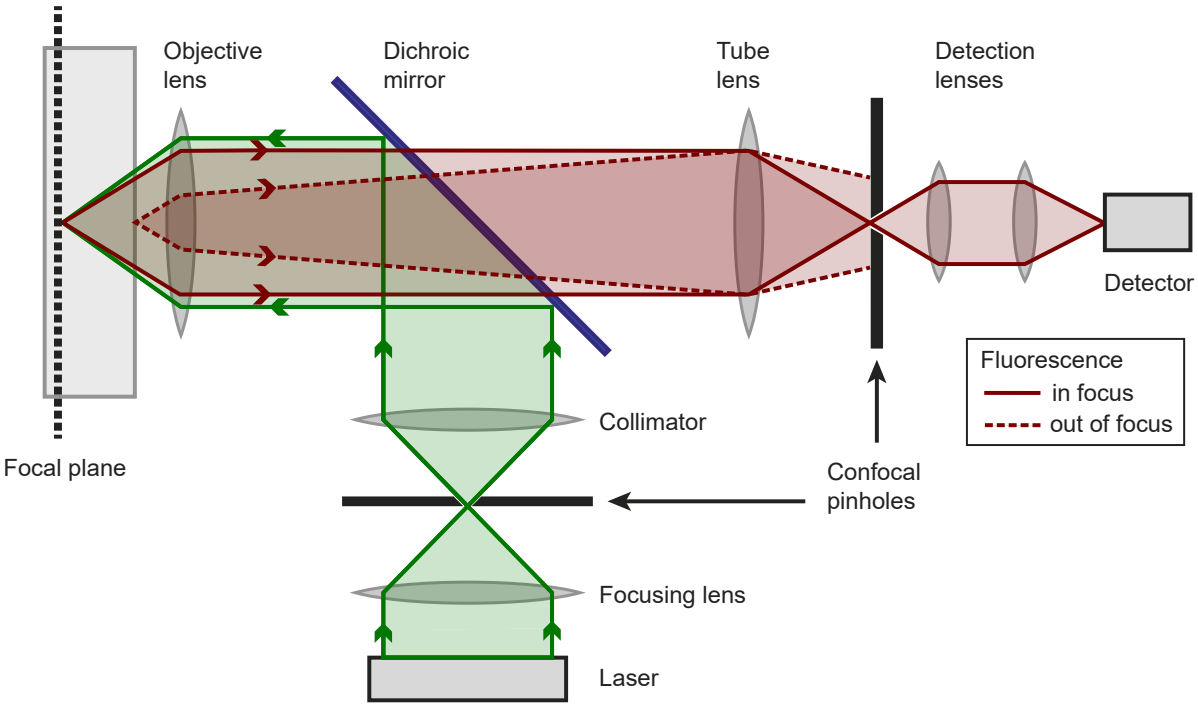

Figure 2.5. | Schematic of a confocal microscope: The excitation beam (green), emitted by a laser, passes the first confocal pinhole and is focused onto the sample. Out of focus fluorescence light (red) is blocked by a pinhole. Only in focus fluorescence light emitted at the focal point is transmitted and detected.

2.4.3. Fluorescence Correlation Spectroscopy

Fluorescence correlation spectroscopy (FCS) is commonly used to determine the concentration, aggregation and diffusion coefficient of fluorescent molecules bound to a system of interest and to examine the molecular interactions between them.[57–59] However, since a defined excitation volume is necessary to calculate these parameters, FCS is a helpful tool to characterize a microscope setup by measuring dyes with known diffusion coefficients. The theory and first experimental realization was developed in the early seventies by measuring the diffusion of ethidium bromide and its binding affinity to DNA.[60–62] Figure 2.6 illustrates the general procedure of FCS. Fluorescent molecules randomly diffuse in and out of the excitation volume which results in intensity fluctuations, i.e. deviations from the mean signal. As long as the fluorescent molecule stays inside the observation volume these fluctuations contain a certain amount of self-similarity which can be measured via the auto-correlation function (ACF). The timescales of the fluctuating signals $F(t)$ are determined by calculating the auto-correlation of the signals as a function of lag time τ.

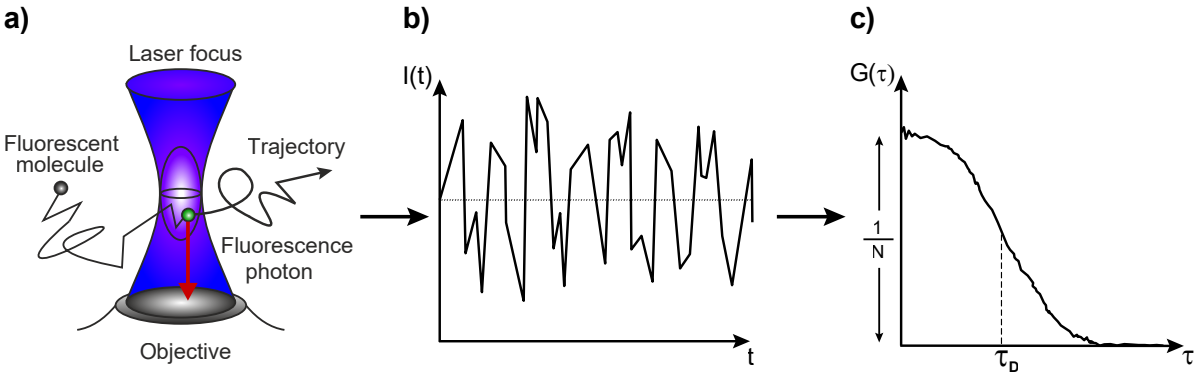

Figure 2.6. | Schematic of the FCS method: a) Fluorescent molecule diffuses through the focal volume. b) The resulting intensity fluctuation is recorded. c) The auto-correlation function is calculated as a function of a time shift τ.

The fluctuations are given by:

$$\Delta F(t) = F(t) - \langle F(t) \rangle \tag{2.32}$$

where $\langle F(t) \rangle$ is the time-averaged fluorescence signal. The ACF of the measured fluctuation, normalized by average intensity squared, is given by:

$$G(\tau) = \frac{\langle \Delta I(t) \cdot \Delta I(t+\tau) \rangle}{\langle I(t) \rangle^2} \tag{2.33}$$

where τ is the lag time, i.e the time difference between two data points. Kinetic properties like the diffusion coefficient can be extracted from the time dependence of the ACF since $G(\tau)$ describes the probability distribution of detecting a photon after a lag time τ. The amplitude of $G(\tau)$ is proportional to the size of the fluctuations and hence it is related to the concentration and brightness of the fluorescent molecule. For short time lags, the intensity fluctuations caused by fluorescent molecules staying inside the focal volume show high self-similarity. The resulting positive correlation value decays with increasing time lag because the fluctuations $\Delta F(t)$ are averaged out. Therefore, the diffusion coefficient and the focal volume determine the time-dependent decay of the correlation function. The concentration can be calculated by

$$\langle N \rangle = \langle C \rangle V_{eff} \tag{2.34}$$

where V_{eff} is the effective observation volume and $\langle N \rangle$ is the average number of fluorescent molecules within the focal spot, which is inversely proportional to the correlation amplitude $G(0)$. This relationship comes from the distribution of molecules being described by a Poisson distribution and hence the variance is proportional to the square root of the mean.

Consequently, ΔC is proportional to $\sqrt{N}$ and the numerator in equation 2.33 contains a factor N while the denominator contains a factor N^2 leading to $G(0) = 1/N$. The effective observation volume V_{eff} depends on the probability of generating fluorescence photons in the vicinity of the focal volume described by a point-spread function $W(\mathbf{r})$ and is usually approximated by a three-dimensional Gaussian function. However, the real excitation volume is larger because it has no clearly defined radius. To account for the uniformity of the fluorescence signal and the effective steepness of the volume boundaries the so-called γ-factor must be considered. It is defined as

$$\gamma = \frac{\int \left(W(\mathbf{r})/W(0)\right)^2 d\mathbf{r}}{\int \left(W(\mathbf{r})/W(0)\right) d\mathbf{r}} \tag{2.35}$$

where $W(\mathbf{r})/W(0)$ is the effective observation volume V_{eff}. In case of one-photon excitation, the ACF for the free diffusion in a three-dimensional Gaussian volume can be expressed as:[63]

$$G(\tau) = \frac{\gamma}{\langle N \rangle} \cdot \left(\frac{1}{1 + 4D\tau/\omega_r^2} \right) \cdot \sqrt{\frac{1}{1 + 4D\tau/\omega_z^2}} \tag{2.36}$$

For two-photon excitation, the ACF can be expressed as:[64]

$$G(\tau) = \frac{\gamma}{\langle N \rangle} \cdot \left(\frac{1}{1 + 8D\tau/\omega_r^2} \right) \cdot \sqrt{\frac{1}{1 + 8D\tau/\omega_z^2}} \tag{2.37}$$

The radii of the Gaussian volume for the lateral and axial dimensions are denoted as ω_r and ω_z, respectively. They are defined as the distance from the center at which the intensity has decayed to $1/e^2$ of the maximum. The relationship between the diffusion coefficient D and the characteristic residence time τ_D (see figure 2.6) is given by:

$$D = \frac{\omega_r^2}{4\tau_D} \tag{2.38}$$

Regarding the performance of fluorescent probes or the quality of a confocal microscope, the molecular brightness η can serve as read-out parameter.. It is defined as the ratio of the average fluorescence count-rate and the average number of fluorophores within the observation volume:

$$\eta = \frac{\langle F(t) \rangle}{\langle N \rangle} \tag{2.39}$$

Observable time scales in FCS range from nano- to milliseconds depending on the experimental condition. The lower time limit is determined by detector deadtime (2 ns–30 ns), detector afterpulsing (100 ns to 5 µs) and the number of detected photons (10 ns–100 ns).

The upper time limit is given by the time a fluorophore diffuses through the excitation volume which can be in range of 10 µs to 1 ms. However, this limit can be extended experimentally either by increasing the observation volumen or by increasing the diffusion time within a viscous environment.

2.5. Data Analysis

2.5.1. Linear Decomposition

Linear decomposition via the least squares method is a comprehensive term in linear algebra which represents the factorization of a matrix into a product of matrices. The main advantage of linear decomposition is its simplicity and high efficiency of solving linear equations. In spectral analysis and many other research fields, linear decomposition is a standard approach for data fitting and various modified approaches exist for handling large data sets, e.g. LU, LDL, Cholesky and QR decomposition.[65–69] A spectrum **B** of a multi-compound sample can be viewed as a set of linear equations in an overdetermined system:

$$\sum_{k=1} x_{i,k} A_{i,k} = B_i \tag{2.40}$$

where $x_{i,k}$ is the contribution of compound k at data point i. This can be rewritten to matrix form:

$$\mathbf{Ax} = \mathbf{B} \tag{2.41}$$

Here, **A** is a column vector of each component. The least squares problem is to find **x** that minimizes $\|\mathbf{Ax} - \mathbf{B}\|^2$. The minimizing vector **x** is called least squares solution of $\mathbf{Ax} = \mathbf{B}$ and can be found by multiplying the equation with the transpose of matrix **A**:

$$\mathbf{A}^{\mathrm{T}}\mathbf{Ax} = \mathbf{A}^{\mathrm{T}}\mathbf{B} \tag{2.42}$$

Solving for **x** yields:

$$\mathbf{x} = \left(\mathbf{A}^{\mathrm{T}}\mathbf{A}\right)^{-1}\mathbf{A}^{\mathrm{T}}\mathbf{B} \tag{2.43}$$

This linear system is called the normal equations.

2.5.2. Principle Component Analysis (PCA)

Principle component analysis (PCA) is a mathematical technique developed in 1901 by Karl Pearson.[70] Today, PCA has a wide range of application in multivariate statistics and any research field which requires the analysis of large data sets.[27,28,71–79] In particular, PCA is used for dimensionality reduction and extraction of the most important, possibly correlated patterns in a multivariate data set by expressing these patterns as a set of a few uncorrelated variables. The newly defined variables are called principal components and are projected onto principal axes describing the direction along which the variation in the data is maximal. Depending on the field of application, various algorithms can be used to transform the data and find the principal axes. The basic and obvious approach is to use the eigenvalue decomposition of the covariance matrix of the data set. However, singular value decomposition (SVD) is often used because it can be directly performed on non-symmetric, non-square matrices. The first step is to mean center a given data matrix $\mathbf{Z}$ of $n \times p$ size, where n is the number of observations and p is the number of spectra. By subtracting the column average from each element, an intercept equal to zero is obtained for the principal component axes:

$$\bar{\mathbf{z}}_p = \frac{1}{n} \sum_{i=1}^{n} \mathbf{z}_{np} \tag{2.44}$$

where $\bar{\mathbf{z}}_p$ denotes the p-th column of the mean centered data matrix $\bar{\mathbf{Z}}$. In addition, the data matrix is normalized to remove the effect of the number of rows on the eigenvalues:

$$\mathbf{X} = \frac{\mathbf{Z}}{\sqrt{n-1}} \tag{2.45}$$

By performing SVD of $\mathbf{X}$, the following decomposition is obtained:

$$\mathbf{X} = \mathbf{U}\Sigma\mathbf{V}^{\mathrm{T}} \tag{2.46}$$

where $\mathbf{U}$ is an orthogonal $n \times n$ matrix containing the left singular vectors, i.e. the eigenvectors of $\mathbf{X}\mathbf{X}^T$, and $\mathbf{V}$ is an orthogonal $p \times p$ matrix containing the right singular vectors, i.e. the eigenvectors of $\mathbf{X}^T\mathbf{X}$.

Σ is a diagonal $n \times p$ matrix of singular values σ_i and has the form

$$\Sigma = \begin{bmatrix} \sigma_1 & & & & & \\ & \sigma_2 & & & 0 & \\ & & \ddots & & & \\ & & & \sigma_i & & \\ & & & & 0 & \\ & 0 & & & & \ddots \\ & & & & & & 0 \end{bmatrix}$$

with $\sigma_1 \geq \sigma_2 \geq \ldots \geq \sigma_i$. The spanned null space depends on the rank r of $\mathbf{X}$ which is equal to the rank of Σ and is defined as the maximum number of linearly independent column or row vectors in the matrix. The singular values σ_i of $\mathbf{X}$ can be calculated by solving:

$$\det(\mathbf{X} - \sigma\mathbf{I}) = 0 \tag{2.47}$$

where $\mathbf{I}$ is the identity matrix. Subsequently, the i-th eigenvector $\mathbf{e}_i$ can be found via:

$$\mathbf{X}\mathbf{e}_i = \sigma_i \mathbf{e}_i \tag{2.48}$$

The close relationship between SVD and the variance of the data set can be established by decomposing the corresponding covariance matrix. Using the definition of the mean centered data $\mathbf{X}$, the $p \times p$ covariance matrix $\mathbf{C}$ can be calculated as:

$$\mathbf{C} = \mathbf{Z}^{\mathrm{T}}\mathbf{Z} = \frac{\mathbf{X}^{\mathrm{T}}\mathbf{X}}{\sqrt{n-1}} \tag{2.49}$$

Since $\mathbf{C}$ is a symmetric square matrix, eigenvalue decomposition can be performed:

$$\mathbf{C} = \mathbf{V}\mathbf{S}\mathbf{V}^{\mathrm{T}} \tag{2.50}$$

where $\mathbf{V}$ is a $p \times p$ matrix of eigenvectors and $\mathbf{S}$ is a $n \times p$ diagonal matrix of eigenvalues λ_i. Combining the SVD of $\mathbf{X}$ (equation 2.46) and the definition of the covariance matrix (equation 2.49) yields:

$$\mathbf{C} = \frac{\mathbf{V}\mathbf{S}\mathbf{U}^{\mathrm{T}}\mathbf{U}\mathbf{S}\mathbf{V}^{\mathrm{T}}}{n-1} = \mathbf{V}\frac{\Sigma^2}{n-1}\mathbf{V}^{\mathrm{T}} \tag{2.51}$$

Hence, the variance of the data set given by the eigenvalues λ_i of the covariance matrix $\mathbf{C}$ can be expressed by the singular values σ_i of the mean centered data $\mathbf{X}$:

$$\lambda_i = \frac{\sigma_i^2}{n-1} \tag{2.52}$$

Furthermore, the direction of maximum variance (principle axes) are described by the right singular vectors $\mathbf{V}$. The original data projected on the principle axes (principle components) are obtained via:

$$\mathbf{XV} = \mathbf{U\Sigma V^T V} = \mathbf{U\Sigma} \tag{2.53}$$

Here, the p-th principle component is the p-th column of $\mathbf{U\Sigma}$. The respective coordinates of the n-th transformed observation in the original data are given by the n-th row of $\mathbf{U\Sigma}$. The original data $\mathbf{Z}$ of the same $n \times p$ size but of lower rank can now be reconstructed by choosing r columns of $\mathbf{U}$, $\mathbf{V}$ and the corresponding $r \times r$ part of $\mathbf{S}$:

$$\mathbf{X}_r = \mathbf{U}_r \mathbf{S}_r \mathbf{V}_r^{\mathrm{T}} \tag{2.54}$$

$$\mathbf{Z}_r = \mathbf{X}_r + \mu \tag{2.55}$$

where μ is the mean value subtracted from each column in the first step of the analysis (equation 2.44). Commonly, the first r eigenvectors are selected which cumulatively explain at least ~ 90% of the total variance in the data set, thus ensuring effective denoising while retaining the most important information. However, the amount of variance accounted for by the first few PCs is lower in Raman imaging due to the larger data sets and the noise, which can increase the intraspectrum variability. Moreover, the chosen rank in approximation can vary depending on the variance of interest explained by the corresponding eigenvector, i.e. principal axes.

3. Methods

In this work, the assembly of a complex setup is presented comprising a fluorescence one- and two-photon microscope with the prospect of performing stimulated Raman spectroscopy in the near future. The main subject of interest is investigating the transport, metabolism and storage of sugars in cells. This chapter describes the various methods which were employed to benchmark the home-built microscope, study different sugars by Raman spectroscopy, performing live cell Raman measurements and analyze the obtained data.

3.1. Description of the home-built setup

The assembled setup is based on a modified Nikon Eclipse TE300 inverted microscope body equipped with an LH-M100CB-1 mercury lamp housing with TE-PS100 power supply, an Hoffman Modulation Contrast G3 Variable Condenser and a 4-way optical path control for a total of three ports. The side port lens of the microscope body was removed to gain more customizable control over the detection path. For coarse sample pos itioning and raster scanning a 3 axis piezo nanopositioner hybrid system (BIO3.200 Piezoconcept) was integrated in the microscope capable of 200 µm scan ranges in all three dimensions. The red and green excitation light is provided by a continuous-wave 633 nm helium-neon laser generating a 500:1 linearly polarized output of 17 mW–25 mW and a continuous-wave 532 nm diode-pumped laser (Cobolt Samba™100 04-01 Series) generating a 100:1 linearly poplarized output of up to 100 mW, respectively. Two photon excitation is accomplished by a prototype fiber coupled laser (FemtoFiber dichro bioMP, Toptica Photonics) providing two separately tunable wavelengths of 780 nm and 1050 nm femtosecond pulses with a 80 MHz repetition rate and an avarage power output of up to 300 mW (780 nm) and 1.5 W (1050 nm). Regarding the one-photon excitation path, the red and green laser are first separately spatially filtered to obtain a gaussian beam profile and expanded to a beam diameter of at least 8 mm to ensure overfilling of the objective back aparture. The green laser is focused by a doublet lens (f = 15 mm, AC064-015-A, Thorlabs) onto a 15 µm pinhole (P15H, Thorlabs) and collimated by an achromatic doublet lens (f = 200 mm AC254-200-A, Thorlabs). The red laser is guided through a telescope

system composed of a focusing doublet lens (f = 15 mm, AC064-015-A), a 20 µm pinhole (P20H, Thorlabs) and a doublet lens (f = 250 mm, AC254-250-A, Thorlabs). Both red and green beam paths are combined by a dual line dichroic mirror (zt532/640rpc, AHF Analysentechnik). Since the radiation coming from the IR laser is highly divergent after the laser output, the 780 nm and 1050 nm excitation are split by a shortpass dichroic mirror (DMSP805, Thorlabs) and guided through two separate telescope systems. After splitting the two wavelengths, both laser beams were broadened and collimated by (f = 100 mm, LA1509-B, Thorlabs) and (f = 150 mm, LA1433-B, Thorlabs) singlet lenses. However, due to the oval shape of the 1050 nm laser beam, a 75 µm pinhole (P100H, Thorlabs) was placed into the focal spot of the focusing lens. Both beam paths were recombined by a shortpass dichroic beamsplitter (HC BS 930 SP, AHF Analysentechnik) and their height above the laser table is adjusted via a periscope, to the height of the one-photon beam path and backport of the microscope body. Finally, the multiphoton infrared and the one-photon beam path were combined by a shortpass dichroic mirror (HC BS 749 SP, AHF Analysentechnik). All laser beams subsequently enter the microscope's back port, are reflected by a polychroic mirror (zt 532/640/NIR rpc, AHF Analysentechnik) and focused into the sample by a 60x 1.20 NA water immersion objective (CFI Plan Apo VC 60XWI). Photons are collected by the same objective, split from the excitation light by the same polychroic mirror and reflected to the side port detection path. First, the signal is filtered by a 750 nm shortpass (FES0750, Thorlabs) and focused onto a 50 µm pinhole (P50H, Thorlabs) by an achromatic doublet lens (f = 250 mm, AC254-250-A-ML, Thorlabs). After being collimated by an achromatic doublet lens (f = 50 mm, AC254-050-A-ML, Thorlabs), photons are split by a shortpass dichroic mirror (BS 647 SP, AHF Analysentechnik) and focused by achromatic doublet lenses (f = 50 mm, AC254-050-A-ML, Thorlabs) onto the detectorchips of the two single photon counting avalanche photodiodes (green channel: COUNT®BLUE , Laser Components; red channel: COUNT®, Laser Components). For one-photon excitation, photons were additionally filtered by emission filters (green channel: HQ580/75, red channel: HQ680/50, AHF Analysentechnik). The APD output is send to two time correlated single photon counting cards (SPC-140 and SPC-150, Becker & Hickl). The synchronization of these TCSPC cards and the lasers is performed by the driver module of the pulsed Toptica laser at the frequency of ~80 MHz. The long focal length of the first signal collecting lens of the detection unit has the advantage of granting enough space for a reflecting mirror in a dual-position slider (ELL6K and ELLA1, Thorlabs) allowing for the implementation of a brightfield imaging path.

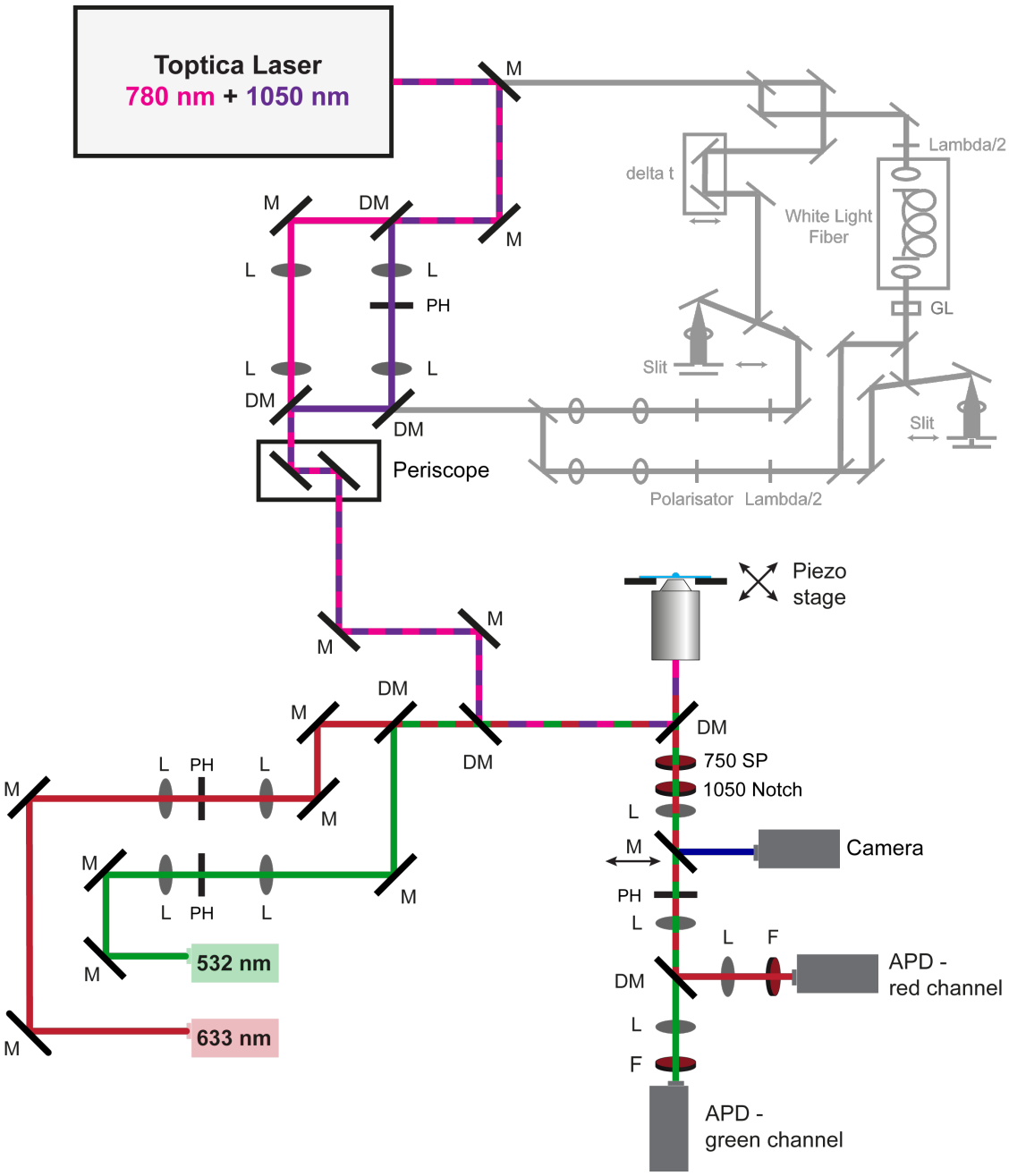

Figure 3.1. | **Microscope setup schematic:** M: mirror, L: lens, PH: pinhole, DM: dichroic/polychroic mirror, F: filter, APD: avalanche photo diode. The Raman section of the setup is gray scaled.

By sliding the reflecting mirror into the detection path, the signal is reflected and focused by an achromatic doublet lens (f = 125 mm, AC254-125-A, Thorlabs) onto an EMCCD camera (DU860D-CS0-BV, Andor), which is operated via Andor Solis software (version 4.19.3, Andor). To provide a broader overview of the sample and select an appropriate imaging region, a CMOS camera (DCC1545M, Thorlabs) was mounted in addition on top of the binocular port (not shown in figure 3.1). Within the one-photon excitation path, broadband dielectric mirrors (BB1-E02, Thorlabs) mounted in kinematic mirror mounts (KM100, Thorlabs) were used. Throughout the two-photon beam path, low group delay dispersion (GDD) mirrors optimized for femtosecond pulses of the corresponding wavelength are used (780 nm: UM10-45A, 1050 nm: UM10-45B, Thorlabs). A schematic illustration of the complete microscope setup is shown in figure 3.1. The currently developed beam path dedicated for coherent Raman imaging is depicted in grey. The complete overview for excitation and detection capabilities of the setup is shown in figure 3.2. Due to a defect beam path of the 1050 nm excitation within the laser, a full demonstration of it capability for dual-color two-photon excitation could not be achieved within the scope of the master thesis.

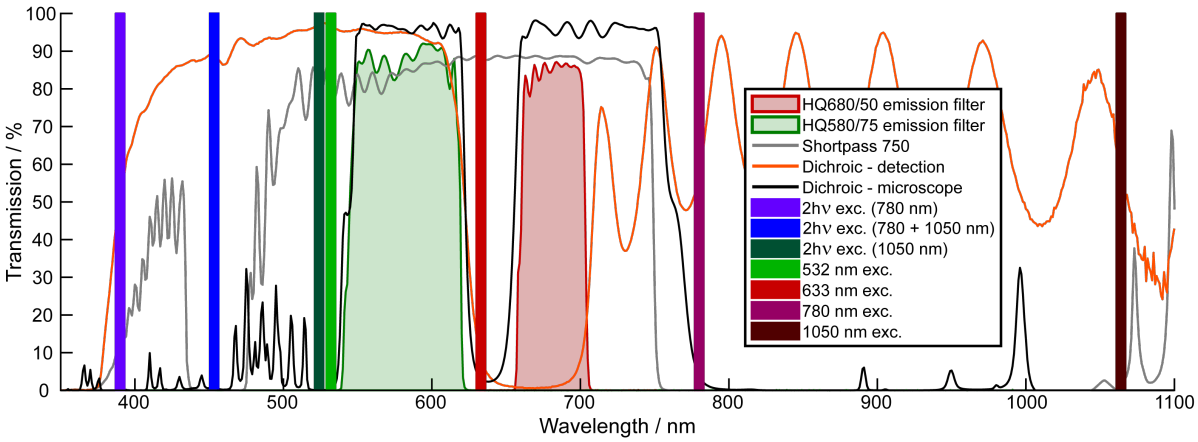

Figure 3.2. | Excitation and detection overview: Laser excitation options are indicated as vertical bars. Filters and dichroic mirrors are represented as colored solid lines. The detection range using the standard filter set used in this thesis is displayed in semi-transparent colors (green, red).

3.2. Characterization of the home-built microscope setup

Confocal volumes of one- and two-photon excitation were determined using fluorescence correlation spectroscopy (FCS). In all measurements, the fluorescence emitted by dyes of known concentrations and diffusion coefficients was detected for 60 s. The recorded FCS values were fitted with the appropriate fit functions with respect to one- and two-photon excitation (see section 2.4.3, equation 2.36 and 2.37), approximating the focal volume as a 3D-Gaussian. According to deviations of the calculated autocorrelation function (ACF), the effects of different excitation powers and the detection pinhole was examined. For the recording of scan images, fluorescence measurements and FCS analysis, the software PAM (pulsed interleaved excitation analysis with MATLAB) was used.[80]

3.3. Raman Setups

Depending on the experimental question, different setups based on spontaneous Raman scattering were used for data acquisition. Raman spectra of solids and substances in solution were measured in collaboration with Florian Zischka (Group of Prof. A. Kornath, LMU) on two different setups. Confocal Raman imaging of live cells was performed in collaboration with David Bauer (Group of Prof. Dr. C. Haisch, TUM München).

3.3.1. Raman spectroscopy in liquid phase

To characterize different solutions and liquids by Raman spectroscopy, a custom build setup was employed. A 532 nm diode pumped, solid state laser (Cobolt Samba™05-01 Series) served as an excitation source. Raman scattered light was detected via a triple Raman spectrometer (T64000, Horiba Scientific) equipped with three gratings in an ultra-high resolution triple additive configuration and capable of a spectral resolution of up to 0.1 cm^{-1}. To record spectra, the laser source was operating at 1.8 W output and focused onto the sample loaded in a NMR tube from two sides by a lens and parabolic optics. The Raman scatttered light was collected in 90° angle and guided into the triple Raman spectrometer. For Raman spectra of sugars, the total integration time was set to 8 min and was recorded from 800 to 4000 cm^{-1} by tuning the detection wavelength from ~532 nm to 675 nm. Raman spectra of solvents were recorded using the same spectral range but a lower integration time of 40 s. A simplified scheme of the setup is shown in figure 3.3.

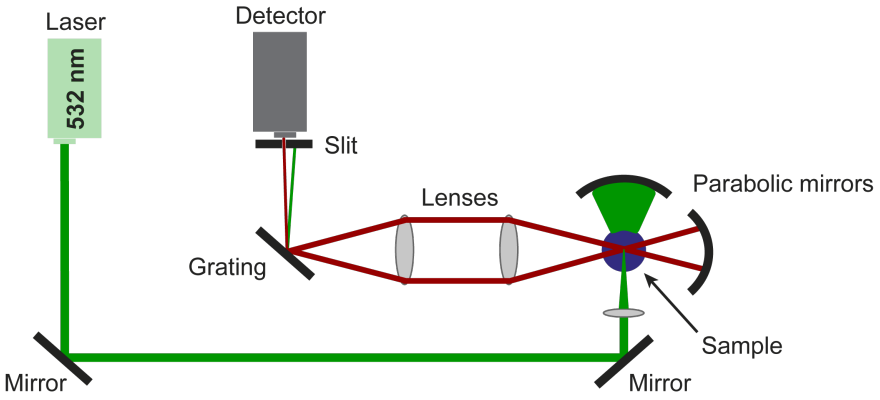

Figure 3.3. | Raman Setup used for liquids: Green excitation light is focused into the sample solution and reflected by a parabolic mirror. Detection is performed in a 90° angle via a triple Raman spectrometer.

The following substaences were characterized by Raman spectroscopy. List of sugars measured at 1 M concentration in water:

- D-Glucose, D-Mannose, D-Galactose
- Methyl β-D-glucopyranoside, Methyl β-D-mannopyranoside, Methyl β-D-glucopyranoside
- N-Acetyl-D-glucosamine (GlcNAc), N-Acetyl-D-mannosamine (ManNAc), N-Acetyl-D-galactosamine (GalNAc)
- 2-Azido-2-deoxy-D-glucose (GlcNAz), deuterated Methyl α-D-glucopyranoside

List of measured pure solvents:

- H_2O (55.5 M), D_2O (55.3 M)
- Ethanol (17.1 M), Ethylengylcol(17.9 M), Chloroform (12.5 M), Toluene (9.4 M)
- Propyn-1-ol (16.9 M), Butyn-1-ol (12.8 M)

Methyl α-D-glucopyranoside was synthesized in collaboration with Adrian Müller-Deku, M.Sc (Group of Thorn-Seshold, PhD) via a Ru/C-catalyzed H–D exchange reaction of methyl α-D-glucoside.[81,82] All other substances were purchased from Sigma Aldrich.

3.3.2. Raman spectroscopy in solid phase

Raman spectra of solids or substances with electronic resonances in the spectral range below 600 nm were acquired using a commercially available Fourier Transform Raman spectrometer (MultiRam, Bruker) equipped with a Nd:YAG-Laser (1064 nm) operating at 1000 mW. The samples were loaded in a NMR tube. The total integration time was set to 10 min for a range of 50 cm^{-1}–3600 cm^{-1} and the spectral resolution of the system amounts to 1 cm^{-1}. Fourier Transform Raman spectrometers do not exhibit dispersive gratings like conventional Raman spectrometers. Instead, a Michelson interferometer is used where the Raman scattered light is split into two beams by a beam splitter.[83] By reflecting one beam off a fixed mirror and the other beam off a movable mirror, different travel lengths and hence time delays are introduced. The temporal coherence of the scattered light can be related to the position of the mirror, thereby transforming the time domain into the frequency domain. The resulting interference patterns are related to the position of the movable mirror and by using a Fourier transform on the interferogram the Raman spectrum is reconstructed and served to measure the following substances:

- D-Glucose, D-Mannose, D-Galactose
- Methyl β-D-glucopyranoside, Methyl β-D-mannopyranoside, Methyl β-D-glucopyranoside
- N-Acetyl-D-glucosamine (GlcNAc), N-Acetyl-D-mannosamine (ManNAc), N-Acetyl-D-galactosamine (GalNAc)
- 2-Azido-2-deoxy-D-glucose (N_3-Glc), deuterated Methyl α-D-glucopyranoside

3.3.3. Confocal Raman imaging of living cells

Confocal Raman imaging was carried out on a commercially available microscope (WITec alpha 300R) using a 633 nm Helium Neon laser (Newport R-14309, 35 mW) as an excitation source and a 63x 1.20 NA water immersion objective (Zeiss W Plan-Apochromat). HeLa cells incubated with normal glucose, N-azidoacetylmannosamine and deuterated Methyl α-D-glucopyranoside were examined. The sample was illuminated from below and stitched widefield images for a broad overview of 4×4 mm were used to obtain a broad overview. Cells were then selected and the scan area was finely adjusted in a rectangle form. For confocal Raman scanning the excitation was realized from above the sample with backwards detection and piezo scanning of the objective. Since a full spectrum for each pixel is measured

a hyperspectral data cube is obtained for every confocal Raman scan. This method is termed hyperspectral imaging and is illustrated in figure 3.4. The excitation power of the red laser (633 nm) was set to 20 mW using an integration time of 0.1 s and a step size of 1 µm for each pixel. For each spectrum an array of 1600 elements (data points) was obtained at a detection region of 643 cm^{-1}–3113 cm^{-1} which corresponds to a spectral resolution of ~1.54 cm^{-1}. The complete dataset was exported as a MATLAB file using the WITec Project FIVE software.

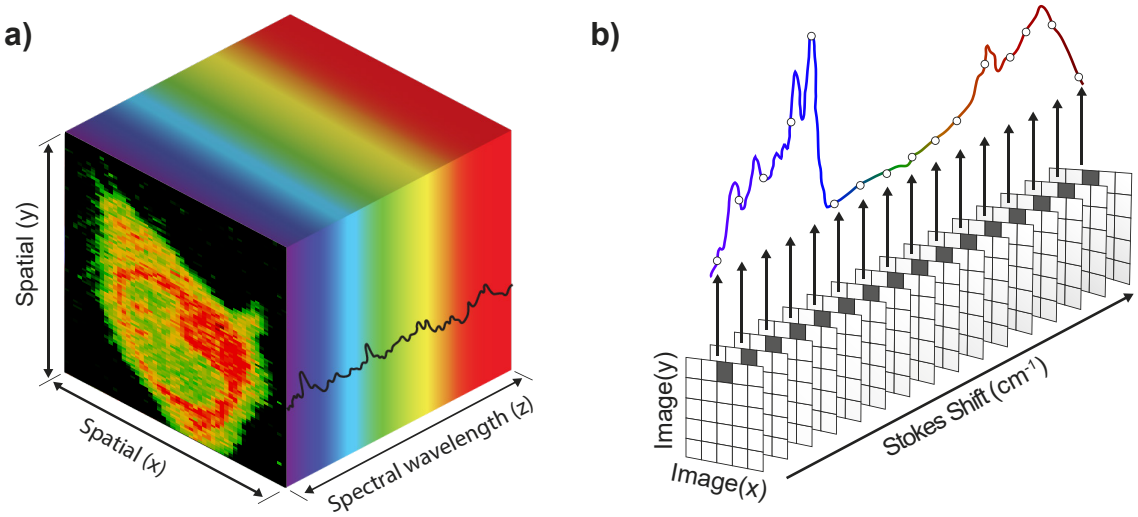

Figure 3.4. | Hyperspectral imaging: a) The hyperspectral image cube is built up during the confocal scan of the sample. b) The hyperspectral data dube is a three-dimensional image comprised of spatial data (x and y coordinates) and spectral data (created by the diffraction grating, which disperses the wavelengths of light). Figure adopted from reference.[84]

3.4. Data Analysis and Simulation

The analysis of hyperspectral Raman datasets as well as the simulation of Raman spectra was executed using the program MATLAB R2017b (MathWorks®). Baseline correction of all Raman spectra was performed via polynomial fitting using the asymmetric truncated quadratic function.[85] The complete source codes developed and used for the simulations and analysis are listed in the appendix.

3.4.1. Estimation of the detection limit

The estimation of the detection limit of a Raman labeled sugar is based on experimental, spontaneous Raman spectra, which were obtained with the Triple Raman spectrometer (see subsection 3.3.1). For the analysis of univariate data, e.g. spectra that differ by a single, clearly separated peak, as well as multivariate and multi-compound spectra, linear decomposition and principle component analysis via singular value decomposition were performed (see section 2.5). Simulated spectra were constructed by linear combination of recorded spontaneous Raman spectra and superimposed Gaussian white noise.[86] Normal linear decomposition and PCA were examined with respect to their accuracy of the reconstruction of a specific broad band substrate spectrum and single peak. For estimating the feasiblity of the project and determining the limits of both analysis methods, the concentration of the substrate and the signal-to-noise ratio (SNR) were considered. The concentration sensitivity was investigated in simulations by scaling the recorded spectrum of the sugar in amplitude in presence of different amounts of experimental noise which was created by adding Gaussian noise to each data point. The substrate of interest was chosen to be the Raman labeled sugar azidoglucose and the azide stretch vibration at ~2120 cm^{-1} was used for single peak spectra. The simulated multi-compound spectrum was composed of nine other recorded substances beside azidoglucose, namely glucose, galactose, mannose, methylglucose, methylgalactose, methylmannose, ethanol and ethylenglycol. All of the predefined noise levels and concentrations of the spectra were combined in nested loop iterations and the accuracy per iteration was determined by the ratio of the calculated concentration and the input concentration. For each combination of noise and concentration the corresponding analysis was performed 40 times to obtain the average accuracy and standard deviation. In each iteration, the SNR was determined by first mean-centering the analyzed spectrum and the corresponding noise. Then, the SNR was calculated via the variance ratio of the data according to:

$$\mathrm{SNR} = \frac{\sigma^2_{\mathrm{spectrum}}}{\sigma^2_{\mathrm{noise}}} \tag{3.1}$$

To solve the linear equations in the linear decomposition analysis, the original real spectra were used. Regarding the PCA technique, the two most important parameters influencing the quality of the analysis are the total number of spectra in the data set and the rank approximation used for the recreation of each spectrum. The calculation time of PCA increases for larger data sets and had to be perfomed several thousand times. Hence the total amount of spectra had to be limited to 2000, which is large enough for effective denoising of the data and still well below the typical size of data sets obtained by confocal raman scans.

The rank selected for the recreation usually depends on the variance one is interested in. For example, a rank 1 approximation can fairly accurately describe the variance in the data but the desired information may be in component 2 or 3 and would get lost. In case of quantifying one substance in a constant background signal, the variance of interest is mainly described by one component which can differ depending on the background signal and measurement noise.

3.4.2. Live cell data

Depending on the size of the scanned area and stepsize, hyperspectral data cubes obtained from live cell raman scans consisted of up to 12000 spectra. The MATLAB script used for the analysis of these datasets can be found in the appendix. PCA was directly performed on the raw data to determine and correct for outliers, e.g. spectra containing large spikes caused by cosmic rays. The hyperspectral data cube was first reshaped into a 2D matrix $\mathbf{Z}$ of $n \times p$ size and mean centered according to the equations described in section 2.5.2:
Mean centering:

$$\mathbf{x}_j = \frac{1}{n} \sum_{i=1}^{n} \mathbf{z}_{ij} \tag{3.2}$$

Standardization by rows:

$$\mathbf{X} = \frac{\mathbf{Z}}{\sqrt{n-1}} \tag{3.3}$$

Singular value decomposition was then performed via:

$$\mathbf{X} = \mathbf{U}\Sigma\mathbf{V}^{\mathrm{T}} \tag{3.4}$$

To determine and correct for outlier spectra, PCA biplots of the decomposed matrices were created. A biplot not only contains the common scatter plot of the principle components but also the corresponding loadings which can be achieved by standardization. Standardized loadings are given by columns of $\mathbf{VS}/\sqrt{p-1}$ and standardized principle components are given by columns of $\sqrt{n-1}\mathbf{U}$. Loadings are useful for the visualization of the analyzed data set and contain valuable information as they are the weights by which each standardized original variable should be multiplied to get the component score. Therefore, loadings also represent the eigenvectors scaled by the covariances observed between the spectra. Outliers can be easily identified since not only the direction but also the magnitude of the eigenvectors can differ significantly from the main cluster of spectra. Furthermore, the vertical sums of squares of the loading matrix are the eigenvalues, i.e. the components' variances. The horizontal

sums of squares are the fraction of variance in the data set being explained by the components which can be used for an appropriate reconstruction of the data. After baseline correction using the asymmetric truncated quadratic function, Raman maps were created via univariate data analysis. Mean spectra were obtained by first choosing a standard deviation threshold for the integrated intensity of a specified spectral region. To adjust this threshold, individual pixels fulfilling the criterion were immediately compared to the Raman intensity map of the cell. The standard deviation threshold was determined iteratively until the selected pixels coincided with the Raman map. The two clusters of spectra were averaged separately in order to get a mean cell spectrum, a residual spectrum of the medium and the difference spectrum.

3.5. Cell Culture

Sugar uptake in living cells was studied for HeLa cells (epitheloid cervix carcinoma). These were grown in F75 flasks (surface area: 25 cm^2, working volume: 5 mL). The complete growth medium consisted of Dulbecco's Modified Eagle's Medium (DMEM) containing 4.5 mg/L glucose, non-essential amino acids (NEAA), 10% fetal bovine serum (FBS), 2 mM L-glutamine, 1 mM sodium pyruvate and Penicillin-Streptomycin (1/100). All supplements for the treatment of HeLa cells were purchased from Thermo Fisher Scientific.

Resuscitation of frozen cells

Frozen cells were thawed in a 37 °C bath, transferred to a F75 flask already containing 4 mL of the complete growth medium. For growth and maintenance, the cells were placed in an incubator at 37 °C with a 5% carbon dioxide content of the atmosphere to realize slightly acidic conditions. The day after thawing, most of the cells stuck to the surface of the flask and the growth medium was aspirated. To remove any dead cells and residues of the freezing medium, the flask was washed using 5 mL Phosphate-buffered saline (PBS, pH 7.4, without Calcium, Magnesium and Phenol Red) and the remaining living cells were provided with new growth medium. At ~ 80% confluency, passaging was conducted by first washing with 5 mL PBS, adding 1 mL Gibco®Trypsin-EDTA and incubating for 2 min. Trypsin was deactivated by adding 4 mL cell media while carefully pipetting the whole solution to avoid cell agglomeration. Afterwards, the cells were split at a 1/5 ratio by transferring 1 mL of the homogeneous cell solution to a new F75 flask. The passaging procedure was repeated twice a week.

Storage of cells

For storage, the residual cell solution was pipetted into a falcon tube and centrifuged at 1200 rpm for 4 min at room temperature. After aspiration of the supernatant, the freezing medium was added to the isolated cell pellet. The freezing medium consisted of the regular complete growth medium and 5% dimethyl sulfoxide (DMSO) used as a cryoprotectant. The cell solution was made homogeneous by pipetting and was stored at −80 °C in 1 mL Eppendorf Tubes®.

Confocal Raman imaging of living cells

For monitoring sugar uptake in living cells by Raman scattering, HeLa cells were grown and seeded over night in media containing different types of sugars. For first proof-of-concept experiments, cells were either provided with usual, high glucose DMEM (25 mM) or low glucose DMEM (5 mM) with additional Raman-tagged sugar (20 mM, N-azidoacetylmannosamine and deuterated Methyl α-D-glucopyranoside) in a ratio of 1:4. Cells were seeded on poly-lysine coated 35 mm wide glass bottom dishes (MatTek Corp. Ashland, USA, P35GC-0-14-C) and characterized by an inverted Raman scanning microscope (WITec GmbH, see subsection 3.3.3). The dishes were washed trice with PBS and the buffer was replaced against PBS directly before Raman imaging. For confocal scan imaging performed on the home-built setup, cells were fixed on Lab-Tek®2 chamber slides. The first step in the fixing procedure was aspiration of the cell medium and washing with 0.5 mL PBS. Then, 0.5 mL of a freshly prepared 4% paraformaldehyde (PFA) solution was added to each chamber. Since PFA is highly photounstable, the chambers were covered with aluminium foil.

After 15 min incubation time, PFA was removed and the fixed cells were washed twice with 0.5 mL PBS. Depending on the experiment, WGA488 stain was added For live cell imaging, HeLa cells were provided over night with either usual high glucose DMEM or modified DMEM containing low glucose DMEM and the raman labeled sugar (N-azidoacetylmannosamine and deuterated Methyl α-D-glucopyranoside) in a ratio of 1:4.

Since the excitation and detection of the confocal Raman setup used for live cell imaging was realized from above the sample, Lab-Tek®2 chamber slides were inadequate and HeLa cells had to be incubated on cover slides.

4. Results and Discussion

This chapter is partitioned into two main sections. In the first section, the home-built multimodal confocal microscope capable of simultaneous one- and two-photon excitation is characterized via fluorescence correlation spectroscopy (FCS) and imaging of fixed cells. Results with respect to Raman spectroscopy on sugars, simulations and Confocal Raman imaging for monitoring sugar uptake in live cells are discussed in the second section.

4.1. Characterization of the combined one- and two-photon microscope

4.1.1. Characterization via FCS

One-photon excitation

As described in section 3.2, FCS is a useful tool to determine the focal volume and examine the influence of various optical elements. After completion of the setup and the first successful FCS fit curves, the optimal position of the detection pinhole was determined. Due to chromatic aberrations, the refractive index of a lens depends on the wavelength of the emitted fluorescence. Hence, the detection pinhole can not be optimally placed in the focal point of the first focusing lens for all wavelengths and a compromise must be made. The long focal length of the first detection lens ($f = 250\,\text{mm}$) has the advantage of minimizing chromatic aberrations but the disadvantage of being more sensitive to the alignment. First, the optimal pinhole position for each channel was determined separately by estimating the maximum molecular brightness while moving the pinhole, mounted on a translation stage, along the optical axis. Since these positions represented the minimum and maximum chromatic shift between green and red fluorescence, the mean value was defined to be the the ideal pinhole position and a lookup table for two color measurements. A FCS measurement with 60 s runtime and excitation powers of 2 µW (532 nm) and 9 µW (633 nm) was performed on both channels for every pinhole position. Higher excitation powers would result in a

higher signal-to-noise ratio but would also significantly increase the triplet state population of the excited fluorophores which complicates the subsequent data fitting. For both channels a solution of 10 nM Atto532 (green emission, D = 373 µm^2 s^{-1}, Atto-tec Germany) and 10 nM Atto655 (red emission, D = 393 µm^2 s^{-1}, Atto-tec Germany) was used. The FCS data was fitted using a fixed diffusion coefficient of the respective dye. As expected, the FCS fit curves (figure 4.1) and the corresponding values (table 4.1) show a less defined focal volume if the pinhole position is optimized for the opposite channel, especially in z-direction. The trade-off position for multicolor measurements causes a small and tolerable deviation from the optimum for both channels.

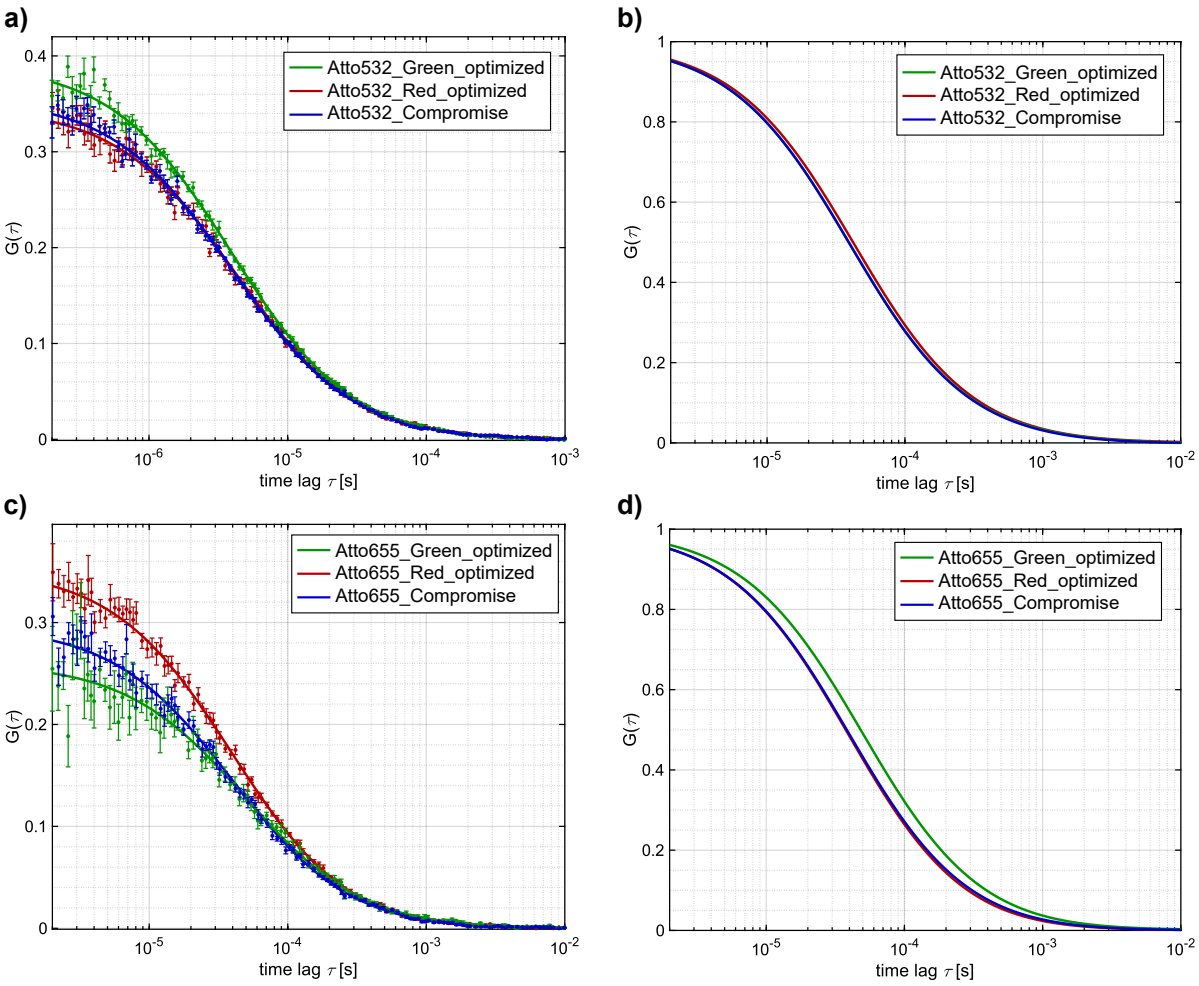

Figure 4.1. | Influence of pinhole position on FCS curves: (a),(b) Unnormalized and normalized FCS curves recorded for the green channel. (c),(d) Unnormalized and normalized FCS curves recorded for the red channel. Alignment of the pinhole was optimized for the green channel (green), the red channel (red) and both channels (blue).

Table 4.1. | FCS fit values for different pinhole positions.

FCS curve	Counts [kHZ]	η [kHz]	N	w_r [µm]	w_z [µm]	χ^2
Atto532_Green_opt.	28.6852	32.8352	0.901	0.2503	1.4933	1.05
Atto532_Red_opt.	24.2575	23.8053	1.019	0.2614	1.6910	1.04
Atto532_compromise	30.8068	31.1039	0.990	0.2533	1.6163	1.41
Atto655_Green_opt.	11.4023	8.3901	1.359	0.2801	1.4127	0.82
Atto655_Red_opt.	22.2005	22.1685	1.001	0.2509	0.9477	0.90
Atto655_compromise	21.1534	17.7630	1.191	0.2499	1.2619	1.11

To further confirm the function of the complete system fluorescent molecules in 10 nM Atto532 and 10 nM Atto655 solutions were slowed down by preparing samples containing different amounts of highly viscous glycerol. In the fitting procedure the focal volume determined by the first measurement without glycerol was fixed (532 nm excitation: w_r = 0.2501 µm, w_z = 1.5131 µm, 633 nm excitation: w_r = 0.2492 µm, w_z = 1.3063 µm). The recorded FCS data and normalized fit curves (figure 4.2) show the increasing time lag with increasing concentration of glycerol. An overview of the determined diffusion coefficients for both dyes can be found in table 4.2. It must be noted that glycerol can cause quenching and higher triplet state populations of the fluorescent molecules. The effects are more apparent for Atto655, resulting in larger error bars at short time scales. Additionally, glycerol alters the focal volume due to its high refractive index of n = 1.4746.

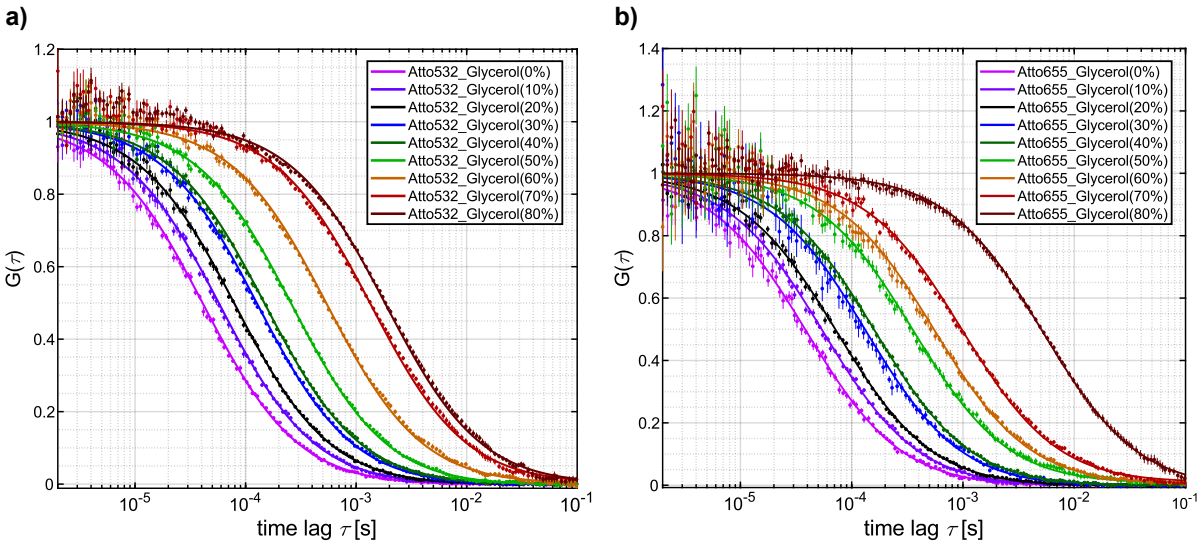

Figure 4.2. | **FCS curves investigating the Influence of the viscosity by the medium:** FCS data and fit curves of (a) 10 nM Atto532 and (b) 10 nM Atto655 in PBS and increasing amount of glycerol.

Table 4.2. | Diffusion coefficients D in dependence of glycerol content determined by FCS.

Glycerol content	0 %	10 %	20 %	30 %	40 %	50 %	60 %	70 %	80 %
D [$\mu m^2\ s^{-1}$] (Atto532)	373	266	193	120	103	59	28	11	8
D [$\mu m^2\ s^{-1}$] (Atto655)	393	279	210	113	94	43	27	14	7

Two-photon excitation

The characterization of two-photon excitation (TPE) employing the 780 nm pulsed femtosecond laser was conducted using similar parameters as for one-photon measurements. FCS curves were recorded with 60 s runtime and Atto532 proved to be a suitable dye for two-photon absorption. Two-photon microscopes usually do contain a detection pinhole since optical sectioning is already achieved by the inherently low axial spread of the two-photon point spread function. However, the same detection path is used for one- and two-photon absorption at 780 nm excitation. To characterize the influence of the detection pinhole, FCS spectroscopy on ~70 nM Atto532 at the same excitation power of 4.7 mW were recorded with and without detection pinhole (figure 4.3) . In case of a detection pinhole in place, the FCS fit curve shows an increase in signal-to-noise ratio and a shift to lower time scales. The corresponding fit values (table 4.3) confirm a significantly smaller observation volume, particularly in z-direction by ~63 %.

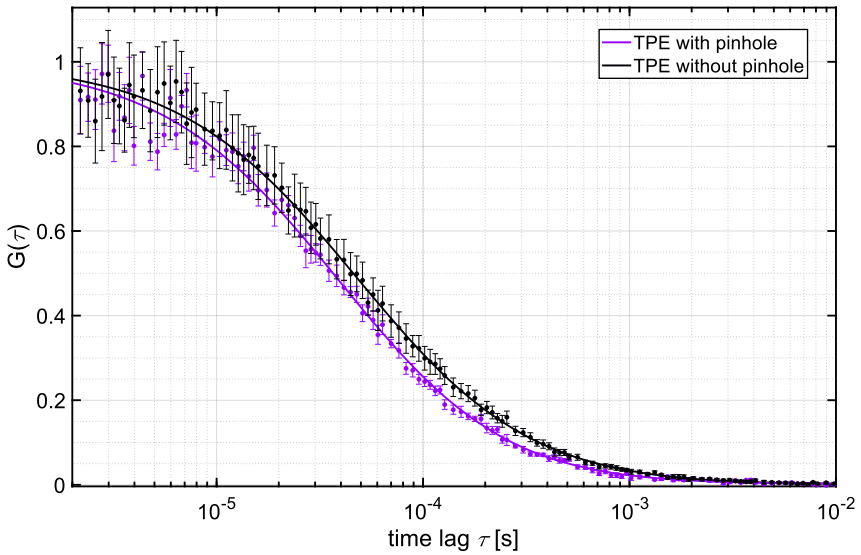

Figure 4.3. | **Confocal pinhole effect on two-photon FCS:** The FCS curve recorded with detection pinhole (purple) shows an improvement of the axial resolution due to the shift to lower time scales compared to the FCS curve without detection pinhole (black). Error bars are indicated as vertical lines have lower values for the measurement with detection pinhole.

Table 4.3. | FCS fit values of detection pinhole effect on TPE.

FCS curve	Counts [kHZ]	η [kHz]	N	w_r [µm]	w_z [µm]	χ^2
TPE no pinhole	92.0602	18.9657	4.854	0.379	1.623	0.21
TPE with pinhole	41.9187	13.4203	3.123	0.347	1.020	1.17

This can be explained by the pinhole acting as an additional filter for scattered light. Hence, the resolution can also be improved for TPE by using a detection pinhole which comes at the cost of a decreased count rate and brightness.

In order to actually confirm TPE, the intensity of a solution of 50 nM Atto532 was recorded with increasing power of the 780 nm laser in a range of 2 mW–100 mW. The average intensity of each measurement and the excitation power was plotted in a double logarithmic plot (figure 4.4). According to the square power law of TPE a linear fit should therefore have a slope of 2 which is the case for excitation powers in the range of 3 mW–7 mW. Starting at 8 mW, several effects cause a deviation from the square power dependence, most importantly the saturation effects.[87] First, a 50 nM Atto532 solution provides only a limited amount of molecules in the focal volume to be excited by the laser. Secondly, large excitation powers lead to a higher probability of two-photon absorption in the outer region of the PSF. This results in a considerable increase of the excitation volume which should slightly compensate for the low concentration of fluorescent molecules. However, the measurement values start to diverge from the square power law before the true intensity saturation is reached at ~1.7×10^5 counts. The explanation can be derived from the corresponding FCS curves shown in figure 4.5. In the range of 3 mW–7 mW (figure 4.5a, the 2 mW measurement is omitted for clarity), an increase of the signal-to-noise ratio can be observed with increasing excitation power and the FCS curves have the same reproducible shape. The fit values (table 4.4) show a stable focal volume 3 mW–6 mW which is independent of the excitation power. In particular, the unaffected axial width is in contrast to one-photon excitation measurements. The fit values of the 7 mW measurement begin to suggest a smaller axial width of the focal volume which is a continuous trend for the following 8 mW–18 mW range. Due to reasons described in the following, the calculated focal volumes as well as the diffusion coefficient are not reliable above laser powers of 6 mW. Beginning at 8 mW the correlation amplitude is steadily increasing until 18 mW excitation power is reached (figure 4.5b). The overall fluorescence intensity maximum is obtained at ~14 mW excitation power. This can be explained by photobleaching which lowers the effective concentration of fluorescent molecules in the observation volume. At ~20 mW the correlation amplitude begins to decrease and flattens at 100 mW excitation power (figure 4.5c). Two factors are the most likely cause for this phenomenon. While the fluorescent

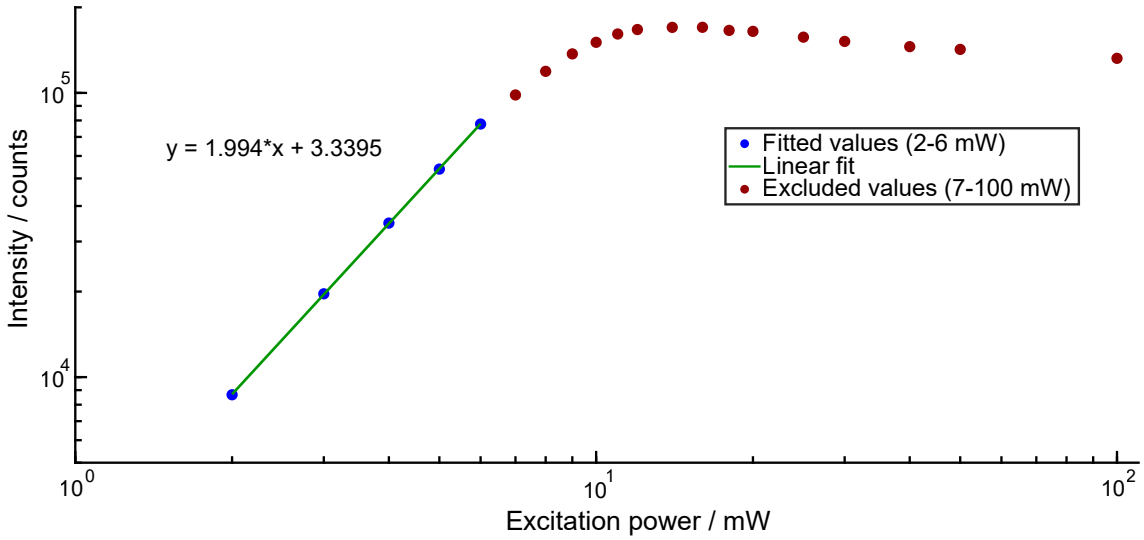

Figure 4.4. | TPE laser power dependence: Double logarithmic plot of detected intensity and average excitation power. Fitted measurement values are represented by blue dots and confirm the square power law. The values influenced by saturation and bleaching effects are excluded from the fit (red dots).

molecules are still being photobleached, the high photon flux achieved at these laser powers lead to a significant enlargement of the PSF. Thus, the effective concentration with respect to the excitation volume increases at a greater rate than the concentration decrease caused by photobleaching. Regarding the correlation amplitude, the value at which the two effects would compensate each other is ~0.15 using an average laser power of ~47 mW. The other factor to be considered is the larger contribution from uncorrelated background at high laser powers. Figure 4.5d displays the normalized FCS curves of the 7 mW–50 mW range where photobleaching and saturation effects become apparent. The 100 mW measurement is omitted for clarity since its FCS curve coincides with the the FCS curve of the 50 mW measurement. Here, it can be seen that photobleaching plays a role throughout the power range and consistently increases with the excitation power. Photobleaching causes the FCS curves to shift to lower relaxation time scales since the fluorescent molecules are destroyed before they are able to diffuse out of the focal volume. The saturation effects can be influenced by a number of parameters. Provided a stable alignment and that the used optical elements do not change, the shape of the PSF solely depends on the laser intensity and could therefore be calibrated. However, the photobleaching effects additionally depend on the properties of the observed fluorescent species, e.g. the stability and absorption cross section. With respect to Atto532, it can therefore be concluded that laser powers exceeding 7 mW should be avoided in order not to bias results on unknown samples.

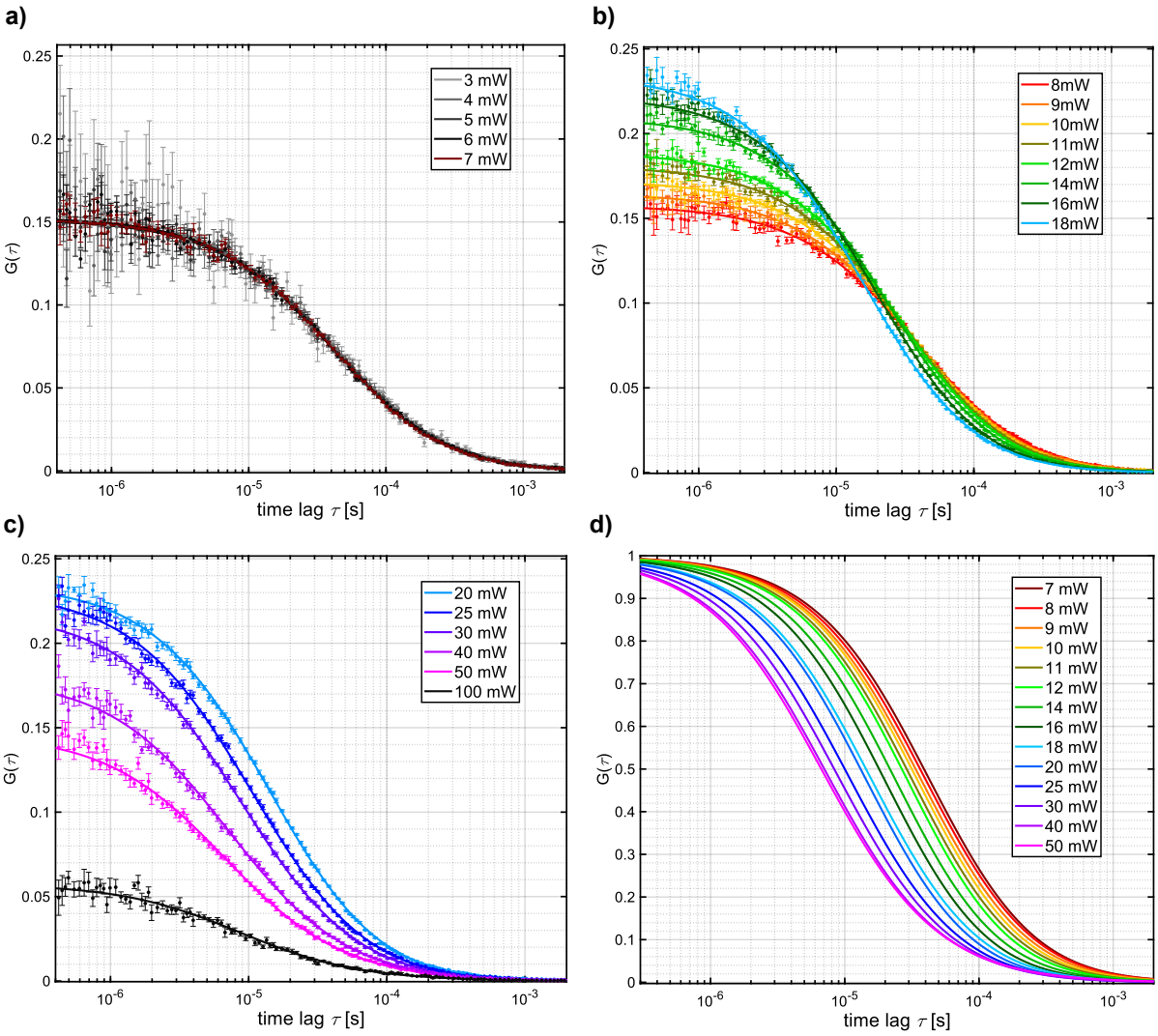

Figure 4.5. | Two-photon FCS laser power dependence: (a) 3 mW–7 mW: Reproducable shape and smaller errors at higher laser power. (b) 8 mW–18 mW: Increasing correlation amplitude with higher laser power caused by photobleaching. (c) 20 mW–100 mW: Decreasing correlation amplitude with higher laser power caused by the increasing excitation volume and background contribution (d) 3 mW–50 mW: Normalized FCS curves showing the decreasing relaxation time scale in dependence on the laser power due to photobleaching.

Table 4.4. | Two-photon FCS fit values of the 2 mW–7 mW range.

Laser power	Counts [kHZ]	η [kHz]	N	w_r [µm]	w_z [µm]	χ^2
3 mW	19.6411	8.4327	2.329	0.343	0.968	1.41
4 mW	33.8468	14.4795	2.337	0.348	0.902	0.87
5 mW	52.4182	22.3634	2.344	0.343	0.918	0.74
6 mW	71.0921	30.5646	2.326	0.340	0.932	0.89
7 mW	89.9833	38.5897	2.332	0.345	0.797	1.11

4.1.2. Characterization via scanning images

Scan image of fixed HeLa cells were recorded to characterize and benchmark the developed imaging system for live cell imaging. In particular we were interested in testing the correct implementation of the piezo scanning stage, the programmed scanning routine, and the overall alignment of the setup allowing for simultaneous one- and two-photon imaging. Apart from inherent piezo scanning artefacts such as non-linearity, hysterisis and creep effects, the biggest experimental challenges to solve is the synchronization was the imperfect synchronization of the stage movement and the actual image acquisition. While the piezo stage is controlled via a field-programmable gate array (FPGA), the TCSPC cards responsible for counting and assigning the detected photons to pixels are synchronized to the repetition rate of the pulsed femtosecond laser. The communication speed between the computer starting the scanning program and the FPGA card fluctuates on the order of 2 ms–3 ms. This effect by itself leads to a constructed image actually starting at a x-shifted pixel for the whole frame. This experimental obstacle could be successfully compensated by adding an appropriate waiting time for the TCSPC card matching the difference of the communication speed. However, the piezo stage scans each line in the same direction, i.e. at the end of each line the stage moves to original x-position and a shifted y-position. The result is a compressed mirror image on the left-hand side of the shifted starting point, representing the recorded image during the repositioning of the stage. Furthermore, a constant additional pixel shift is introduced between each scanning line. Therefore, an additional waiting time per line would be necessary in order to match the time its takes the piezo stage to return to its original x-position and start the next line scan. The implementation of the latter wait time is not trivial as it varies with experimental settings, such as the number of lines, the size of the scanning area and the total measurement time between different scans. Figure 4.6 shows two examples of raw data images of fixed HeLa cells which feature the encountered artefacts. To correct and prevent these delay times, a new approach is currently implemented, based on a common synchronization via the FPGA. A full implementation and characterzation, however, could not be achieved anymore during

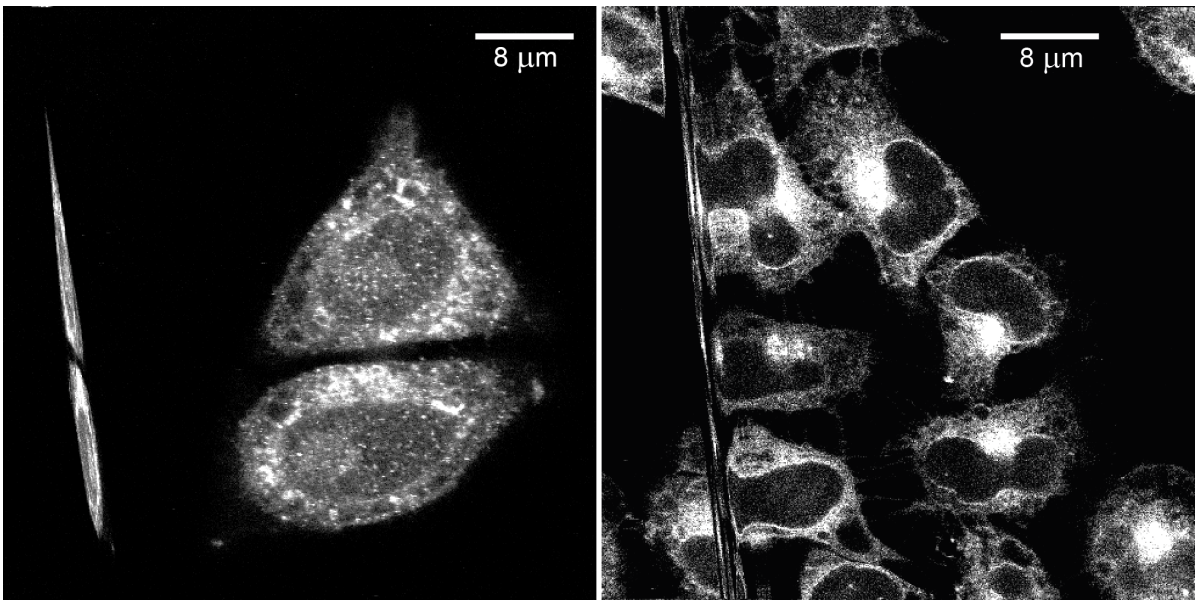

Figure 4.6. | Raw data images including scanning artefacts: Unaltered scan images show a pixel line shift and compressed mirror images due to imperfect synchronization of the piezo stage and TCSPC card. The images were obtained via 532 nm excitation of unstained (left panel) and with WGA488 stained HeLa cells (right panel) using an image acquisition time of 180 s and 512 lines.

this thesis. In order to minimize the scanning artefacts, images were recorded using a long acquisition time of 180 s. Afterwards, the shifted pixels were corrected in post processing procedures of the data. Using the image processing package Fiji (distribution of ImageJ) a transformation matrix was constructed to shift each pixel line with respect to each other by a constant value. Since the degree of the image tilt and the shifted start position is highly reproducible for given scanning parameters, the overall alignment of the three excitation sources (532, 633, 780 nm) could be superimposed. Lateral shifts between scanned images for the three excitations could be successfully corrected by ImageJ. The pixiel shift between 532 and 633 nm was determined by co-localization of simultaneously recorded scan images. Images for 532 and 780 nm excitation were recorded sequentially, as their signal is detected in the same channel. No optical fibers were used for overlapping the different wavelengths and hence each beam bath was aligned separately. The pixel shift was determined by colocalization and the images obtained from 532 nm and 780 nm excitation were not recorded simultaneously because the signal was detected in the same channel. From the ratio of the total number of pixels and the known size of the scan area, the actual distances were obtained and are listed in table 4.5.

Table 4.5. | Calculated x-y-shifts between green, red and two-photon excitation.

Compared exc. wavelength	x-shift [µm]	y-shift [µm]
532 nm ↔ 633 nm	1.16	0.12
532 nm ↔ 780 nm	2.91	0.23
633 nm ↔ 780 nm	4.07	0.61

Although it is challenging to perfectly superimpose three independent laser systems for a collinear excitation of the sample, the determined shifts are sufficiently small to get very similar image information. Considering the drift occurring in successive measurements taking at least 9 min, the overall y-shift (parallel to the scanning axis) is especially small. The x-shift (perpendicular to the scanning axis) is significantly larger. As the incoupled laser lines are centered with respect to the objective, the displacement in x can be assigned to a the scan artefact of an improper placed sample on the piezo stage. Only if the sample is positioned and properly clamped under 90° with respect to the objective's surface, chromatic aberrations and deviations in the scan position are avoided. Very likely is also the faster acquisition speed in x-direction introduced by the scanning mechanism, i.e. the sample itself is more likely to drift in x-direction than in y-direction. In both cases, however, the x- and y- shift can be compensated. Figure 4.7a and 4.7b shows two tilt-corrected scan images of WGA488 stained HeLa cells recorded in the green channel and excited by the 532 nm and 780 nm laser. The composite image after colocalization is shown in figure 4.7c. Considerably less background signal can be observed in case of two-photon excitation. A complete overview including the brightfield options and 633 nm excitation and is illustrated in figure 4.8 which shows images of unstained HeLa cells. Hence, the disparity in the image quality of each excitation method is mainly caused by the different efficiency of generating autofluorescence. In particular, 4.8e demonstrates the strong absorption of two 780 nm photons since the compounds emitting autofluorescence (NAD(P)H, collagen, riboflavin, aromatic molecules) primarily absorb in the UV to blue range.

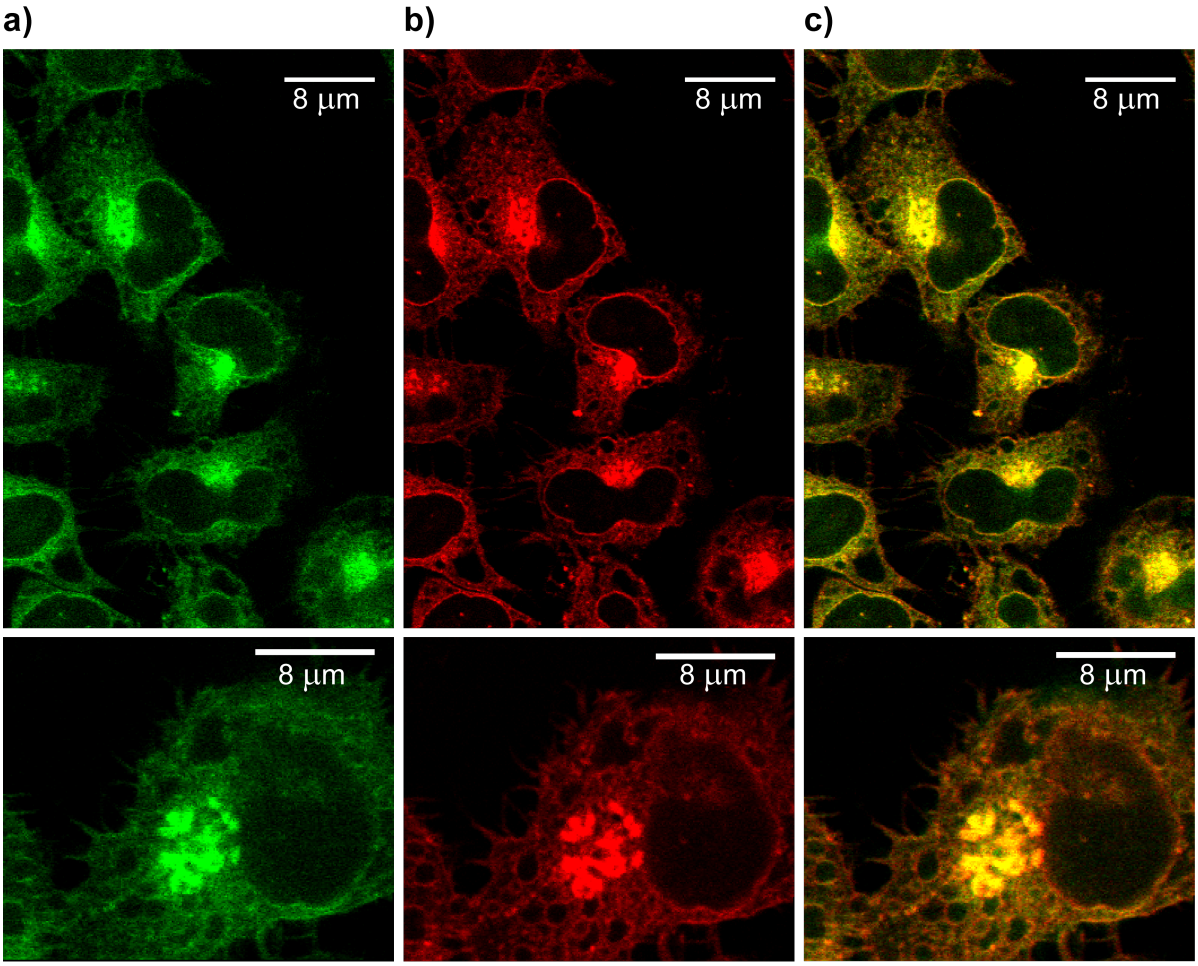

Figure 4.7. | Scan images of stained HeLa cells: (a) Scan image obtained with 532 nm excitation after line shift correction. (b) Scan image obtained with 780 nm excitation after line shift correction. (c) Colocalized image of (a) and (b). Images were recorded in the green channel with 180 s acquisition time and 512 lines.

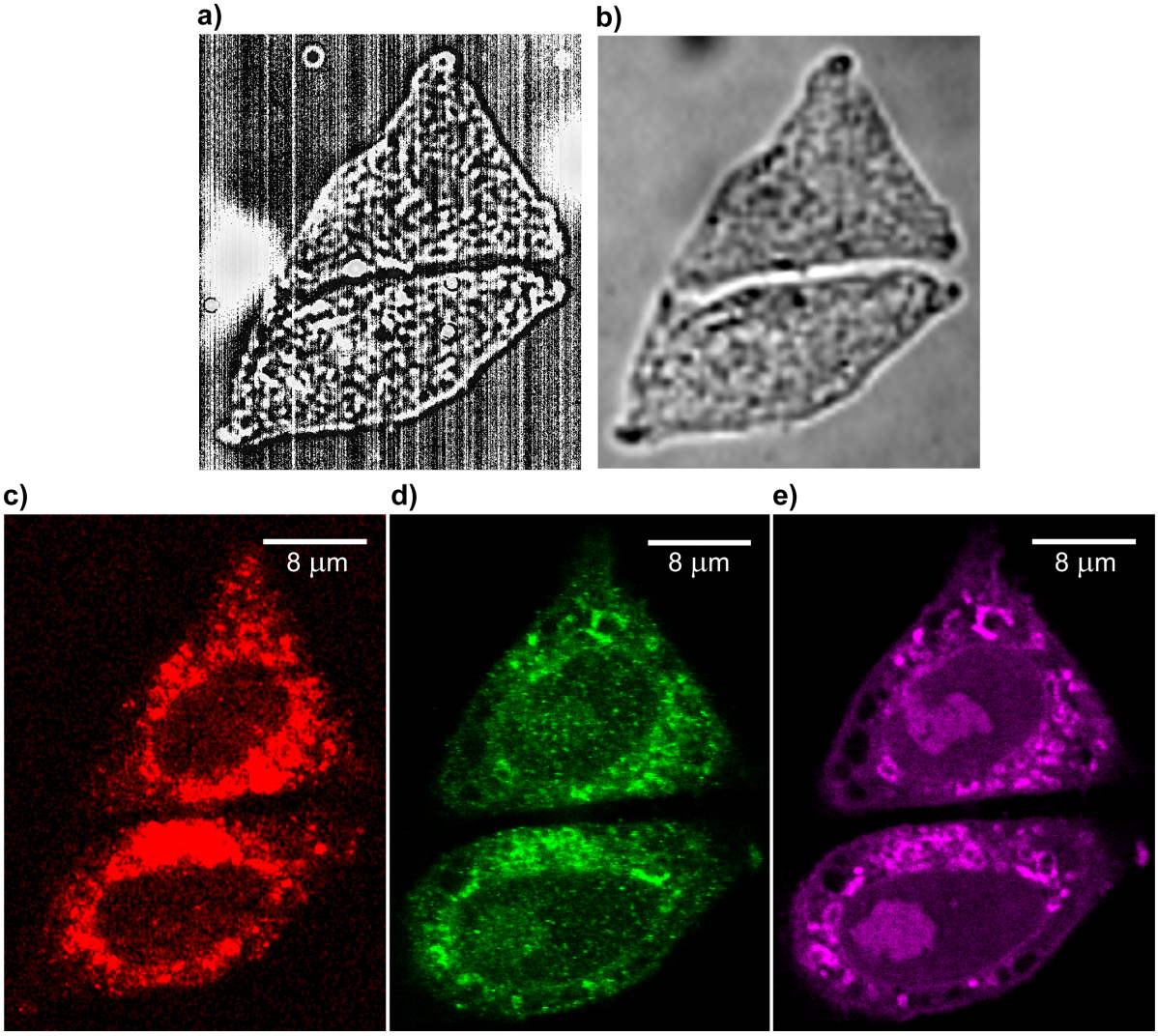

Figure 4.8. | Scan images of unstained HeLa cells: (a) Brightfield image of the CMOS camera. (b) Brightfield image of the Andor camera. (c) 633 nm excitation. (d) 532 nm excitation. (e) 780 nm excitation.

4.2. Raman measurements and simulations

4.2.1. Raman spectra

The metabolism and storage of sugars inside cells is highly complex. A vast number of different monosaccharides can be used by cells for various biological functions. In this work, the priority was to study the most important sugar derivates (see section 3.3.1 and 3.3.2) used as an energy source and as building blocks to create complex glycans via glycosidic linkages. The measured Raman spectra of these sugars are presented in the following in order to constitute the difficulty of differentiating these sugars via spontaneous Raman scattering, especially under natural conditions in solution. Furthermore, Raman spectra of common sugars and solvents exhibit similar vibrations with respect to Raman spectra of living cells and also feature the same Raman-silent region in the range of 1800 cm^{-1} to 2800 cm^{-1}. Hence, to get an idea of the Raman shifts and intensity ratios of promising Raman labels such as alkyne, azide or deuterated moieties, Raman spectra of solvents and Raman-labeled sugars are compared with their untagged counterparts. The measured spectra also serve as the basis for simulations used to estimate the detection limit and test the performance of quantitative analysis techniques (see section 4.2.2).

All monosaccharides mainly consist of carbon, oxygen and hydrogen atoms. Accordingly, they all show Raman bands in similar regions depending on the different vibrational modes. The most important types of vibrations and Raman shift regions are listed in table 4.6.[88] C=O vibrations only exist in acetylated sugar molecules. O-H vibrations are covered by water.

Table 4.6. | Characteristic vibrations in Raman spectra of monosaccharides.[88]

Type of vibration	Region of Raman shift
C-C vibrations	800 cm^{-1} – 1200 cm^{-1}
C-H stretching	2800 cm^{-1} – 3100 cm^{-1}
C-H deformation	1380 cm^{-1} – 1470 cm^{-1}
C-OH stretching	1100 cm^{-1} – 1210 cm^{-1}
C-OH deformation	750 cm^{-1} – 800 cm^{-1}
C=O stretching	1550 cm^{-1} – 1800 cm^{-1}
O-H stretching	3200 cm^{-1} – 3800 cm^{-1}
O-H deformation	1600 cm^{-1} – 1700 cm^{-1}

Figure 4.9a displays the structure of the most relevant monosaccharides D-glucose, D-galactose and D-mannose. The corresponding normalized Raman spectra in solid phase and in solution (figure 4.9b-c) at 1 M concentration show the significant broadening as well as intensity and spectral shifts of individual peaks caused by the solvation in water. In particular, the characteristic galactose peaks in solid phase at 1032 cm^{-1} and 1280 cm^{-1} are not observable in solution and galactose is nearly indistinguishable from mannose. Only glucose could be cleary identified in a sugar mixture by the strong peak at 920 cm^{-1}.

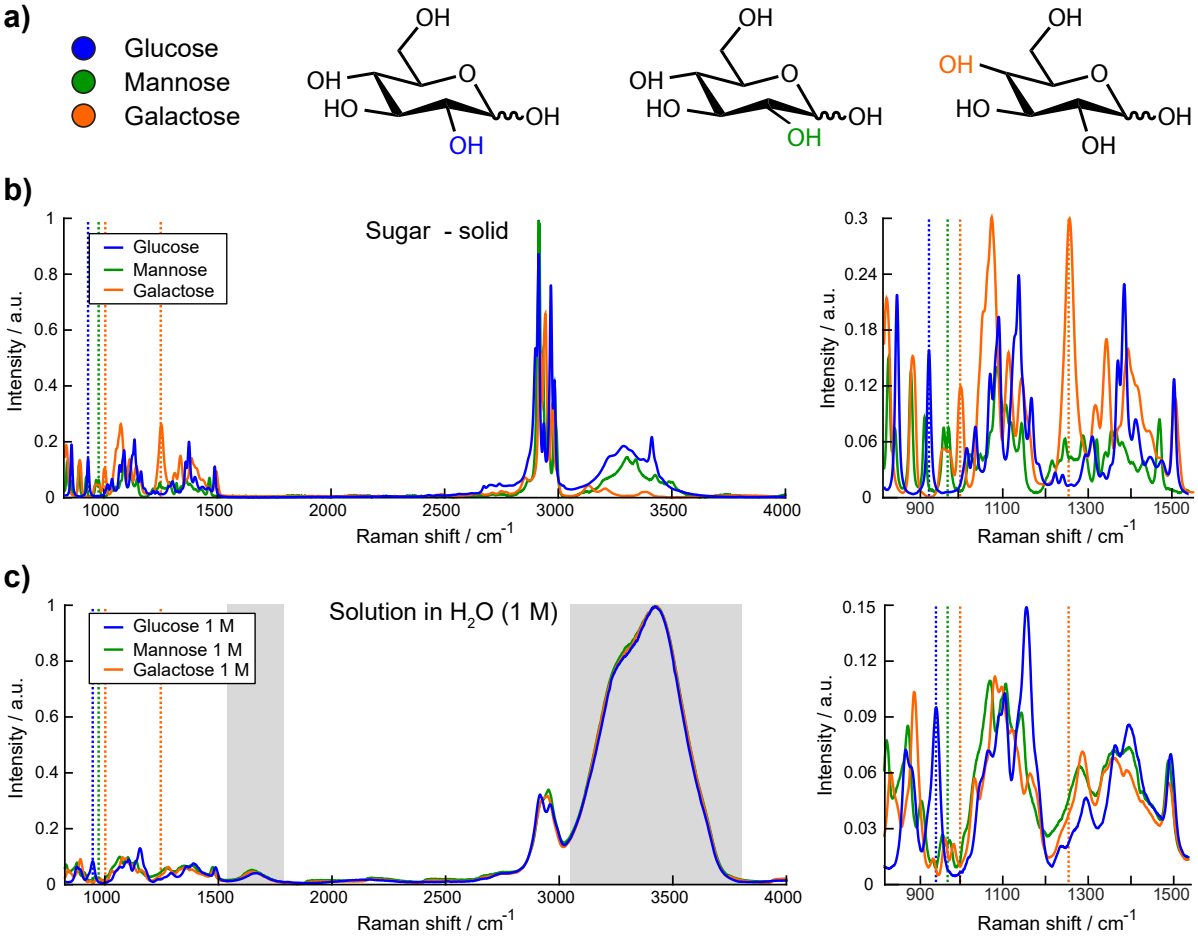

Figure 4.9. | Raman spectra of common sugars: a) Chemical structures of glucose, mannose and galactose. b) Corresponding Raman spectra in solid phase. c) Corresponding Raman spectra in water at 1 M concentration. The insets show the zoomed in characteristic regions. O-H vibrations caused by water are depicted in grey background.

Similar circumstances can be recognized in the normalized Raman spectra of *N*-acetyl-D-glucosamine (GlcNAc), *N*-acetyl-D-mannosamine (ManNAc) and *N*-acetyl-D-galactosamine (GalNAc), which are used as building blocks for glycans in the endothelial cell membrane (figure 4.10). The Raman spectra show strongly overlapping peaks varying in intensity. Compared to normal sugars, the main difference is the high intensity detected in the C-H stretch region (2800 cm^{-1} – 3100 cm^{-1}) caused by the CH_3 moiety. Additionally, the strong C=O stretching vibration can be observed for all acetylated sugars at ~1642 cm^{-1}. This Raman band contributes to the so-called amide l region (1640 cm^{-1}–1700 cm^{-1}) of living cells and is therefore convoluted with various other compounds.[89,90]

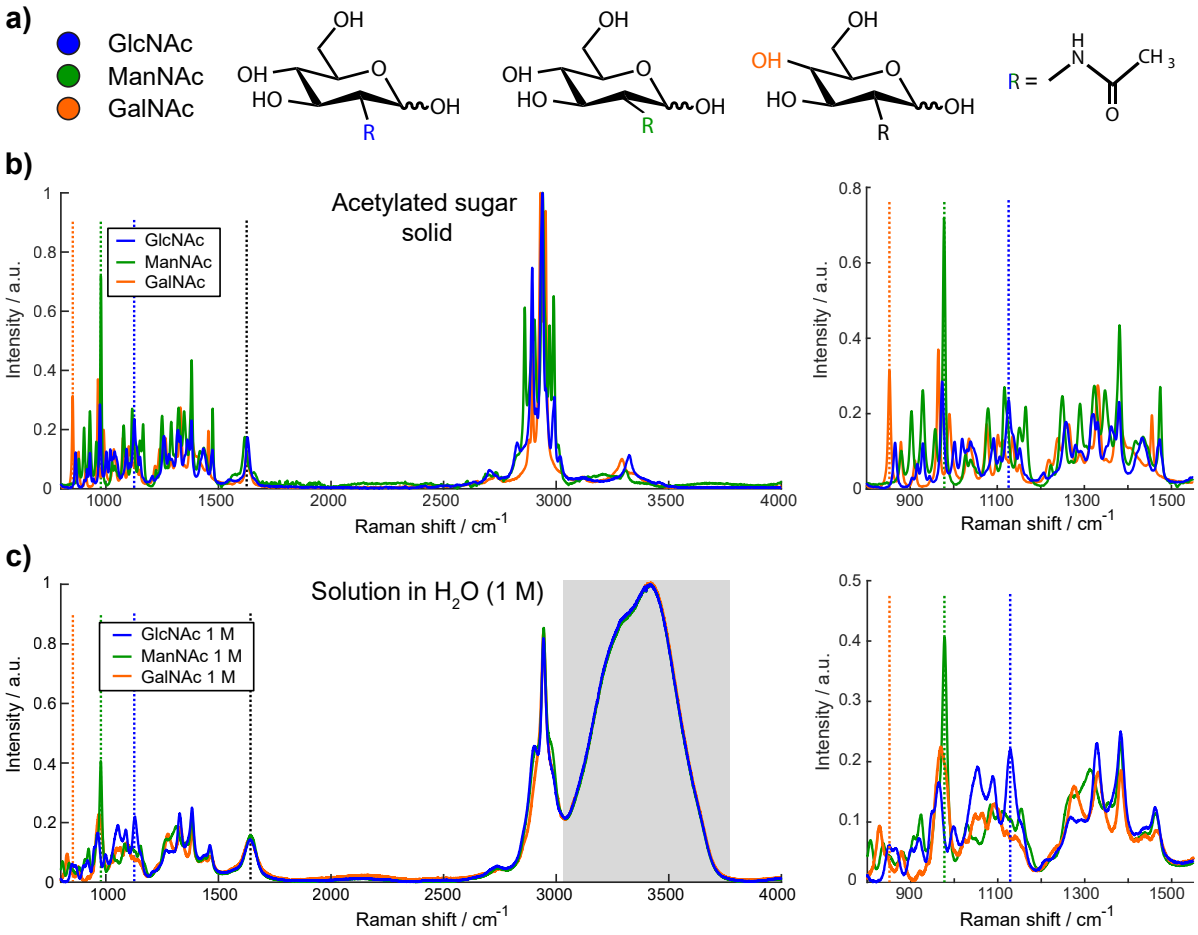

Figure 4.10. | Raman spectra of acetylated sugars: a) Chemical structures of *N*-acetyl-D-glucosamine (GlcNAc), *N*-acetyl-D-mannosamine (ManNAc) and *N*-acetyl-D-galactosamine (GalNAc). b) Corresponding Raman spectra in solid phase. c) Corresponding Raman spectra in water at 1 M concentration. The insets show the zoomed in characteristic regions. O-H vibrations caused by water are depicted in grey background.

Radioactively methylated sugars are used to study the up- and downregulation of the blood-brain barrier glucose transporter since they directly compete with glucose transport.[91,92] Characteristic peaks of in solid phase at 830 cm^{-1} and 875 cm^{-1} can not be resolved in solution in the presence of other compounds. This also applies to the characteristic peaks of methyl β-D-glucose (e.g. 903 cm^{-1}) and methyl β-D-mannose (980 cm^{-1}). Compared to normal sugars (figure 4.9), an increased intensity in the C-H stretch region (2800 cm^{-1} – 3100 cm^{-1}) and additional peaks at 2849 cm^{-1} and 3014 cm^{-1} can be observed due to the CH_3 moiety. For Raman spectroscopy however, sole methylation would not be adequate to distinguish these sugars from other substances in living cells.

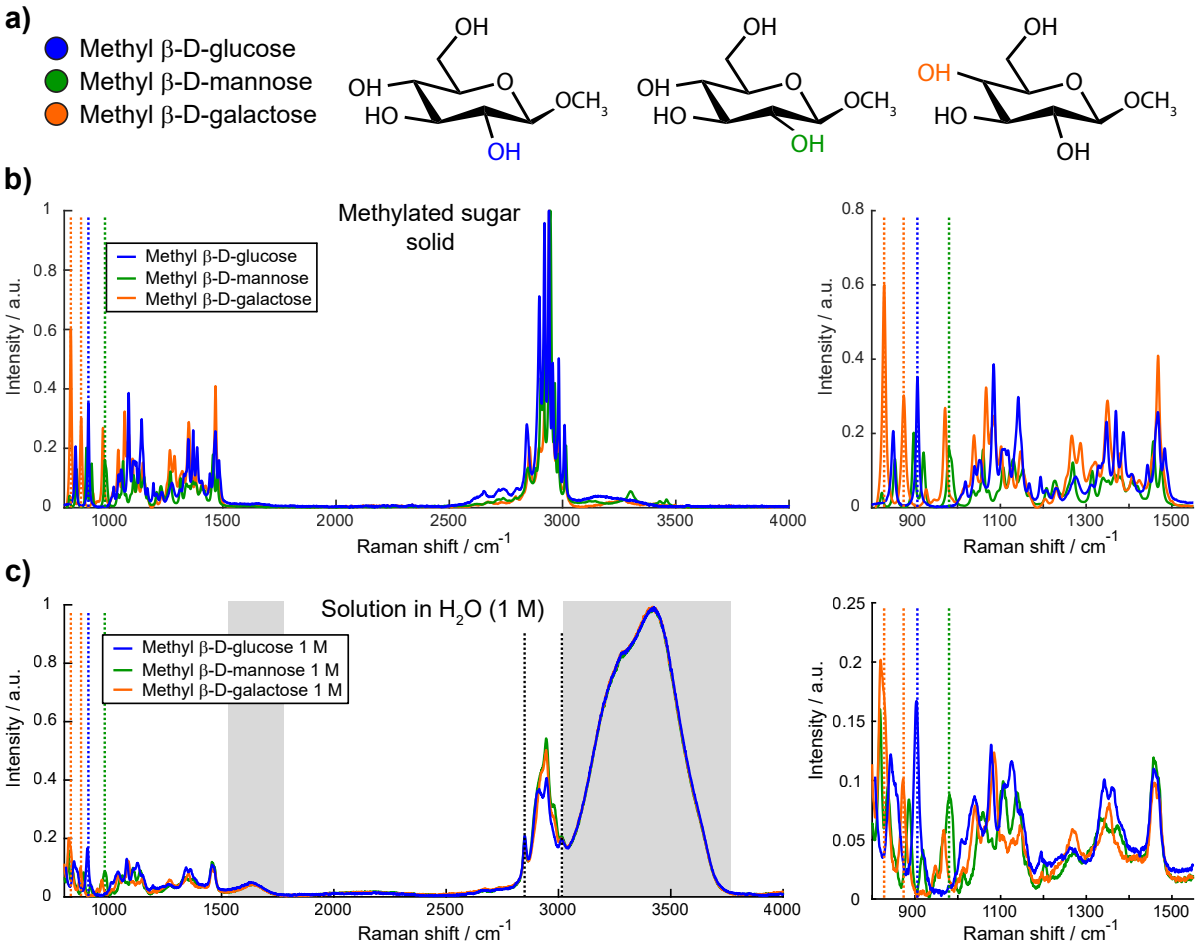

Figure 4.11. | Raman spectra of methylated sugars: a) Chemical structures of methyl β-D-glucose, methyl β-D-mannose and methyl β-D-galactose. b) Corresponding Raman spectra in solid phase. c) Corresponding Raman spectra in water at 1 M concentration. The insets show the zoomed in characteristic regions. O-H vibrations caused by water are depicted in grey background.

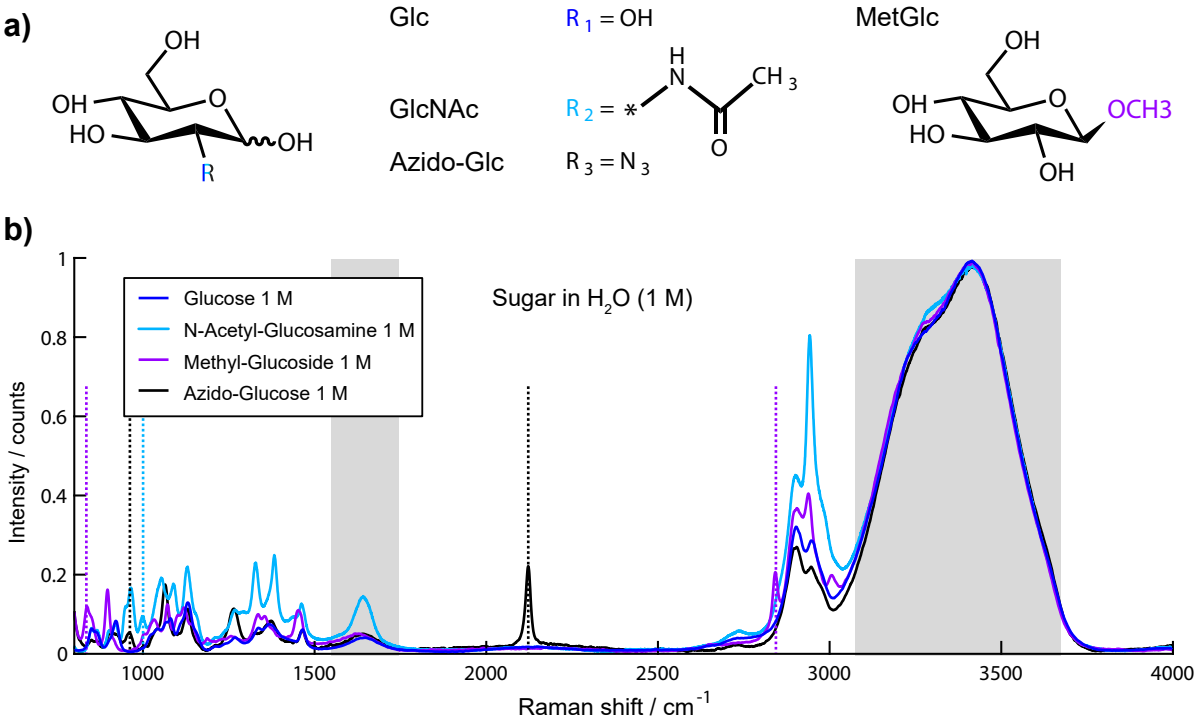

Figure 4.12. | Raman spectra of glucose derivates: a) Chemical structures of D-glucose, *N*-acetyl-D-glucosamine (GlcNAc), 2-Azido-2-deoxy-D-glucose (N_3-Glc) and methyl β-D-mannose . b) Corresponding Raman spectra in water at 1 M concentration. The spectrum of N_3-Glc shows the strong azide stretching vibration at 2123 cm^{-1} in the Raman-silent region of living cells. O-H vibrations caused by water and C=O stretching vibrations are depicted in grey background.

Multiple Raman tags are qualified for the quantification of monosaccharides. Moieties such as alkyne, nitrile, azide or deuterium have unique Raman bands in the desired region (1800 cm^{-1} – 2800 cm^{-1}) which do not overlap with Raman scattering from any endogenous molecule in live cells. The synthesis of alkyne and nitrile labeled sugars was outside the scope of this work since it involves synthetic chemistry methods, e.g. ketone-aminooxy/hydrazide ligation[93,94], Staudinger ligation[95] or Michael addition.[96] Azide sugars, however, are commercially available and could easily be used for experiments. Figure 4.12 provides an overview of normalized Raman spectra of examined glucose derivates including 2-Azido-2-deoxy-D-glucose (N_3-Glc) at 1 M concentration. N_3-Glc shows Raman bands at 856 cm^{-1}, 911 cm^{-1}, 960 cm^{-1}, assigned to skeletal C-C vibrations. The strong peaks at 1064 cm^{-1} and 1130 cm^{-1} could be assigned to exocyclic C-O and C-OH vibrations, respectively.[97] Peaks at 1264 cm^{-1}, 1372 cm^{-1}, 1468 cm^{-1} are assigned to CH_2 and CH_3 deformations whereas peaks at 2906 cm^{-1} and 2946 cm^{-1} correspond to CH stretching vibrations. Most importantly, N_3-Glc exhibits the strong azide stretching vibration at 2123 cm^{-1} withing the Raman-silent region of cells.

In addition to azide sugars, it was possible to examine and experimentally utilize deuterated methyl α-D-glucoside, which was synthesized in collaboration with Adrian Müller-Deku, M.Sc (Group of Thorn-Seshold, PhD). Assuming a diatomic molecule, deuterium substitution of hydrogen leads to a doubled reduced mass of and thus to a decreased Raman shift of $\sqrt{2}$. This phenomenon can be clearly observed in the Raman spectrum of deuterated methyl α-D-glucoside, showing the strong C-D stretching vibration in the range of 2060 cm^{-1} – 2270 cm^{-1} and C-D deformations at 831 cm^{-1} and 963 cm^{-1}. Since methyl α-D-glucoside was deuterated site-selectively at the carbon positions only a weak signal for O-D stretching vibrations (~ 2400 cm^{-1} – 2600 cm^{-1}) is obtained.

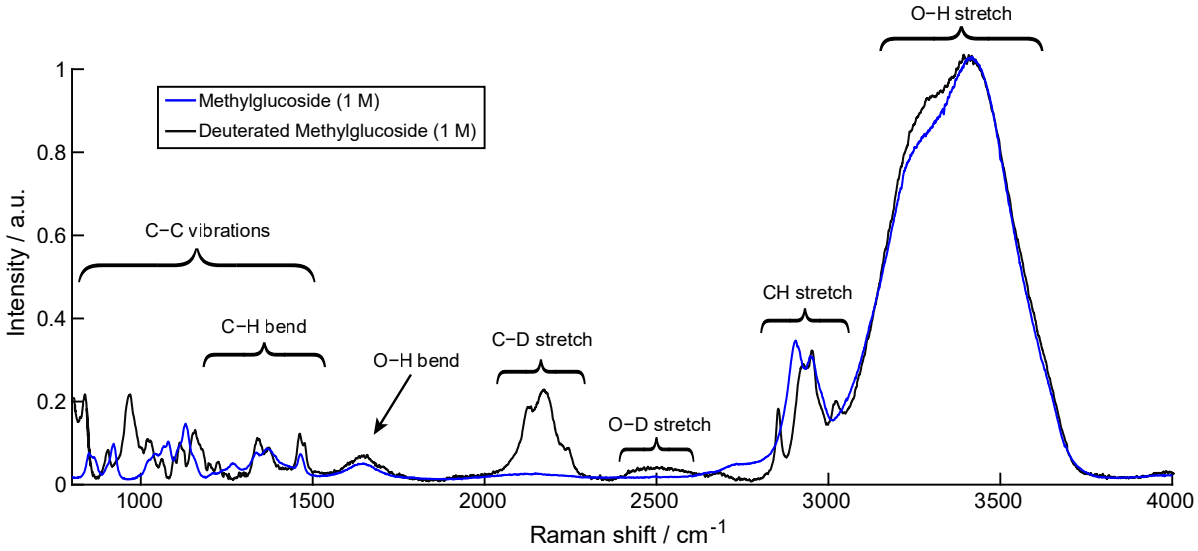

Figure 4.13. | Raman spectrum of deuterated methyl α-D-glucoside: Comparison of undeuterated and deuterated methylglucoside at 1 M concentration in H_2O showing the $\sqrt{2}$ Raman shift decrease caused by deuterium substitution. This shift results in the strong C-D stretching vibration in the range of 2060 cm^{-1} – 2270 cm^{-1} in the Raman-silent region of living cells.

The C-D band of deuterated methyl α-D-glucoside, is rather broad and shows similar signal strength to the C-H vibration. When compared to 2-azido-2-deoxy-D-glucose (N_3-Glc), N_3-Glc features an immensely sharper Raman resonance in the cell-silent region, which facilitates its detection in in presence of further Raman-tagged sugars. As alkynes are amongst groups with highest Raman cross-sections, the simplest carbohydrates carrying an alkyne group, namely propyn-1-ol and butyn-1-ol, were measured in comparison to known solvents. The spectra of ethanol and ethylenglycol were used in simulations of multicompound spectra described in the following section (section 4.2.2). Figure 4.14 shows the Raman spectra of solvents normalized to 1 M concentration. In particular, propyn-1-ol and butyn-1-ol exhibit the C≡C moiety giving rise to the very strong signal at 2123 cm^{-1} which can be used to detect alkyne tagged sugars inside living cells. Both substances possess a large Raman cross section and signals that are 2-3 fold higher than their C-H stretch vibration. Therefore, alkynes are the most promising Raman-labels for the quantification of sugars at low concentrations since they can significantly enhance the detection sensitivity.

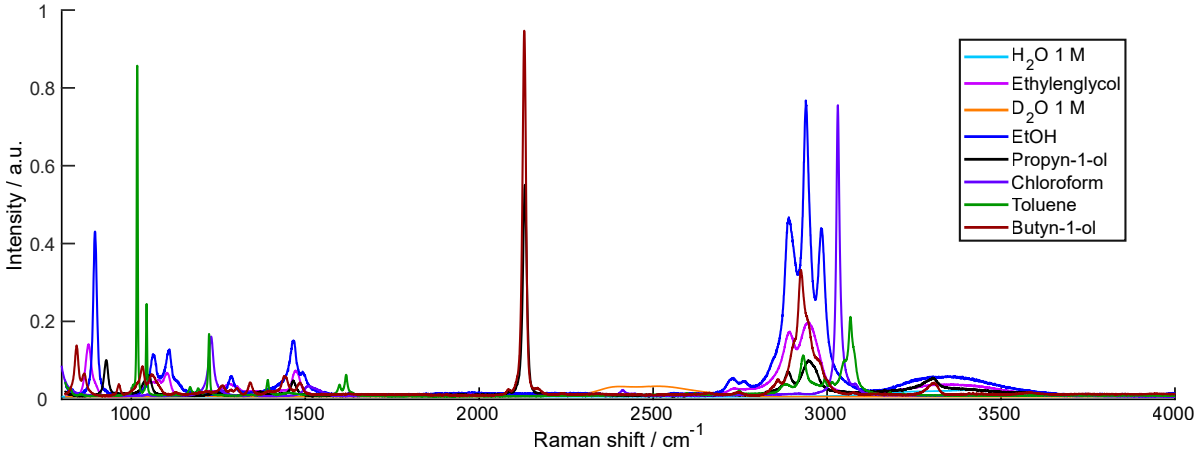

Figure 4.14. | Normalized Raman spectra of solvents: Overview of solvent Raman spectra normalized to 1 M concentration. Propyn-1-ol and butyn-1-ol show the very strong C≡C stretching vibration at 2123 cm^{-1} in the Raman-silent region of living cells.

4.2.2. Estimation of the detection limit

For estimating the detection limit of a Raman labeled sugar in cells, at first spontaneous Raman spectra of Raman tagged sugars were recorded at a concentration of 1 M in water. (see section 4.2.1 for results and 3.3.1 for experimental details). To ensure comparability, spectra were taken under identical conditions and experimental care was take to ensure the following premises:

- A constant excitation power of 1.8 W and excitation wavelength of 532 nm used.
- All spectra are acquired with constant spectral resolution and constant integration time.
- Background signal remains constant.

Two examples of 0.1 M 2-azido-2-deoxy-D-glucose (N_3-Glc) simulated spectra with added noise (SNR = 9) are shown in figure 4.15a-b according to the two examined scenarios of a single peak spectrum and a multicompound spectrum. Beside N_3-Glc, the multicompound spectrum contains glucose, galactose, mannose, methylglucose, methylgalactose, methylmannose, ethanol and ethylenglycol. While the accuracy of normal linear decomposition to correctly identify the original spectral input mainly depends on the quality of the used reference spectra, PCA analysis is mostly influenced by the total number of spectra in the data set and the chosen rank in approximation, , i.e. the number of incorporated principle components. Figure 4.15c-d displays two PCA biplots of azidoglucose for varying concentrations of sugar and chemical background. Figure 4.15c suggests that the variation caused by the single azide stretch peak can be reasonably well described by component 1 as it can be completely separated from the background, which is described solely by component 2. However, this changes with increasing noise and decreasing concentration such that the variation of the azide peak is best described by component 2 similar to the loading plot for a multicompound spectrum shown in figure 4.15d. Thus, a rank 2 approximation was chosen for both scenarios. Both analysis methods were applied to single and multicompound spectra varying in SNR (1-18) and concentration (µM-mM). The corresponding standard deviation of the accuracy in percent is shown in figure 4.16 for each method. For normal linear decomposition (figure 4.16a-b), the limit of reliability is reached at ~10^{-4} M concentration of N_3-Glc for high SNR values above 10 and at ~10^{-3} M for SNR values below 0.5. Using PCA this limit can be pushed to a concentration of ~10^{-5} M for SNR values above 10 (figure 4.16c) and ~5×10^{-5} M for SNR values below 0.5 (figure 4.16d) which resembles physiological conditions. Interestingly, the limits of the analysis methods behave differently when comparing the results for multicompound and single peak spectra. In case of linear decomposition a slight decrease in accuracy is obtained

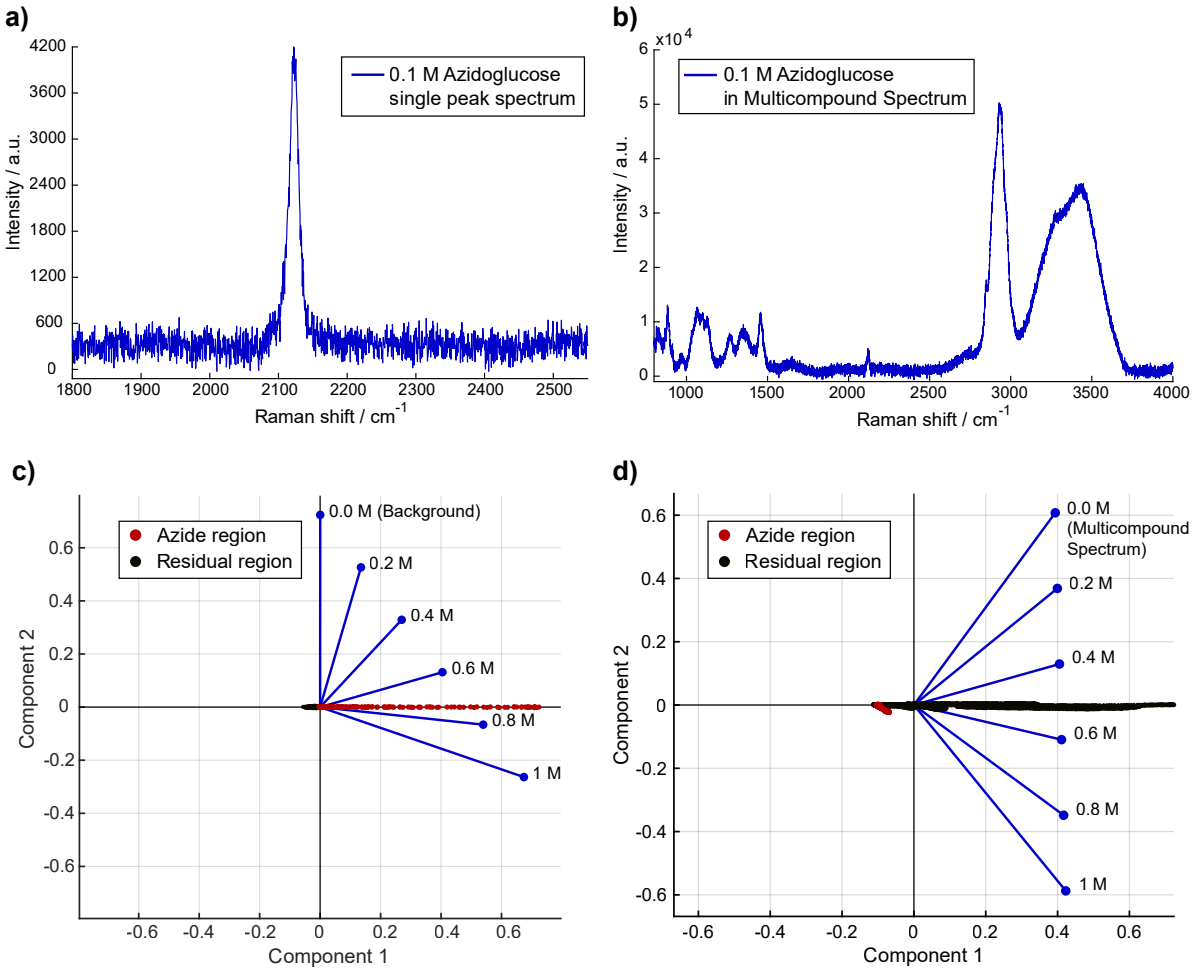

Figure 4.15. | Simulated spectra and PCA biplots: a) Simulated single peak spectrum of 0.1 M azidoglucose (N_3-Glc) at the range of the characteristic azide stretch vibration. b) Simulated broad-band multicompound spectrum containing 0.1 M N_3-Glc. c) PCA biplot of single peak spectra with different azidoglucose concentrations. d) PCA biplot of multicompound spectra containing different concentrations of N_3-Glc. Blue lines represent the individual loadings for each spectrums and the direction of maximum variance. Dots are the corresponding principle components of the whole data set. The characteristic azide stretch region (2000 cm^{-1}–2200 cm^{-1}) is displayed in red.

if only a single peak is analyzed, most likely due to the close resemblance of the azidoglucose spectrum to the background and hence less linear equations exist for the differentiation of these two components. In contrast, the accuracy of PCA slightly improves for the single peak spectrum since the variation of one peak against a flat constant background can be clearly separated. However, it must be noted that these results are not generally applicable as they are only valid for the two simulated scenarios and thus primarily give an approximation of the detection limit. Furthermore, PCA thrives on the size of the analyzed dataset whereas

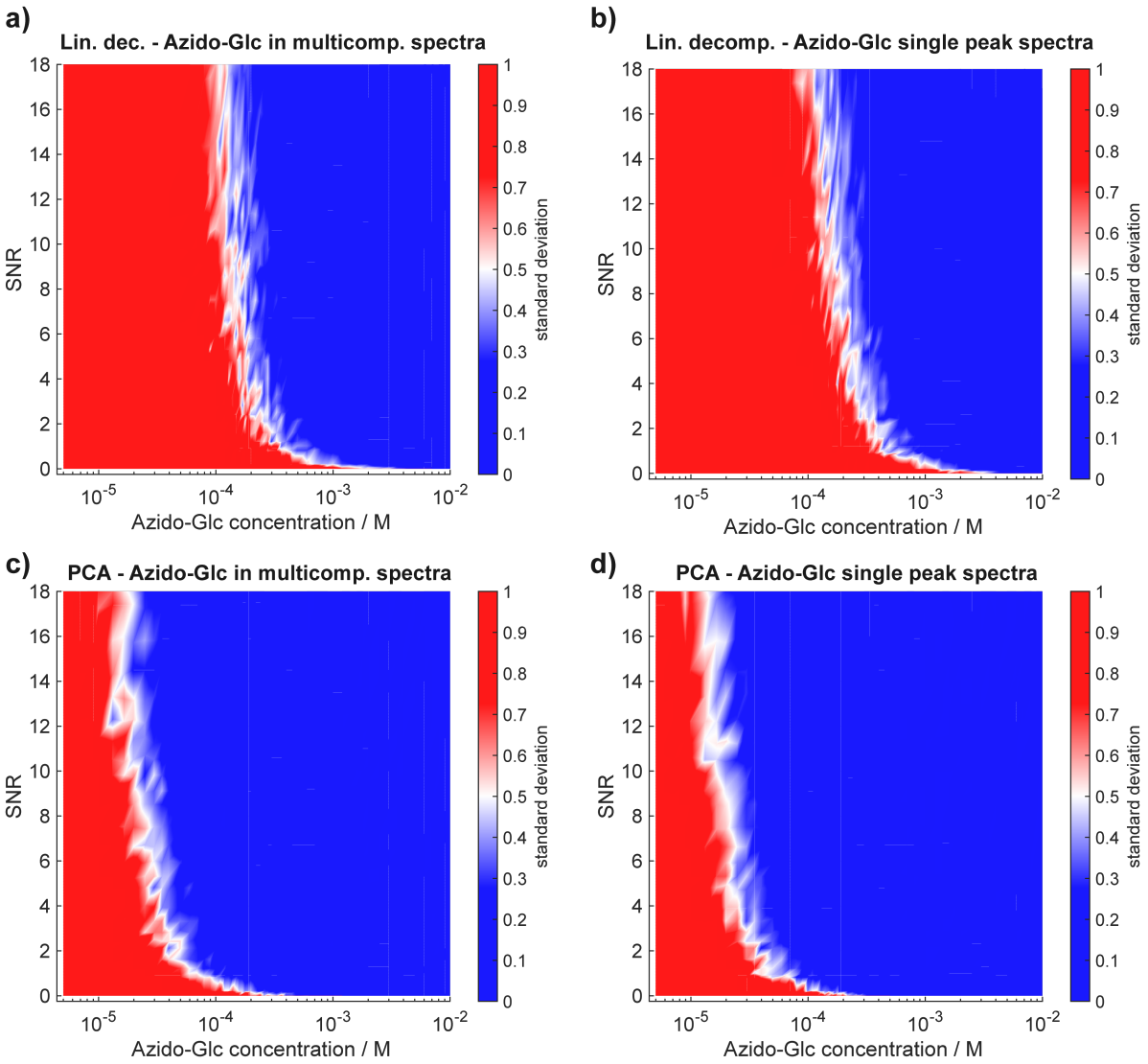

Figure 4.16. | Analysis of simulated Raman spectra via linear decomposition and PCA: Standard deviations of quantitative analysis of azidoglucose (N_3-Glc) in dependence of SNR and concentration. a) Linear decomposition of N_3-Glc in multicompound spectra. b) Linear decomposition of N_3-Glc in single peak spectra. c) PCA of N_3-Glc in multicompound spectra. d) PCA of N_3-Glc in single spectra.

linear decomposition can only be applied to one spectrum at a time and does not gain any benefit from large datasets. The influence on the analysis quality of parameters such as the peak widths, flatness of the background and eventual phase shift must also be considered. If only one peak of interest is observed PCA is a highly useful tool for signal denoising and can be accompanied by methods which include peak fitting algorithms. Overall, considering naturally occurring sugar concentrations in the µM and mM range, the limits reached by PCA are promising and confirm the feasibility of the project.

4.2.3. Live Cell Measurements

Sugar serves as the main energy source in living cells. To visualize its cellular uptake by Raman scattering, live cell imaging was conducted using a inverted, confocal scanning Raman microscope (see section 3.3.3) in collaboration with (Group of Prof. Dr. C. Haisch, TUM München). The main goal in these proof-of-concept experiments was to investigate the survivability of HeLa cells grown with Raman tagged sugars and to show the feasibility of monitoring sugar uptake into the cell. The main subject of interest was the overall effect of incubating living HeLa cells with Raman labeled sugars and if the eventually metabolized sugar can be detected inside the cell. Two types of sugars were used for the experiments, namely N-azidoacetylmannosamine (ManNAz) and deuterated methylglucose. Although cells were successfully cultured using deuterated methylglucose no confocal Raman scans could be performed due to the limited amount of measurement time. Here, the data analysis and evaluation of the experiment using ManNAz is presented. The excitation power of the red laser (633 nm) was set to 20 mW with integration time of 0.1 s for each pixel for all measurements. For each spectrum an array of 1600 elements (data points) was be obtained at a detection region of 643 cm^{-1}–3113 cm^{-1} which corresponds to a spectral resolution of ~1.54 cm^{-1}. HeLa cells simultaneously cultured with 20 mM D-glucose dissolved in growth medium served as reference samples. An example is shown in figure 4.17 which also depicts the applied analysis procedure. One Raman spectrum per 1 μm^2 was recorded over a scan area size of 60×80 µm resulting in a total of 4800 spectra. Figure 4.17b shows the complete data set in a PCA biplot after the correction of outlier spectra. Since the principal components (colored dots) represent the maximum amount of variance contained in all spectra of the data set, spectral regions of interest were examined. A large variance can be directly observed in the CH-stretch region (2800 cm^{-1}–3100 cm^{-1}, green dots) and the amide l region (1640 cm^{-1}–1700 cm^{-1}, red dots) mainly caused by C=O-vibrations of polypeptides.[89,90] The spectral region of the azide stretch vibration (2050 cm^{-1}–2150 cm^{-1}) is represented by purple dots and shows no change in variance. The Raman map was constructed by integrating the intensity of the CH-region of each spectrum as a function of spatial coordinate (figure 4.17d). In order to calculate an average spectrum of the cell and the outside region, the spectra were assigned to either the cell or the surrounding medium (figure 4.17c). The distinction between spectra was made by a standard deviation threshold of the CH-stretch intensity, which was set to 1.9 fold deviation for the cell.

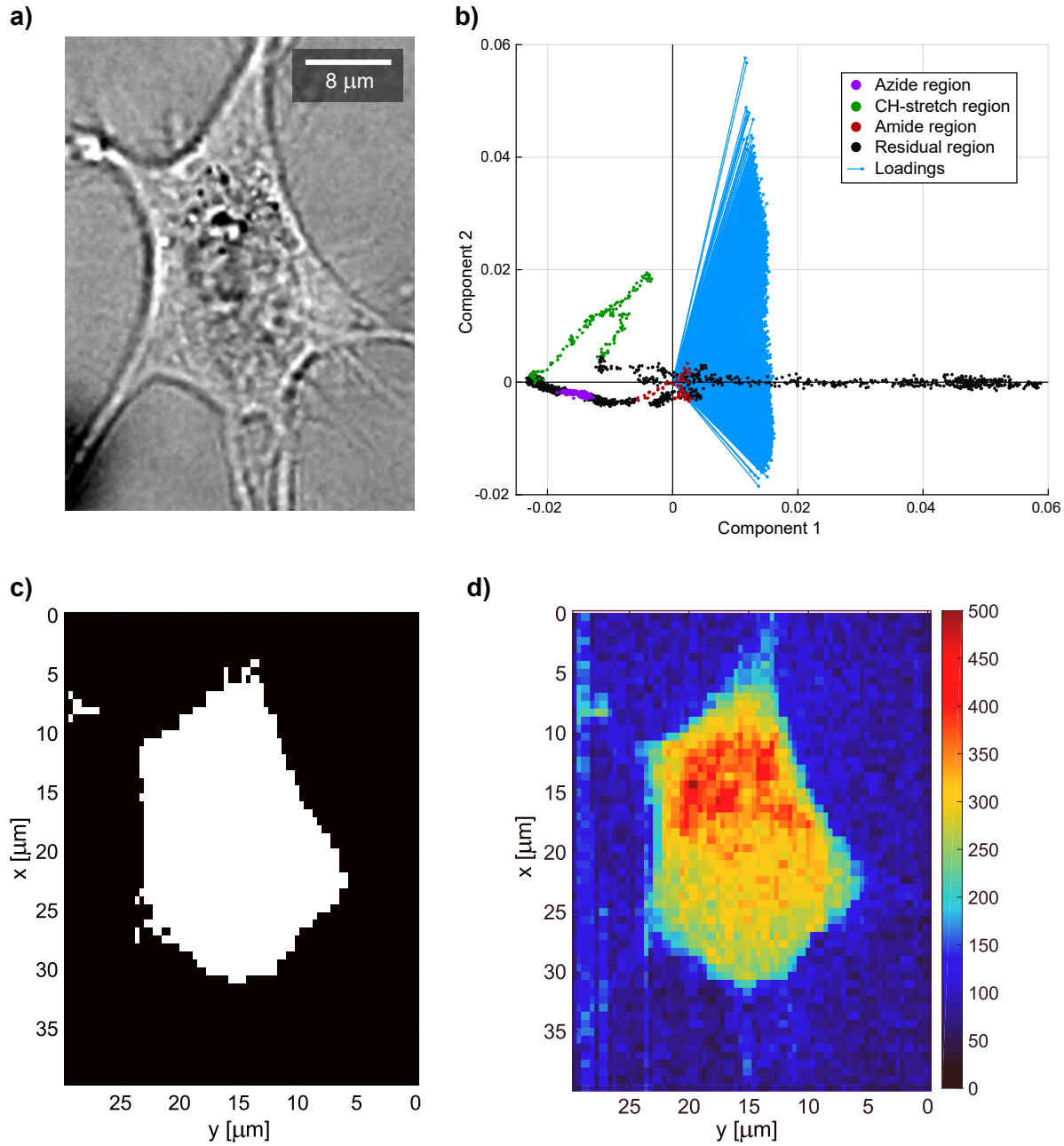

Figure 4.17. | Analysis of HeLa cell cultured with 20 mM **D-glucose:** a) Widefield image of scanned area. b) PCA biplot of the obtained data set after removal of outliers. c) Selected pixels (white) fulfilling the set intensity threshold of the CH-stretch region for calculating the average spectrum of the cell. d) Raman map of the cell. The colormap represents the integrated intensity of the CH-stretch region (2800 cm^{-1}–3010 cm^{-1}).

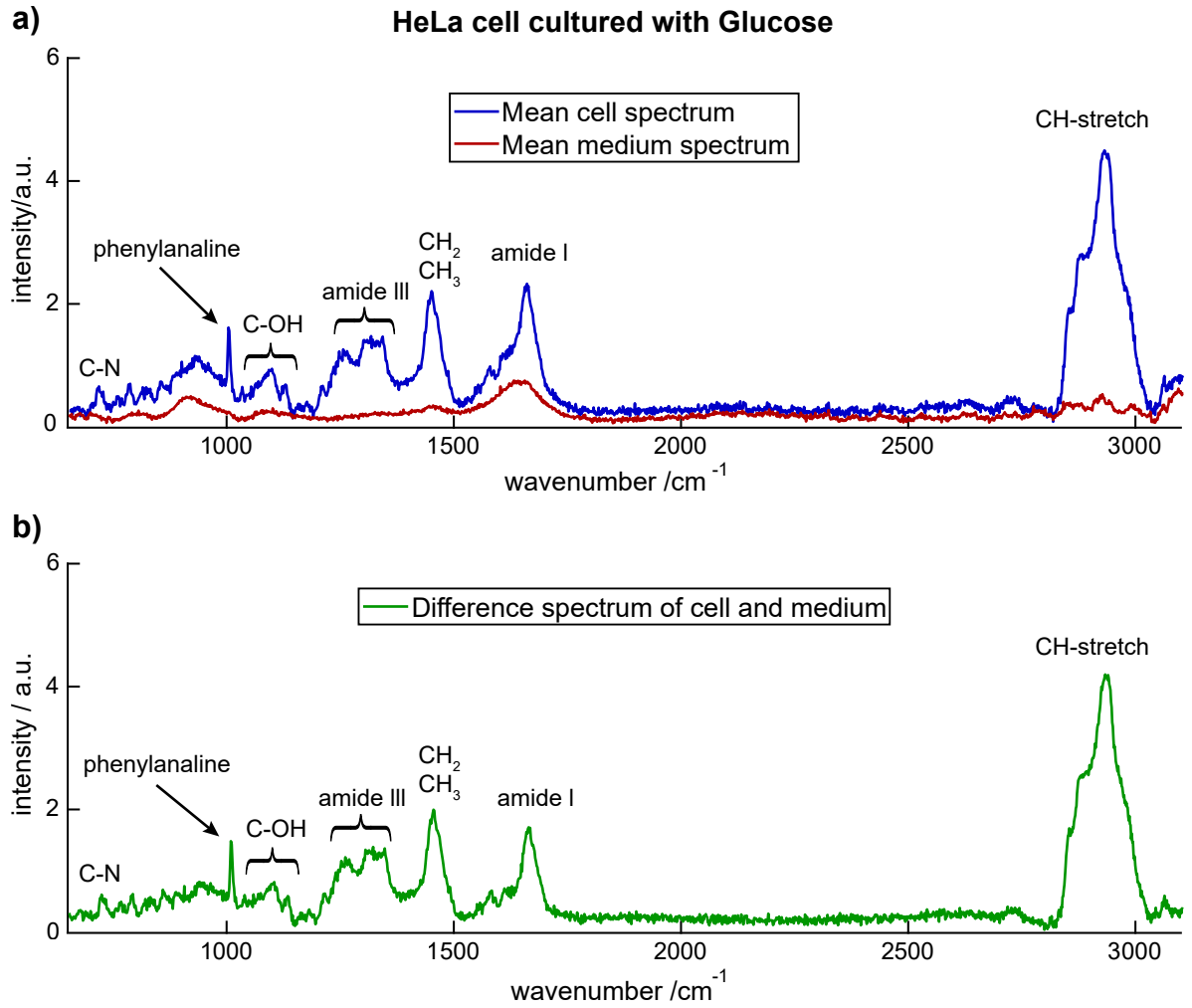

Figure 4.18. | Average spectra of HeLa cell cultured with 20 mM **D-glucose:** a) Mean spectra of the selected pixels. b) Difference spectrum of cell and residual spectrum.

The obtained mean spectra and the difference spectrum of cell and medium (figure 4.18) show the amide l vibrations at 1657 cm^{-1}, the strong CH_2 and asymmetric CH_3 vibration at 1447 cm^{-1}, broad peaks in the amide lll region 1200 cm^{-1}–1340 cm^{-1}, the broad C–OH peak at 1085 cm^{-1} and the C–N stretch vibration at 715 cm^{-1}. The sharp peak at 1000 cm^{-1} is caused by the aromatic ring deformation of the amino acid phenylalanine.[29] All observed peaks represent vibrations of lipids and proteins.

The confocal Raman scan and data analysis of a HeLa cell incubated with ManNAz for one hour and washed with PBS afterwards is shown in figure 4.19. Raman spectra were recorded with the same settings over a scan area of 50×100 µm yielding 5000 spectra. The PCA biplot after correction of outlier spectra reveals that no azide stretch vibration in the range of 2050 cm^{-1}–2150 cm^{-1} was detected for the first two components (figure 4.19b). For all components greater than two, the explained variance flattens to ~ 0.2 % and hence were assigned to random noise. The calculated mean spectra and the difference spectrum (figure 4.20) show the amide l vibrations at 1655 cm^{-1}, the strong CH_2 and asymmetric CH_3 vibration at 1447 cm^{-1}, broad peaks in the amide lll region 1200 cm^{-1}–1340 cm^{-1}, the broad C–OH peak at 1083 cm^{-1} and the C–N stretch vibration at 713 cm^{-1}. The sharp peak at 1000 cm^{-1} is caused by the aromatic ring deformation of the amino acid phenylalanine. The calculated mean spectra (figure 4.20) show no significant difference the spectra obtained from the cell incubated with glucose. Various reasons could inhibit the detection of the azide stretch vibration and additional experiments would have to be performed to get further insight. Although the incubation with ManNAz did not seem to influence the HeLa cells in an observable manner the question remains if ManNAz was actually metabolized and built into the membrane or if it could merely not be detected. Since the experiment could only be carried out once and due to the limited amount of data, no definitive answer can be given at this point. Regarding the cell preparation, parameters such as incubation time and the concentration of the Raman-labeled sugar in the growth medium certainly play an important role. Furthermore, the scan settings could be adjusted for optimal detection sensitivity, e.g. the laser excitation power or the integration time per pixel. The potential damage inflicted on the measured cell must be considered if the overall exposure of the laser is increased. Another option would be to use a 532 nm laser to increase the Raman signal but the excitation at this wavelength could lead to higher fluorescent background.

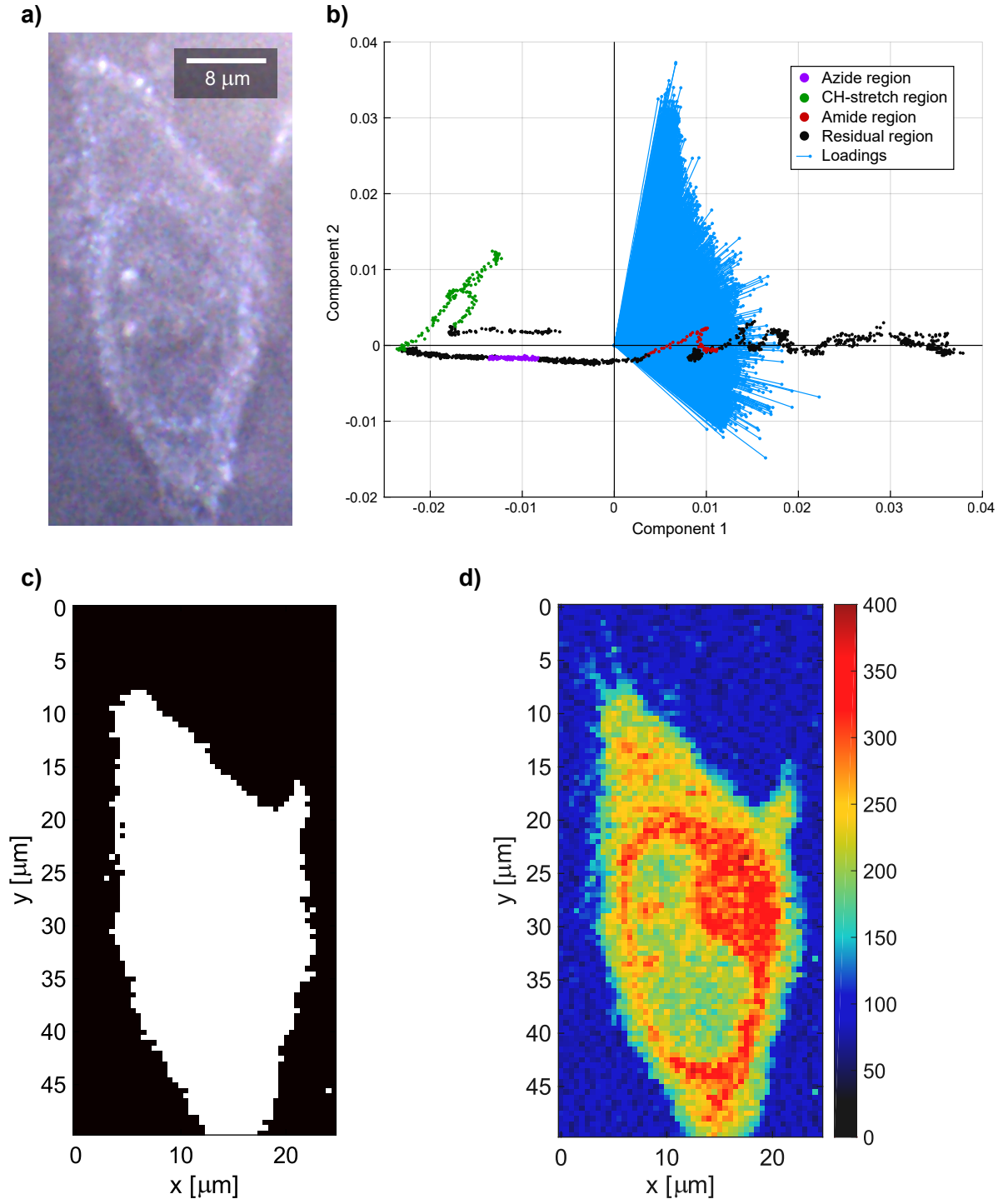

Figure 4.19. | Analysis of HeLa cell cultured with ManNAz: a) Widefield image of scanned area. b) Biplot of the obtained data set after removal of outliers. c) Selected pixels (white) fulfilling the set intensity threshold of the CH-stretch region for calculating the average spectrum of the cell. d) Raman map of the cell. The colormap represents the integrated intensity of the CH-stretch region (2800 cm^{-1}–3010 cm^{-1}).

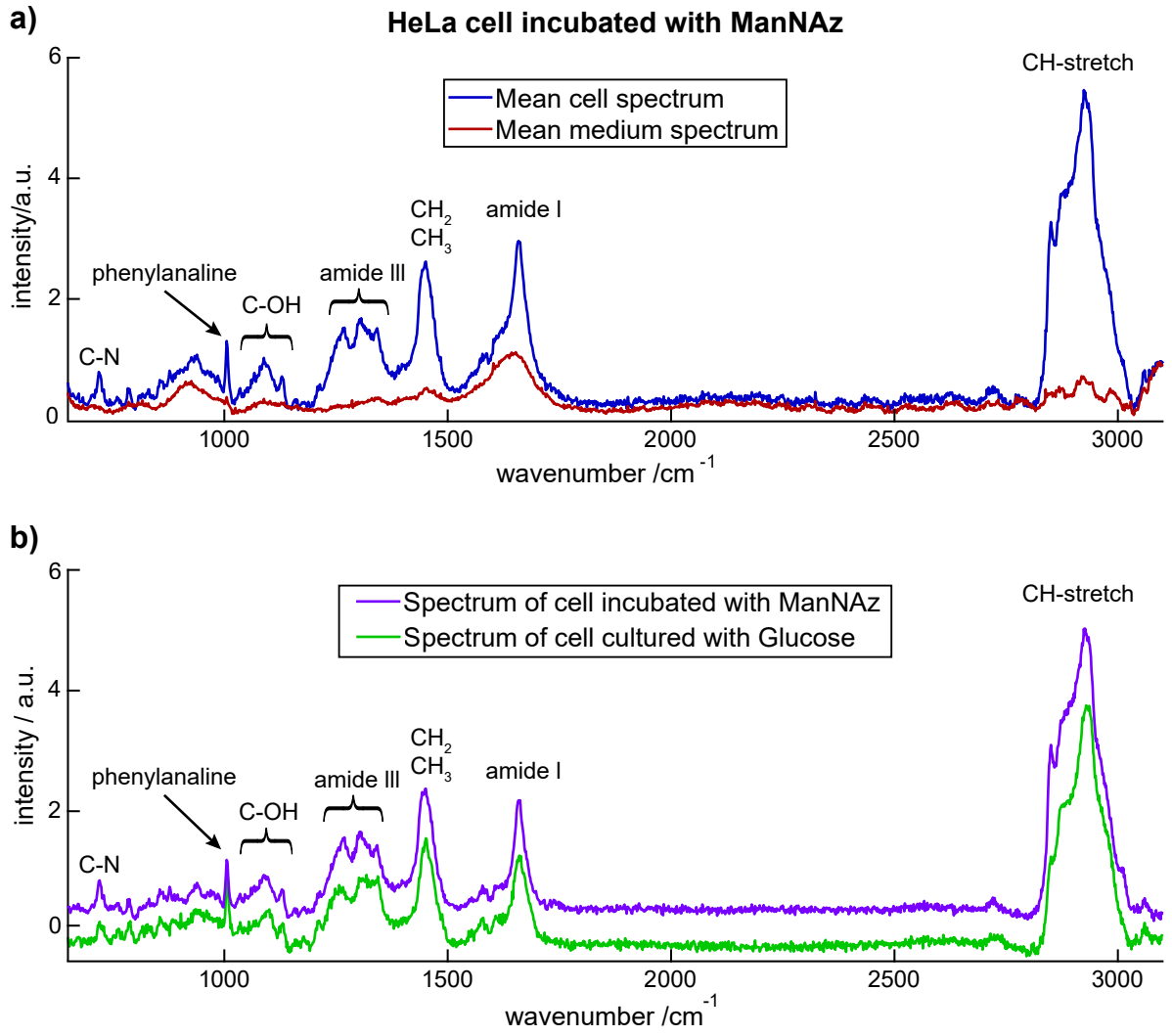

Figure 4.20. | Average spectra of HeLa cell cultured with ManNAz: a) Mean spectra of the selected pixels. b) Difference spectrum of cell and residual spectrum and comparison to the spectrum obtained from HeLa cell fed with glucose.

5. Conclusion and Outlook

Combining the advantages of fluorescence microscopy with stimulated Raman microscopy (SRS) including nonlinear optical (NLO) imaging on a single setup is certainly an interesting and promising concept. While SRS can provide a high amount of specific chemical properties of the sample at high concentrations and in a noninvasive manner, fluorescence microscopy is unmatched regarding its high detection sensitivity which can be used to obtain information at low concentrations.

In this thesis, the assembly of a microscope capable of multimodal imaging by coupling single and multiphoton excitation into one setup was presented. Two-photon absorption was confirmed via the square power law, fluorescence correlation spectroscopy and piezo scan images of HeLa cells were used to align and characterize the constructed microscope. The excitation volumes of the lasers determined by fluorescence correlation spectroscopy are in the range of experimentally achievable values. A fully functioning imaging system and stable alignment was shown via scan images of fixed WGA488 stained and unstained HeLa cells. Regarding the 1050 nm laser beam further efforts will be made for a full characterization. Although a fluorescence signal of Atto532 using 1050 nm excitation was observed, a FCS curve could not be obtained at the end of this thesis. This is likely caused by the fiber output of the 1050 nm laser exhibiting an oval shape and hence the beam profile is not a gaussian profile even after spatial filtering. Using a pinhole with smaller diameter (~ 25 µm) could solve this problem at the expense of a significantly reduced excitation power. However, since the maximum output power of the 1050 nm laser can be adjusted up to 1.5 W even a power loss of ~ 90 % after the pinhole would still be sufficient to facilitate two-photon absorption. Another important factor is the collimation of the 1050 nm beam and the possibility of chromatic aberrations, induced by the used objective, causing a considerable focal shift along the optical axis. These issues can be identified and resolved in the near future by performing bead scans in z-direction and adjusting the collimation accordingly or choosing an appropriate pinhole size. Apart from SRS, spatial and temporal overlap between both excitation sources, 1050 nm and 780 nm, will also allow two photon absorption by molecules absorbing at approximately 458 nm.

The second project involved testing the feasibility of detecting and quantifying Raman-labeled sugars featuring signals withing the Raman-silent region of the cell. Based on spontaneous Raman scattering, a library of Raman spectra of solvents and sugars in solid state and solution was acquired. The obtained dataset was further used for simulating low concentration and signal-to-noise conditions. These simulations were used to test analysis algorithms based on normal linear decomposition and principle component analysis (PCA). PCA outperformed normal linear decomposition by at least one order of magnitude and was able to accurately determine the concentration of azidoglucose at ~10^{-5} M for high SNR and ~5×10^{-5} M for low SNR values. Considering intracellular sugar concentrations in the µM and mM range, the azide stretch vibration should be detectable under physiological conditions provided that the cells metabolize these labeled sugars in similar quantities. For experimental confirmation of this concept, HeLa cells were successfully cultured with Raman-labeled sugars and examined using a confocal Raman scanning microscope. The desired azide stretch vibration could not be detected after incubating HeLa cells with N-azidoacetylmannosamine (ManNAz). Nevertheless, the similar chemical composition of these cells compared to cells solely cultured in D-glucose suggests that culturing cells with Raman-labeled sugars can be conducted in a noninvasive manner. At the current state the MATLAB script used for the analysis is tailored to the structure file exported from the WITec software. However, the variables can be easily rewritten such that the script can be applied to any hyperspectral data cube. In future experiments, a rewarding approach will certainly be the implementation of sophisticated cluster analysis methods such as *k*-means clustering and agglomerative hierarchical cluster analysis (AHCA).[98–102] Furthermore, complementary clustering via PCA can also be performed by creating Raman maps based on individual principal components. These methods hold great promises to pre-sort and differentiate similar cellular spectra of different cell compartments in an unsupervised manner. Since sugars such as ManNAz and D-glucose are metabolized differently by the cell, an average cell spectrum is not the best representation to quantify sugar uptake. While ManNaz is employed as building block in glycosylation, D-glucose serves mainly as energy source in the glycolytical pathway. Hence their localization in different areas of the cell, i.e. the cytoplasm and cell wall are expected. A combination of cluster analysis for pre-sorting of spectra and additional PCA for noise reduction will be of great benefit to identify even small amount of uptaken sugar molecules.

Within the scope of this thesis, important steps have been accomplished to investigate sugar uptake at the single cell level. On one hand, a combined multimodal imaging system has been successfully developed that provides single molecule sensitivity to visualize and investigate individual GLUT membrane transporter. The feasibility to spectroscopically detect transported sugar molecules by Raman scattering was established and new analysis methods to trace Raman-labeled sugars in living cells was developed. The spectroscopic analysis of commercially available and even synthesized sugars clearly showed that Raman-labeling of sugars, e.g. by azide moieties or isotopic markers, can be used to discriminate those against the cellular background. First cell experiments successfully proved the viability of cells to modified sugars. With the implementation of SRS on the home-built setup in the near future, the foundation was laid for studying sugar uptake activities *in vivo* in a completely new way.

List of Figures

2.1. Jablonski Diagram of various excitation and emission processes. 5
2.2. Franck-Condon-Principle. 7
2.3. Raman scattering processes. 11
2.4. Definition of Raman polarization. 14
2.5. Confocal setup schematic. 18
2.6. Fluorescence correlation spectroscopy method. 19

3.1. Microscope setup schematic. 27
3.2. Excitation and detection overview. 28
3.3. Raman setup used for liquids. 30
3.4. Hyperspectral imaging method. 32

4.1. One-photon FCS curves: Influence of detection pinhole position. 38
4.2. FCS of slowed down dyes. 39
4.3. Confocal pinhole effect on two-photon FCS. 40
4.4. TPE power dependence. 42
4.5. Two photon FCS curves. 43
4.6. Raw data of HeLa cell scans. 45
4.7. Confocal scan images of WGA488 stained HeLa cells. 47
4.8. Confocal scan images of unstained HeLa cells. 48
4.9. Raman spectra of common sugars. 50
4.10. Raman spectra of acetylated sugars. 51
4.11. Raman spectra of methylated sugars. 52
4.12. Raman spectra of glucose derivates. 53
4.13. Raman spectra of deuterated methyl α-D-glucoside. 54
4.14. Normalized Raman spectra of solvents. 55
4.15. Simulated spectra and PCA biplots. 57
4.16. Linear decomposition and PCA analysis of simulated Raman spectra. 58

4.17. Widefield image, Biplot, selected pixels and Raman map of HeLa cell cultured with 20 mM glucose. 60
4.18. Averaged spectra of HeLa cell cultured with glucose. 61
4.19. Widefield image, Biplot, selected pixels and Raman map of HeLa cell cultured with ManNAz. 63
4.20. Averaged spectra of HeLa cell cultured with ManNAz. 64

List of Tables

4.1. FCS fit values for different pinhole positions. 39
4.2. Diffusion coefficients D in dependence of glycerol content determined by FCS. 40
4.3. FCS fit values of detection pinhole effect on TPE. 41
4.4. Two-photon FCS fit values of the 2 mW–7 mW range. 44
4.5. Calculated x-y-shifts between green, red and two-photon excitation. 46
4.6. Characteristic vibrations in Raman spectra of monosaccharides.[88] 49

Abbreviations

N_3-Glc	2-Azido-2-deoxy-D-glucose
ACF	Autocorrelation function
AOD	Acousto-optic deflector
APD	Avalanche Photo Diode
CARS	Coherent anti-stokes Raman scattering
CMOS	Complementary metal-oxide semiconductor
DMEM	Dulbecco's Modified Eagle's Medium
DMSO	Dimethyl sulfoxide
EMCCD	Electron multiplying charge-coupled device
FCS	Fluorescence correlation spectroscopy
GalNAc	N-Acetyl-D-galactosamine
GDD	Group delay dispersion
GlcNAc	N-Acetyl-D-glucosamine
GLUT	solute carrier family 2, facilitated glucose uniporter
HPD	Hybrid photo detector
ManNAc	N-Acetyl-D-mannosamine
ManNAz	N-azidoacetylmannosamine
NAD(P)H	Nicotinamide adenine dinucleotide phosphate
NMR	Nuclear magnetic resonance

OPE	One-photon excitation
PAM	Pulsed interleaved excitation analysis
PBS	Phosphate-buffered saline
PCA	Principle Component Analysis
PFA	Paraformaldehyde
PMT	Photomultiplier tubes
PSF	Point spread function
SGLT	solute carrier family 5, sodium-glucose symporter
SHG	Second-harmonic generation
SRS	Stimulated Raman scattering
SVD	Singular value decomposition
TCSPC	Time-correlated single photon counting
TPE	Two-photon excitation

Bibliography

[1] E. M. Wright, B. A. Hirayama, D. F. Loo, *Journal of internal medicine* **2007**, *261*, 32–43.

[2] E. M. Wright, *American journal of physiology. Renal physiology* **2001**, *280*, F10–8.

[3] A. L. Olson, J. E. Pessin, *Annual review of nutrition* **1996**, *16*, 235–256.

[4] A. Scheepers, H.-G. Joost, A. Schürmann, *JPEN. Journal of parenteral and enteral nutrition* **2004**, *28*, 364–371.

[5] I. S. Wood, P. Trayhurn, *The British journal of nutrition* **2003**, *89*, 3–9.

[6] M. Uldry, B. Thorens, *Pflugers Archiv : European journal of physiology* **2004**, *447*, 480–489.

[7] F. Hajiaghaalipour, M. Khalilpourfarshbafi, A. Arya, *International journal of biological sciences* **2015**, *11*, 508–524.

[8] M. B. Calvo, A. Figueroa, E. G. Pulido, R. G. Campelo, L. A. Aparicio, *International Journal of Endocrinology* **2010**, *2010*.

[9] M. L. Macheda, S. Rogers, J. D. Best, *Journal of cellular physiology* **2005**, *202*, 654–662.

[10] R. A. Medina, G. I. Owen, *Biological research* **2002**, *35*, 9–26.

[11] M. Kocdor, H. Kocdor, J. Pereira, J. Vanegas, I. Russo, J. Russo, *Cancer Research* **2009**, *69*, 5152.

[12] J. Pujol-Gimenez, F. P. de Heredia, M. A. Idoate, R. Airley, M. P. Lostao, A. R. Evans, *Journal of Cancer* **2015**, *6*, 139–143.

[13] Y. R. Hussein, S. Bandyopadhyay, A. Semaan, Q. Ahmed, B. Albashiti, T. Jazaerly, Z. Nahleh, R. Ali-Fehmi, *Translational Oncology* **2011**, *4*, 321–327.

[14] J. R. Zierath, K. L. Houseknecht, B. B. Kahn, *Seminars in Cell & Developmental Biology* **1996**, *7*, 295–307.

[15] E. Karnieli, M. Armoni, *Hormone research* **1990**, *33*, 99–104.

[16] T. Asano, T. Ogihara, H. Katagiri, H. Sakoda, H. Ono, M. Fujishiro, M. Anai, H. Kurihara, Y. Uchijima, *Current medicinal chemistry* **2004**, *11*, 2717–2724.

[17] O. WARBURG, **1956**, *123*, 309–314.

[18] J. Flier, M. Mueckler, P. Usher, H. Lodish, *Science* **1987**, *235*, 1492–1495.

[19] L.-Q. Chen, L. S. Cheung, L. Feng, W. Tanner, W. B. Frommer, *Annual review of biochemistry* **2015**, *84*, 865–894.

[20] N. Yamamoto, H. Ashida, *Food Science and Technology Research* **2012**, *18*, 493–503.

[21] R. de Michele, C. Ast, D. Loqué, C.-H. Ho, S. La Andrade, V. Lanquar, G. Grossmann, S. Gehne, M. U. Kumke, W. B. Frommer, *eLife* **2013**, *2*, e00800.

[22] C.-H. Ho, W. B. Frommer, **2014**, *3*.

[23] L. Yin, W. Wang, S. Wang, F. Zhang, S. Zhang, N. Tao, *Biosensors & bioelectronics* **2015**, *66*, 412–416.

[24] M. A. Nolte, G. Kraal, R. E. Mebius, *Cytometry. Part A : the journal of the International Society for Analytical Cytology* **2004**, *61*, 35–44.

[25] K. B. Abbitt, G. Rainger, G. B. Nash, *Journal of Immunological Methods* **2000**, *239*, 109–119.

[26] Toporski J., Dieing T., Hollricher O.

[27] G. Shetty, C. Kendall, N. Shepherd, N. Stone, H. Barr, *British Journal of Cancer* **2006**, *94*, 1460–1464.

[28] P. Crow, B. Barrass, C. Kendall, M. Hart-Prieto, M. Wright, R. Persad, N. Stone, *British Journal of Cancer* **2005**, *92*, 2166–2170.

[29] W.-L. Lo, J.-Y. Lai, S. E. Feinberg, K. Izumi, S.-Y. Kao, C.-S. Chang, A. Lin, H. K. Chiang, *Journal of Raman Spectroscopy* **2011**, *42*, 174–178.

[30] K. Klein, A. M. Gigler, T. Aschenbrenner, R. Monetti, W. Bunk, F. Jamitzky, G. Morfill, R. W. Stark, J. Schlegel, *Biophysical journal* **2012**, *102*, 360–368.

[31] W. J. Tipping, M. Lee, A. Serrels, V. G. Brunton, A. N. Hulme, *Chemical Society reviews* **2016**, *45*, 2075–2089.

[32] D. Fu, Y. Yu, A. Folick, E. Currie, R. V. Farese, T.-H. Tsai, X. S. Xie, M. C. Wang, *Journal of the American Chemical Society* **2014**, *136*, 8820–8828.

[33] L. Wei, F. Hu, Y. Shen, Z. Chen, Y. Yu, C.-C. Lin, M. C. Wang, W. Min, *Nature Methods* **2014**, *11*, 410–412.

[34] E. Ploetz, S. Laimgruber, S. Berner, W. Zinth, P. Gilch, *Applied Physics B* **2007**, *87*, 389–393.

[35] C.-S. Liao, P. Wang, J. Li, H. J. Lee, G. Eakins, J.-X. Cheng, *Science Advances* **2015**, *1*, e1500738–e1500738.

[36] C.-S. Liao, P. Wang, C. Y. Huang, P. Lin, G. Eakins, R. T. Bentley, R. Liang, J.-X. Cheng, *ACS Photonics* **2018**, *5*, 947–954.

[37] S. Lim, B. Chon, H. Rhee, M. Cho, *Journal of Raman Spectroscopy* **2018**, *49*, 607–620.

[38] L. Wei, Z. Chen, L. Shi, R. Long, A. V. Anzalone, L. Zhang, F. Hu, R. Yuste, V. W. Cornish, W. Min, *Nature* **2017**, *544*, 465–470.

[39] C. Ota, T. Furukawa, K. Shima, S. Sano, K. Kuramochi, K. Tsubaki, S. Noguchi, K. Takano, *ChemistrySelect* **2017**, *2*, 1267–1270.

[40] S. Hong, T. Chen, Y. Zhu, A. Li, Y. Huang, X. Chen, **2014**, *53*, 5827–5831.

[41] J. D. Kovac, *Journal of Chemical Education* **1998**, *75*, 545.

[42] N. A. Nemkovich, A. N. Rubinov, V. I. Tomin in *Topics in fluorescence spectroscopy*, (Eds.: J. R. Lakowicz, C. D. Geddes), Topics in Fluorescence Spectroscopy, Plenum Press, New York, **1991-**, pp. 367–428.

[43] J. R. Lakowicz, *Principles of fluorescence spectroscopy*, 3rd ed., Springer, New York, **2006**.

[44] M. Göppert-Mayer, *Annalen der Physik* **1931**, *401*, 273–294.

[45] W. Kaiser, C. G. B. Garrett, *Physical Review Letters* **1961**, *7*, 229–231.

[46] B. Kierdaszuk, I. Gryczynski, J. R. Lakowicz in *Topics in fluorescence spectroscopy*, (Eds.: J. R. Lakowicz, C. D. Geddes), Plenum Press, New York, **1991-**, pp. 187–209.

[47] G. Baym, *Lectures on Quantum Mechanics*, Chapman and Hall/CRC, Boulder, **2018**.

[48] D. A. Long, *The Raman effect: A unified treatment of the theory of Raman scattering by molecules*, Wiley, Chichester and New York, **2002**.

[49] J.-X. Cheng, *Coherent Raman Scattering Microscopy*, CRC Press, **2016**.

[50] A. Smekal, *Die Naturwissenschaften* **1923**, *11*, 873–875.

[51] C. V. RAMAN, *Nature* **1928**, *121*, 619.

[52] *Archiv für Mikroskopische Anatomie* **1873**, *9*, 418–440.

[53] Airy, **1835**, *5*, 283–291.

[54] Rayleigh, *The London Edinburgh and Dublin Philosophical Magazine and Journal of Science* **1879**, *8*, 261–274.

[55] M. Minsky, *US Patent 3013467* **1961**.

[56] A. Diaspro, *Confocal and two-photon microscopy: Foundations, applications, and advances / edited by Alberto Diaspro*, Wiley-Liss, New York, **2002**.

[57] M. Eigen, R. Rigler, *Proceedings of the National Academy of Sciences of the United States of America* **1994**, *91*, 5740–5747.

[58] J. Schüler, J. Frank, U. Trier, M. Schäfer-Korting, W. Saenger, *Biochemistry* **1999**, *38*, 8402–8408.

[59] E. Margeat, N. Poujol, A. Boulahtouf, Y. Chen, J. D. Müller, E. Gratton, V. Cavailles, C. A. Royer, *Journal of molecular biology* **2001**, *306*, 433–442.

[60] D. Magde, E. Elson, W. W. Webb, *Physical Review Letters* **1972**, *29*, 705–708.

[61] E. L. Elson, D. Magde, *Biopolymers* **1974**, *13*, 1–27.

[62] D. Magde, E. L. Elson, W. W. Webb, *Biopolymers* **1974**, *13*, 29–61.

[63] R. Rigler, Mets, J. Widengren, P. Kask, *European Biophysics Journal* **1993**, *22*.

[64] A. Nagy, J. Wu, K. M. Berland, *Biophysical journal* **2005**, *89*, 2077–2090.

[65] D. C. Heinz, Chein-I-Chang, *IEEE Transactions on Geoscience and Remote Sensing* **2001**, *39*, 529–545.

[66] G. Govindu, S. Choi, V. Prasanna, V. Daga, S. Gangadharpalli, V. Sridhar in International parallel & distributed processing symposium, IEEE, **2004**, pp. 149–156.

[67] F. M. Dopico, J. M. Molera, *SIAM Journal on Matrix Analysis and Applications* **2005**, *27*, 561–581.

[68] D. Dereniowski, M. Kubale in *Parallel processing and applied mathematics*, (Ed.: R. Wyrzykowski), Lecture notes in computer science, 0302-9743, Springer, Berlin and London, **2004**, pp. 985–992.

[69] G. H. Golub, C. F. van Loan, *Matrix computations*, 3rd ed., Johns Hopkins University Press, Baltimore and London, **1996**.

[70] K. Pearson, *The London Edinburgh and Dublin Philosophical Magazine and Journal of Science* **1901**, *2*, 559–572.

[71] M. A. Elliott, G. A. Walter, A. Swift, K. Vandenborne, J. C. Schotland, J. S. Leigh, *Magnetic Resonance in Medicine* **1999**, *41*, 450–455.

[72] R. Bro, A. K. Smilde, *Anal. Methods* **2014**, *6*, 2812–2831.

[73] H. Abdi, L. J. Williams, *Wiley Interdisciplinary Reviews: Computational Statistics* **2010**, *2*, 433–459.

[74] *A practical approach to microarray data analysis*, (Eds.: D. P. Berrar, W. Dubitzky, M. Granzow), Kluwer Academic, Boston, Mass. and London, **2002**.

[75] M. E. Wall, A. Rechtsteiner, L. M. Rocha in *A practical approach to microarray data analysis*, (Eds.: D. P. Berrar, W. Dubitzky, M. Granzow), Kluwer Academic, Boston, Mass. and London, **2002**, pp. 91–109.

[76] J. Bollen, H. van de Sompel, A. Hagberg, R. Chute, *PloS one* **2009**, *4*, e6022.

[77] A. Hyvärinen, E. Oja, *Neural Networks* **2000**, *13*, 411–430.

[78] I. Osticioli, N. Mendes, A. Nevin, F. P. Gil, M. Becucci, E. Castellucci, *Spectrochimica Acta Part A: Molecular and Biomolecular Spectroscopy* **2009**, *73*, 525–531.

[79] J. Guicheteau, L. Argue, D. Emge, A. Hyre, M. Jacobson, S. Christesen, *Applied Spectroscopy* **2008**, *62*, 267–272.

[80] W. Schrimpf, A. Barth, J. Hendrix, D. C. Lamb, *Biophysical journal* **2018**, *114*, 1518–1528.

[81] Y. Sawama, Y. Yabe, H. Iwata, Y. Fujiwara, Y. Monguchi, H. Sajiki, **2012**, *18*, 16436–16442.

[82] R. Lowery, M. I. Gibson, R. L. Thompson, E. Fullam, **2015**, *51*, 4838–4841.

[83] D. B. Chase, *Journal of the American Chemical Society* **1986**, *108*, 7485–7488.

[84] D. Bannon, *Nature Photonics* **2009**, *3*, 627–629.

[85] V. Mazet, C. Carteret, D. Brie, J. Idier, B. Humbert, *Chemometrics and Intelligent Laboratory Systems* **2005**, *76*, 121–133.

[86] C. F. Gauss, Theoria motus corporum coelestium in sectionibus conicis solem ambientium, **1809**.

[87] O. Kafri, S. Kimel, *Chemical Physics* **1974**, *5*, 488–493.

[88] D. A. Long, *Journal of Raman Spectroscopy* **2004**, *35*, 905.

[89] N. K. Howell, G. Arteaga, S. Nakai, E. C. Y. Li-Chan, *Journal of Agricultural and Food Chemistry* **1999**, *47*, 924–933.

[90] P. LAGANT, G. VERGOTEN, G. FLEURY, M.-H. Loucheux-Lefebvrr, *European Journal of Biochemistry* **1984**, *139*, 137–148.

[91] *Glucose Metabolism in the Brain*, 1. Aufl., (Ed.: D. Dwyer), Elsevier textbooks, s.l., **2002**.

[92] J. H. Byrne, J. L. Roberts, *From molecules to networks: An introduction to cellular and molecular neuroscience*, 2nd ed., Academic Press/Elsevier, Amsterdam and Boston, **2009**.

[93] H.-C. Tai, N. Khidekel, S. B. Ficarro, E. C. Peters, L. C. Hsieh-Wilson, *Journal of the American Chemical Society* **2004**, *126*, 10500–10501.

[94] L. K. Mahal, *Science* **1997**, *276*, 1125–1128.

[95] E. Saxon, *Science* **2000**, *287*, 2007–2010.

[96] S.-G. Sampathkumar, A. V. Li, M. B. Jones, Z. Sun, K. J. Yarema, *Nature Chemical Biology* **2006**, *2*, 149–152.

[97] M. Mathlouthi, D. Vinh Luu, *Carbohydrate Research* **1980**, *81*, 203–212.

[98] R. Parthasarathy, G. Thiagarajan, X. Yao, Y.-P. Wang, P. Spencer, Y. Wang, *Journal of biomedical optics* **2008**, *13*, 014020.

[99] H. Salehi, I. Calas-Bennasar, J.-C. Durand, E. Middendorp, J. Valcarcel, C. Larroque, K. Nagy, K. Turzó K, I. Dekany, F. J. G. Cuisinier, *Journal of Raman Spectroscopy* **2014**, *45*, 807–813.

[100] I. W. Schie, T. Huser, *Applied spectroscopy* **2013**, *67*, 813–828.

[101] J. Hilderink, C. Otto, C. Slump, A. Lenferink, M. Engelse, C. van Blitterswijk, E. de Koning, M. Karperien, A. van Apeldoorn, *PloS one* **2013**, *8*, e78148.

[102] B. Prats Mateu, E. Harreither, M. Schosserer, V. Puxbaum, E. Gludovacz, N. Borth, N. Gierlinger, J. Grillari, *Biotechnology journal* **2017**, *12*.

A. Appendix

MATLAB script used for the analysis of live cell data obtained from confocal Raman scanning:

```
%% Analysis of hyperspectral data
%select matlab file, import as a structure and rename it
    [fileName,PathName]  =  uigetfile('','Select a Large-Area-Scan');
    cd(PathName);
    A = load(fileName);
    Names = fieldnames(A);
    fName = Names{1,1};
    Label = strcat('LAS',fName(17:19));
%get x- and y-Data: geometrical parameters of the map
%x: points per line: A.(fName).imageaxisscale{2,1}
%y: Lines per image: A.(fName).imageaxisscale{1,1}
    ImageData.ySize = double(A.(fName).imageaxisscale{1,1});
    ImageData.xSize = double(A.(fName).imageaxisscale{2,1});
    spectra = double(A.(fName).data');
%% Perform PCA
% choose a specific Rank or an explained threshold
    prompt  =  {'Rank' 'Explained'};
    dlg_title  =  'PCA';
    dims = [1 40];
    defaultans  =  {'3' '1'};
    Answer  =  inputdlg(prompt,dlg_title,dims,defaultans);
    rank = str2double(Answer{1,1});
    perc = str2double(Answer{2,1});
    [coefs,score,¬,¬,explained,mu] = pca(spectra,'algorithm','svd');
    figure
    LoadingPlot = biplot(coefs(:,1:2),'Scores',score(:,1:2));
%% prepare z-Data
    yData.Original = reshape(double(A.(fName).data'),[size(A.(fName).data,2),...
         size(ImageData.ySize,2),size(ImageData.xSize,2)]);
    prompt  =  {'Threshold'};
    dlg_title  =  'Determine Outliers';
    dims = [1 40];
    defaultans  =  {'700'};
    Answer  =  inputdlg(prompt,dlg_title,dims,defaultans);
    threshold = str2double(Answer{1,1});
    for i=1:size(spectra,2)
          for j=1:size(spectra,1)
             if spectra(j,i) > threshold
             outliers(:,i) = spectra(:,i);
            end
```

```
41          end
42      end
43  %% selected rank approximation
44      while sum(explained(1:rank,:))<perc
45           rank = rank + 1;
46      end
47      rec= score(:,1:rank) * coefs(:,1:rank)' + mu;
48  %% background correction
49  % Select order, threshold and costfunction via UI
50      x = (1:size(rec,1))';
51      [¬,¬,¬,order,threshold,¬] = backcor(x,mean(rec,2));
52  %perform background correction
53      spectra_backcor = zeros(size(rec,1),size(rec,2));
54      for k=1:size(rec,2)
55           if isempty(rec(:,k))==0
56               [EST,¬,¬] = backcor(x,rec(:,k),order,threshold,'atq');
57               spectra_backcor(:,k) = rec(:,k)-EST(:,1);
58               spectra_backcor(:,k) = ...
59                  (spectra_backcor(:,k)-min(spectra_backcor(:,k)));
60              else
61               spectra_backcor(:,k) = rec(:,k);
62              end
63      end
64  %% select range of interest
65      prompt  =  {'x1' 'x2'};
66      dlg_title  =  'Range';
67      dims = [1 35];
68      defaultans  =  {'2800','3010'};
69      Answer  =  inputdlg(prompt,dlg_title,dims,defaultans);
70      x1 = str2double(Answer{1,1});
71      x2 = str2double(Answer{2,1});
72      xData.Raw  =  double(A.(fName).axisscale{2,1});
73      xRange  =  xData.Raw > x1 & xData.Raw < x2;
74      [row,col]  =  find(xRange);
75      xData.Indices  =  col;
76  %% Sum up selected region
77      yData.intensitiesCH =  spectra_backcor(xData.Indices,:);
78      yData.sumCHvector   =  nansum(yData.intensitiesCH,1);
79  %% Additional Filter for Outliers
80      prompt  =  {'Threshold'};
81      dlg_title  =  'Determine Outliers';
82      dims = [1 40];
83      defaultans  =  {'700'};
84      Answer  =  inputdlg(prompt,dlg_title,dims,defaultans);
85      threshold = str2double(Answer{1,1});
86      temp = 1;Outl = 1;
87      for k = 1:length(yData.sumCHvector)
88          if yData.sumCHvector(:,k)>threshold
89              yData.sumCHvector(:,k)= 0;
90              Outl(temp) = k;
91              temp=temp+1;
92          end
93      end
```

```
94      clear temp
95  %create 3 dimensional array containing the summed up Intensities
96  %according the imageaxes
97      yData.sumCH = reshape(yData.sumCHvector,...
98          [size(ImageData.ySize,2),size(ImageData.xSize,2)]);
99
100 %% Check if Scan was stopped before finishing
101 %check if the mean intensity of all the lines is larger than 0.
102 %redefine image axes and reduce data set
103     for ind = 1:size(yData.sumCH,1)
104         if mean(yData.sumCH(ind,:),2)>0
105             CheckMapSz(ind) = 1;
106         else
107             CheckMapSz(ind) = 0;
108         end
109     end
110 %use the rows of the measured lines to redefine
111 %the variables ImageData.xSize and ImageData.ySize
112     [row,col] = find(CheckMapSz);
113     checkMapSz  =  isequal(size(row,2),size(ImageData.ySize,2));
114     if checkMapSz  ==  0
115         h_checkMap = msgbox('Dataset contains empty arrays.');
116         ReducedData = row;
117         ImageData.ySize = ImageData.ySize(row);
118         yData.sumCH = yData.sumCH(row,:);
119 %create a selection array also for the not yet reshaped data
120 %(yData.sumCHvector)
121     for ind = 1:size(yData.sumCHvector,2)
122         if yData.sumCHvector(1,ind)>0
123             CheckMapIntens(ind) = 1;
124         else
125             CheckMapIntens(ind) = 0;
126         end
127     end
128     [row,col] = find(CheckMapIntens);
129     yData.sumCHvector = yData.sumCHvector(:,col);
130     yData.sumCH = reshape(yData.sumCHvector,...
131         [size(ImageData.ySize,2),size(ImageData.xSize,2)]);
132     else
133     end
134     xImageSize = max(ImageData.xSize)+A.(fName).imageaxisscale{1,1}(1,2);
135     yImageSize = max(ImageData.ySize)+A.(fName).imageaxisscale{2,1}(1,2);
136 %subtract Minimum of the Intensities as Background
137     for m = 1:length(yData.sumCHvector)
138         yData.sumCHsubtractMinimum(m) = ...
139             (yData.sumCHvector(m)-min(yData.sumCHvector));
140     end
141 %Reduce the hyperspectral dataset to new size
142     yData.Orig = yData.Original(:,1:size(ImageData.ySize,2)...
143          ,1:size(ImageData.xSize,2));
144     yData.sumCH2 = reshape(yData.sumCHsubtractMinimum, ...
145         [size(ImageData.ySize,2),size(ImageData.xSize,2)]);
146 %% Data selection
```

```
147 % extract the Spectra of the pixels, where
148 % Intens > c*std(Intens)
149 % while-loop for comparing resulting selection with intensity scaled image
150 %% Criterion dialog
151     CriterionAns = 1;
152     Crit = 3;
153     while CriterionAns == 1
154     yData.CriterionBasedSelection = find(yData.sumCHsubtractMinimum> ...
155         ((Crit)*std(yData.sumCHsubtractMinimum)));
156 %create the logical Matrix showing the position of the extracted
157 %Data as 1, the rest as 0
158     for k = 1:length(yData.sumCHvector)
159         if ismember(k,yData.CriterionBasedSelection)
160             yData.SelectionLogicalVector(1,k) = 1;
161         else
162             yData.SelectionLogicalVector(1,k) = 0;
163         end
164     end
165 %Collect all spectra of the selected pixels in yData.SelectionLogical
166     yData.SelectionLogical = reshape(yData.SelectionLogicalVector,...
167         [size(ImageData.ySize,2),size(ImageData.xSize,2)]);
168     RestSpect = find(yData.SelectionLogicalVector == 0);
169 %create a figure comparing the selected areas with the intensity-map
170     figTemp  =  figure;
171             ax1  =  axes('Position',[0.1 0.1 .4 1]);
172             ax2  =  axes('Position',[.55 0.1 .4 1]);
173 %plot the selected data logical matrix yData.SelectionLogical(NaN/1)
174     imagesc(ax1,ImageData.xSize,ImageData.ySize,yData.SelectionLogical);
175     shading flat;
176 % plot the intensity-map next to it
177     imagesc(ax2,ImageData.xSize,ImageData.ySize,yData.sumCH);
178     shading flat;
179     pbaspect(ax1,[length(ImageData.xSize) ...
180         length(ImageData.ySize) length(yData.sumCH)]);
181     pbaspect(ax2,[length(ImageData.xSize) ...
182         length(ImageData.ySize) length(yData.sumCH)]);
183     view(2);
184 %Check criterion
185     CriterionAnswer = questdlg(strcat ...
186         ('The criterion to select the spectra is currently: y > ',...
187         num2str(Crit),'x std(intensity). Shall it be changed?'));
188         if strcmp(CriterionAnswer,'Yes')
189             prompt  =  {'Multiplier for the std(intensity)'};
190             dlg_title  =  (strcat...
191                 ('What shall be the new criterion (now:',...
192                 num2str(Crit),'*std(intensity))'));
193             num_lines  =  1;
194         defaultans  =  {'3'};
195         CritAns  =  inputdlg(prompt,dlg_title,num_lines,defaultans);
196     Crit = str2double(CritAns{1,1});
197     close(gcf);
198         else
199             close(gcf);
```

```
200             CriterionAns = 0;
201         end
202     end
203 %% Data evaluation based on criterion
204 %in case outliers were set to 0, reset them to nan for averaging
205     if Outl ~= 1
206          for n = 1:length(Outl)
207             spectra_backcor(:,Outl(n)) = nan;
208         end
209     end
210     Data.ExtrSpectra = spectra_backcor(:,yData.CriterionBasedSelection);
211     Data.RestSpectra = spectra_backcor(:,RestSpect);
212 %calculate the mean xData.Raw from those selected by the criterion
213     MRestSpect = nanmean(spectra_backcor(:,RestSpect),2);
214     MExtrSpec = nanmean(spectra_backcor(:,yData.CriterionBasedSelection),2);
215 %normalize to OH/CH-stretch
216     MExtrSpec = MExtrSpec*(max(MRestSpect)/max(MExtrSpec));
217 %subtract the mean background xData.Raw from the mean
218     PureSpec = MExtrSpec-MRestSpect-min(MExtrSpec-MRestSpect);
219 %Save number of spectra used for the Average xData.Raw in variable
220 %'numSpecs'
221     numSpecs = numel(yData.CriterionBasedSelection);
222 %%
223 % Intensity-map
224     fig_1 = figure;
225     h_map = imagesc(ImageData.xSize,ImageData.ySize,yData.sumCH);
226     pbaspect([length(ImageData.xSize) length(ImageData.ySize)...
227          length(yData.sumCH)]);
228     view(2);
229     title('Raman Map (based on intensity in region cm^-^1)');
230     xlabel('x [\mum]','interpreter','Tex');
231     ylabel('y [\mum]','interpreter','Tex');
232     zlabel('intensity / a.u.');
233     colormap(jet(300));shading flat;colorbar;
234     a=gca;a.FontName='Arial';a.FontSize=20;a.LineWidth=1.0;
235     fig_2  =  figure;
236     h_fig2 = imagesc(ImageData.xSize,ImageData.ySize,yData.SelectionLogical);
237     shading flat;
238     pbaspect([length(ImageData.xSize) ...
239          length(ImageData.ySize) length(yData.sumCH)]);
240     view(2);
241     title('Datapoints taken for average spectrum')
242     xlabel('x [\mum]','interpreter','Tex');
243     ylabel('y [\mum]','interpreter','Tex');
244     zlabel('intensity/a.u.')
245     colormap(hot);a=gca;a.FontName='Arial';a.FontSize=20;a.LineWidth=1.0;
246 %plot mean xData.Raw of the extracted data
247     fig_3 = figure;
248     subplot(2,1,1);
249     plot(xData.Raw,MExtrSpec,xData.Raw,MRestSpect);
250     xlabel('wavenumber /cm^{-1}')
251     ylabel('intensity/a.u.')
252     legend('mean(cell spectrum)','mean(residue)','Location','best')
```

```
    a=gca;a.FontName='Arial';a.FontSize=20;a.LineWidth=1.0;a.XLim=[640 3100];
    subplot(2,1,2);
    plot(xData.Raw,PureSpec);
    xlabel('wavenumber /cm^{-1}');ylabel('intensity / a.u.')
    legend('Difference spectrum of cell and residue','Location','best')
    a=gca;a.FontName='Arial';a.FontSize=20;a.LineWidth=1.0;a.XLim=[640 3100];
%% Loading Plot
    Check data set again if any outliers remained and
    colorize selected variance of interest
    spectraBiplot=spectra_backcor;
    spectraBiplot(isnan(spectraBiplot))= 0;
    [coefs,score,¬,¬,explained,mu]=pca(spectraBiplot,'algorithm','svd');
    prompt  =  {'x1' 'x2'};
    dlg_title  =  'Range';dims = [1 35];defaultans  =  {'2800','3010'};
    Answer  =  inputdlg(prompt,dlg_title,dims,defaultans);
    x1 = str2double(Answer{1,1});
    x2 = str2double(Answer{2,1});
    xData.Raw  =  double(A.(fName).axisscale{2,1});
    xRange  =  xData.Raw > x1 & xData.Raw < x2;
    class=xRange';
    figure
    Biplot = biplot(coefs(:,1:2),'Scores', score(:,1:2), ...
         'ObsLabels', num2str(class),'markersize', 10);
    for ii = size(Biplot,1)-size(spectra,1):size(Biplot,1)-1
        userdata = get(Biplot(ii), 'UserData');
        if ¬isempty(userdata)
            if class(userdata) == 1
                set(Biplot(ii), 'Color', 'm');
            elseif class(userdata) == 0
                set(Biplot(ii), 'Color', 'r');
            end
        else
            set(Biplot(ii), 'Color', 'b');
        end
    end
    a=gca;a.FontName='Arial';a.FontSize=16;a.LineWidth=1.0;
```

MATLAB script used for background correction:

```
    function [z,a,it,ord,s,fct] = backcor(n,y,ord,s,fct)
% BACKCOR   Background estimation by minimizing a non-quadratic cost function.
%
%   [EST,COEFS,IT] = BACKCOR(N,Y,ORDER,THRESHOLD,FUNCTION) computes and estimation EST
%   of the background (aka. baseline) in a spectroscopic signal Y with wavelength N.
%   The background is estimated by a polynomial with order ORDER using a cost-function
%   FUNCTION with parameter THRESHOLD. FUNCTION can have the four following values:
%       'sh'  - symmetric Huber function :  f(x) = { x^2  if abs(x) < THRESHOLD,
%        { 2*THRESHOLD*abs(x)-THRESHOLD^2  otherwise.
%       'ah'  - asymmetric Huber function :  f(x) = { x^2  if x < THRESHOLD,
%        { 2*THRESHOLD*x-THRESHOLD^2  otherwise.
```

```
%       'stq' - symmetric truncated quadratic :  f(x) = { x^2  if abs(x) < THRESHOLD,
%           { THRESHOLD^2  otherwise.
%       'atq' - asymmetric truncated quadratic :  f(x) = { x^2  if x < THRESHOLD,
%           { THRESHOLD^2  otherwise.
%   COEFS returns the ORDER+1 vector of the estimated polynomial coefficients
%   (computed with n sorted and bounded in [-1,1] and y bounded in [0,1]).
%   IT returns the number of iterations.

% Rescaling
    N = length(n);
    [n,i] = sort(n);
    y = y(i);
    maxy = max(y);
    dely = (maxy-min(y))/2;
    n = 2 * (n(:)-n(N)) / (n(N)-n(1)) + 1;
    y = (y(:)-maxy)/dely + 1;
% Vandermonde matrix
    p = 0:ord;
    T = repmat(n,1,ord+1) .^ repmat(p,N,1);
    Tinv = pinv(T'*T) * T';
% Initialisation (least-squares estimation)
    a = Tinv*y;
    z = T*a;
% Other variables
    alpha = 0.99 * 1/2;     % Scale parameter alpha
    it = 0;                 % Iteration number
    zp = ones(N,1);         % Previous estimation
% LEGEND
    while sum((z-zp).^2)/sum(zp.^2) > 1e-9,

        it = it + 1;        % Iteration number
        zp = z;             % Previous estimation
        res = y - z;        % Residual
% Estimate d
        if isequal(fct,'sh'),
            d = (res*(2*alpha-1)) .* (abs(res)<s) + (-alpha*2*s-res) .* (res≤-s) +...
                (alpha*2*s-res) .* (res≥s);
        elseif isequal(fct,'ah'),
            d = (res*(2*alpha-1)) .* (res<s) + (alpha*2*s-res) .* (res≥s);
        elseif isequal(fct,'stq'),
            d = (res*(2*alpha-1)) .* (abs(res)<s) - res .* (abs(res)≥s);
        elseif isequal(fct,'atq'),
            d = (res*(2*alpha-1)) .* (res<s) - res .* (res≥s);
        end;
% Estimate z
        a = Tinv * (y+d);   % Polynomial coefficients a
        z = T*a;            % Polynomial
    end;
% Rescaling
    [¬,j] = sort(i);
    z = (z(j)-1)*dely + maxy;

        a(1) = a(1)-1;
```

```
        a = a*dely;% + maxy;
end
```

MATLAB script used for simulations and analysis comparison:

```
H = waitbar(0,'computing...');
for i=1:numel(conc_factor)
    for j=1:numel(noise_factor)
        for k=1:iterations
% Generate new spectrum for each iteration and calculate SNR
            for l=1:spectra+1
                mixture(:,l) = a*conc_factor(i)+b+c+d+e+f+g+x+y+z...
                    +randn(size(a,1),1)*noise_factor(j);
            end
% Calculate SNR
            SNRinf = a(2300:4100)*conc_factor(i)+z(2300:4100);
            noise=randn(size(z(2300:4100)))*noise_factor(j);
            SNR(k) = var(SNRinf-mean(SNRinf))/var(noise-mean(noise));
% Principle Component Analysis
            [coefs,score,¬,¬,explained,mu]=pca(mixture,'algorithm','svd');
             while sum(explained(1:rank,:))<perc
                 rank = rank + 1;
             end
            rec_complete= score(:,1:rank) * coefs(:,1:rank)' + mu;
            pca_decomp=[a+randn(size(a,1),1)*noise_ref,...
                b+randn(size(a,1),1)*noise_ref,c+randn(size(a,1),1)...
                *noise_ref,d+randn(size(a,1),1)*noise_ref,...
                e+randn(size(a,1),1)*noise_ref,f+randn(size(a,1),1)...
                *noise_ref,g+randn(size(a,1),1)*noise_ref, ...
                x+randn(size(a,1),1)*noise_ref,y+randn(size(a,1),1)...
                *noise_ref,z+randn(size(a,1),1)...
                *noise_ref]\rec_complete(:,1);
            temp(:,k)= [pca_decomp(1,1)/conc_factor(i),pca_decomp(2,1),...
                pca_decomp(3,1),pca_decomp(4,1),pca_decomp(5,1),...
                pca_decomp(6,1),pca_decomp(7,1),pca_decomp(8,1),...
                pca_decomp(9,1),pca_decomp(10,1)];
            lindecomp = [a+randn(size(a,1),1)*noise_ref,...
                b+randn(size(a,1),1)*noise_ref,c+randn(size(a,1),1)...
                *noise_ref,d+randn(size(a,1),1)*noise_ref,...
                e+randn(size(a,1),1)*noise_ref,f+randn(size(a,1),1),...
                g+randn(size(a,1),1)*noise_ref, ...
                x+randn(size(a,1),1)*noise_ref,y+randn(size(a,1),1)...
                *noise_ref,z+randn(size(a,1),1)*noise_ref]\mixture(:,1);
            temp2(:,k) = [lindecomp(1,1)/conc_factor(i),lindecomp(2,1),...
                lindecomp(3,1),lindecomp(4,1),lindecomp(5,1),...
                lindecomp(6,1),lindecomp(7,1),lindecomp(8,1),...
                lindecomp(9,1),lindecomp(10,1)];
            perc=(i+(i-1)*numel(noise_factor)*iterations+(j-1)...
                *iterations+k)/(iterations*numel(noise_factor)...
            *numel(conc_factor));
```

```
46              waitbar(perc,H);
47          end
48          loopednoise_pca(j,1:5) = [round(mean(SNR),1) mean(temp(1,:),2)...
49              mean(temp(2,:),2) std(temp(1,:),0,2) std(temp(2,:),0,2)];
50          loopednoise_linDecomp(j,1:5) = [round(mean(SNR),1)...
51              mean(temp2(1,:),2) mean(temp2(2,:),2) std(temp2(1,:),0,2)...
52              std(temp2(2,:),0,2)];
53      end
54      overall_pca(i,1:2) = {conc_factor(i);loopednoise_pca};
55      overall_linDecomp(i,1:2) = {conc_factor(i);loopednoise_linDecomp};
56  end
```